PHYSICAL REVIEW D **77,** 114003 (2008)

Top jets in the peak region: Factorization analysis with next-to-leading-log resummation

Sean Fleming,[1,*] Andre H. Hoang,[2,†] Sonny Mantry,[3,‡] and Iain W. Stewart[4,§]
[1]*Department of Physics, University of Arizona, Tucson, Arizona 85721, USA*
[2]*Max-Planck-Institut für Physik (Werner-Heisenberg-Institut), Föhringer Ring 6, 80805 München, Germany*
[3]*California Institute of Technology, Pasadena, California 91125, USA*
[4]*Department of Physics, Massachusetts Institute of Technology, Boston, Massachusetts 02139, USA*
(Received 21 November 2007; published 5 June 2008)

We consider top quarks produced at large energy in e^+e^- collisions, and address the question of what top mass can be measured from reconstruction. The production process is characterized by well-separated scales: the center-of-mass energy Q, the top mass m, the top decay width Γ_t, and also $\Lambda_{\rm QCD}$; scales which can be disentangled with effective theory methods. In particular we show how the mass measurement depends on the way in which soft radiation is treated, and that this can shift the mass peak by an amount of order $Q\Lambda_{\rm QCD}/m$. We sum large logs for $Q \gg m \gg \Gamma_t > \Lambda_{\rm QCD}$ and demonstrate that the renormalization group ties together the jet and soft interactions below the scale m. Necessary conditions for the invariant mass spectrum to be protected from large logs are formulated. Results for the cross section are presented at next-to-leading order with next-to-leading-log (NLL) resummation, for invariant masses in the peak region and the tail region. Using our results we also predict the thrust distribution for massive quark jets at NLL order for large thrust. We demonstrate that soft radiation can be precisely controlled using data on massless jet production, and that in principle, a short-distance mass parameter can be measured using jets with precision better than $\Lambda_{\rm QCD}$.

DOI: 10.1103/PhysRevD.77.114003 PACS numbers: 14.65.Ha, 12.39.Hg

I. INTRODUCTION

The top quark is the heaviest known fermion of the standard model and couples strongly to the Higgs sector. The most recent CDF and D0 measurements obtained a top mass, $m_t = 170.9 \pm 1.8$ GeV [1], with $\sim$1% uncertainty. For the standard model a precise top-mass determination is important for precision electroweak observables which test the theory at the quantum level, and which constrain extensions of the theory such as supersymmetry. In Ref. [2] we derived a factorization theorem for the invariant mass distribution of high energy top jets for $e^+e^- \to t\bar{t}$, which allows in principle a determination of m_t with uncertainty better than $\Lambda_{\rm QCD}$. Such accuracy is possible because the factorization theorem separates the perturbative and nonperturbative contributions in terms of field theory Wilson coefficients and matrix elements. A virtue of our approach is that the nonperturbative matrix elements are universal and in some cases are straightforward to extract from other processes. In addition the factorization theorem provides a unique prescription for determining the Wilson coefficients and perturbative matrix elements at any order in the α_s expansion. This level of control allows us to make stable predictions for the invariant mass distribution in terms of a short-distance top-quark mass, which is not limited in precision by $\Lambda_{\rm QCD}$.

Determining the top mass with jet reconstruction methods in general faces issues such as (i) defining an observable that is sensitive to the top mass, (ii) soft-gluon interactions and color reconnection, (iii) uncertainties from higher order perturbative corrections, (iv) the large top-quark width $\Gamma_t^{\rm SM} \simeq 1.4$ GeV, and other finite lifetime effects, (v) final state radiation, (vi) initial state radiation, (vii) treatment of beam remnants, (viii) underlying events, and (ix) parton distributions. In Ref. [2] we addressed the definition of a suitable top-quark mass m and issues (i) through (v) in the framework of electron-positron collisions at high energies $Q \gg m$, where Q is the center-of-mass energy and m is the top mass.[1] The analysis is suitable for a future linear collider. Issues (vii) through (ix) are avoided by treating the e^+e^- initial state, but are important in a hadron collider environment like the Tevatron or LHC. Issue (vi) is also greatly simplified in e^+e^- annihilation, since the inclusion of initial state photon radiation mainly shifts Q and thus has very little impact on our analysis.

Our analysis of top jets uses effective theory techniques to exploit the hierarchy of scales $Q \gg m \gg \Gamma \gtrsim \Lambda_{\rm QCD}$, and separate dynamical fluctuations. This hierarchy provides a systematic power counting in m/Q and Γ/m, and gives a clear interpretation to elements in the factorization theorem. In Ref. [2] we focused on developing the formalism and describing the main conceptual points in the factorization theorem for the invariant mass distribution in the peak region. The same formalism also yields a factorization theorem for the invariant mass distribution in the tail region above the peak. Here we use models for

---

[*] fleming@physics.arizona.edu
[†] ahoang@mppmu.mpg.de
[‡] mantry@theory.caltech.edu
[§] iains@mit.edu

[1] We will use m for the top mass when it is not necessary to specify the precise scheme which defines this parameter.

the soft function that are consistent for both the peak and tail regions, and carry out detailed calculations of perturbative quantities in the factorization theorem. We verify that the matching conditions which define the Wilson coefficients at the scales Q and m are infrared safe, compute one-loop perturbative corrections to the matrix elements, and carry out the next-to-leading-log renormalization-group summation of large logs. For the peak region these are logs between the scales Q, m, Γ, and $\Lambda_{\rm QCD}$, while away from the peak they are between Q^2, m^2, and the variables $M_t^2 - m_t^2$ and $M_{\bar t}^2 - m_t^2$ described below.

As an observable sensitive to the top mass, we considered in Ref. [2] the double differential invariant mass distribution in the peak region around the top resonance:

$$\frac{d^2\sigma}{dM_t^2 dM_{\bar t}^2}, \qquad M_{t,\bar t}^2 - m^2 \sim m\Gamma \ll m^2, \tag{1}$$

where

$$M_t^2 = \Bigl(\sum_{i\in X_t} p_i^\mu\Bigr)^2, \qquad M_{\bar t}^2 = \Bigl(\sum_{i\in X_{\bar t}} p_i^\mu\Bigr)^2. \tag{2}$$

Here X_t and $X_{\bar t}$ represent a prescription to associate final state hadronic four momenta to top and antitop invariant masses, respectively. For simplicity we call $X_{t,\bar t}$ the top and antitop jets, and $M_{t,\bar t}$ the invariant mass of the top and antitop jets, respectively. The distribution in Eq. (1) has a width $\Gamma \sim \Gamma_t + Q\Lambda_{\rm QCD}/m$ which can be larger than the top-quark width Γ_t. The restriction $M_{t,\bar t}^2 - m^2 \sim m\Gamma \ll m^2$ defines the peak region, which is the region most sensitive to the top-quark mass m. Here the dynamics is characterized by energy deposits contained predominantly in two back-to-back regions of the detector with opening angles of order m/Q associated with the energetic jets or leptons coming from the top and antitop decays, plus collinear radiation. The region between the top decay jets is populated by soft particles, whose momentum is assigned to one of M_t^2 or $M_{\bar t}^2$. The tail region is defined by invariant masses starting just past the peak where the cross section begins to fall off rapidly, namely, where $m^2 \gg M_{t,\bar t}^2 - m^2$ and either $M_{t,\bar t}^2 - m^2 \gtrsim m\Gamma$ or $M_{t,\bar t}^2 - m^2 \gg m\Gamma$. Farther out, when $M_{t,\bar t}^2 - m^2 \sim m^2$, we have an ultra-tail region where the cross section is very small. We do not consider the region where $M_{t,\bar t}^2 \sim Qm$. The observable in Eq. (1) in the peak and tail regions is the main focus of our analysis. We also briefly consider the cross section in the ultra-tail region.

The result for the double differential cross section in the peak region to all orders in α_s is given by [2]

$$\begin{aligned}\frac{d\sigma}{dM_t^2 dM_{\bar t}^2} &= \sigma_0 H_Q(Q, \mu_m) H_m\Bigl(m_J, \frac{Q}{m_J}, \mu_m, \mu\Bigr) \\ &\quad\times \int d\ell^+ d\ell^- B_+\Bigl(\hat s_t - \frac{Q\ell^+}{m_J}, \Gamma_t, \mu\Bigr) \\ &\quad\times B_-\Bigl(\hat s_{\bar t} - \frac{Q\ell^-}{m_J}, \Gamma_t, \mu\Bigr) S(\ell^+, \ell^-, \mu) \\ &\quad+ \mathcal{O}\Bigl(\frac{m\alpha_s(m)}{Q}\Bigr) + \mathcal{O}\Bigl(\frac{m^2}{Q^2}\Bigr) + \mathcal{O}\Bigl(\frac{\Gamma_t}{m}\Bigr) \\ &\quad+ \mathcal{O}\Bigl(\frac{s_t, s_{\bar t}}{m^2}\Bigr),\end{aligned} \tag{3}$$

where, as indicated, power corrections are suppressed by $\alpha_s m/Q$, m^2/Q^2, Γ_t/m, or $s_{t,\bar t}/m^2$. Here m_J is the short-distance top-quark mass we wish to measure, and for convenience we have defined

$$\hat s_t = \frac{s_t}{m_J} = \frac{M_t^2 - m_J^2}{m_J}, \qquad \hat s_{\bar t} = \frac{s_{\bar t}}{m_J} = \frac{M_{\bar t}^2 - m_J^2}{m_J}, \tag{4}$$

where $\hat s_{t,\bar t} \sim \Gamma$ are of natural size in the peak region. In Eq. (3) the normalization factor σ_0 is the total Born-level cross section, the H_Q and H_m are perturbative coefficients describing hard effects at the scales Q and m_J, $B_\pm$ are perturbative jet functions that describe the evolution and decay of the top and antitop close to the mass shell, and S is a nonperturbative soft function describing the soft radiation between the jets. To sum large logs $B_\pm$ and S will be evolved to distinct renormalization scales μ, as we discuss in Sec. II C below. For the tail region Eq. (3) becomes

$$\begin{aligned}\frac{d\sigma}{dM_t^2 dM_{\bar t}^2} &= \sigma_0 H_Q H_m B_+ \otimes B_- \otimes S_{\rm part} + \mathcal{O}\Bigl(\frac{\Lambda_{\rm QCD} Q}{s_{t,\bar t}}\Bigr) \\ &\quad+ \mathcal{O}\Bigl(\frac{m\alpha_s(m)}{Q}, \frac{m^2}{Q^2}, \frac{\Gamma_t}{m}\Bigr),\end{aligned} \tag{5}$$

so the only changes are that the soft function $S = S_{\rm part}(\ell^+, \ell^-, \mu)$ becomes calculable, and we have an additional $\mathcal{O}(\Lambda_{\rm QCD} Q/s_{t,\bar t})$ nonperturbative correction from the power expansion of the soft function which we will include in our analysis. The result in Eq. (3) was derived by matching QCD onto the soft collinear effective theory (SCET) [3–7] which in turn was matched onto heavy quark effective theory (HQET) [8–13] generalized for unstable particles [14–17] as illustrated in Fig. 1. The decoupling of perturbative and nonperturbative effects into the $B_\pm$ jet functions and the S soft function was achieved through a factorization theorem in SCET and HQET, aspects of which are similar to factorization for massless event shapes [18–21]. The result in Eq. (3) is an event-shape distribution for massive particles, and can be used to determine common event shapes such as thrust or jet-mass distributions. Note that a subset of our results can also be used to match results with the event-shape cross sections for massless jets, namely, by using our SCET ultra-tail cross section and taking the limit $m \to 0$.

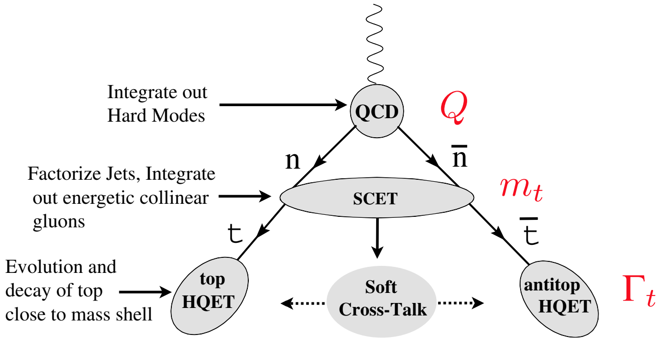

FIG. 1 (color online). Sequence of effective field theories used to compute the invariant mass distribution.

In general the functions $B_\pm$ and S depend on exactly how M_t and $M_{\bar{t}}$, or equivalently X_t and $X_{\bar{t}}$, are defined. The factorization theorem in Eq. (3) holds in the form shown when all the soft radiation is assigned to either X_t or $X_{\bar{t}}$, and the probability of radiation being assigned to X_t or $X_{\bar{t}}$ increases to unity when we approach the top or antitop direction [2]. Finally, the definition should be inclusive in the hard jets and leptons from the top decay. One possibility for defining $M^2_{t,\bar{t}}$ in Eq. (3) is a hemisphere mass definition, where X_t, $X_{\bar{t}}$ contain everything to the left or right of the plane perpendicular to the thrust axis. In this case our S is identical to the soft function of Refs. [18,19,22] that appears in the factorization theorem for massless event shapes in the dijet region. For studies of soft functions in massless event shapes see Refs. [18–29]. The $B_\pm$ are inclusive in the jets from the top decay and collinear radiation and can be defined by forward matrix elements [2]. Other definitions to associate all soft radiation to the top and antitop jets can be used which modifies the required S function, but for the class of masses defined above leaves $B_\pm$ unchanged.

The use of a short-distance mass definition in the $B_\pm$ jet function and a short-distance gap parameter in the soft function S [30] are crucial for obtaining predictions that remain stable when higher order perturbative corrections are included. In Ref. [2] we showed that suitable mass schemes for reconstruction measurements can only differ from the pole mass by an amount $\delta m \sim \Gamma_t \alpha_s$, and we proposed a jet-mass scheme which satisfies this criteria. We will refine the criteria for this jet-mass scheme here. In Eq. (3) the jet mass m_J only appears in the calculable Wilson coefficients and jet functions $B_\pm$. The greatest sensitivity to m_J is in $B_\pm$. Through these jet functions, m_J influences the spectrum of the mass distribution in the peak region. The spectral distribution and location of the peak are also affected by nonperturbative effects in the soft function S. In Ref. [30] a gap parameter scheme based on moments of the partonic soft function was devised to avoid perturbative ambiguities in the definition of the partonic end point where the variables $\ell^\pm$ in Eq. (3) approach zero. Methods for using Eq. (3) to extract m_J are discussed in detail in Ref. [2].

In this paper we determine the functions H_Q, H_m, $B_\pm$ at one-loop order in α_s, and carry out the summation of large logs between the scales $Q \gg m \gg \Gamma$ in Eq. (3). The derivation of results for the top jet-mass scheme are discussed in detail. We also show that there are constraints on the allowed soft functions, and implement a consistent method to include perturbative corrections in S. In our numerical analysis we extend the work in Ref. [2] to one-loop order, including the summation of the next-to-leading order logarithms using renormalization-group (RG) evolution in effective field theories. Our analysis of the $t\bar{t}$ jet cross section at this order includes both invariant masses in the peak region and the tail region above the peak, and the final results are analytic up to integration over the soft-function model.

For massless jets there has been a lot of work done on the program of resumming logs in event-shape variables [31,31–44]. In this paper we do not use the traditional approach to resummation, but rather an approach that sums the same large logs based on the renormalization of operators in effective field theories, including HQET and SCET [3,7]. The effective theory resummation technique has the advantage of being free of Landau-pole singularities [45,46], since it only depends on the evaluation of anomalous dimensions at perturbative scales. This technique can also be extended in a straightforward manner to arbitrary orders, N^{k}LL in the resummation [47,48]. A recent application of the SCET technique is the resummation for thrust in e^+e^- to massless jets at NLL order [49].

In our log summation there is an important distinction between large logs which affect the overall cross section normalization, and large logs that change the shape of the distribution in $M^2_{t,\bar{t}}$. In predicting the normalization in the dijet region we must sum up a series of double Sudakov logarithms that occur for $Q \gg m$ and for $m \gg \Gamma$. However, it turns out that the same is not true for logs affecting the shape of the invariant mass spectrum. As we discuss in detail, the form of the spectrum is protected from large logs below the scale Q until we reach the fundamental low energy scale governing the dynamics of either the soft or jet functions. This conclusion is not affected by the mass threshold at m, and is valid to all orders in perturbation theory (i.e. for both leading and subleading series of logarithms). In order for this cancellation to occur it is important that the invariant mass definition includes soft radiation at wide angles. The hemisphere mass definition of M_t and $M_{\bar{t}}$, as well as other definitions which associate wide angle soft radiation to both X_t and $X_{\bar{t}}$, are in this category. In the effective field theory this protection against the appearance of shape changing large logs is described by a set of “consistency conditions.” From our analysis we find that the only shape changing large logs occur between the low energy scale $\mu \sim Q\Lambda/m + \Gamma_t$ where logs in the jet functions are minimized, and a perturbative low energy scale $\mu \gtrsim \Lambda + m\Gamma_t/Q$ where logs in the soft function are minimized. Here $\Lambda \sim 0.5$ GeV is the hadronic scale where the interactions are nonperturbative. As indicated there are two scales appearing in each of these functions, and the question of which dominates depends on the size of these parameters.

The program of this paper is as follows. In Sec. II A we review the formulation of the factorization theorem for the invariant mass cross section from Ref. [2]. In Sec. II B we show that the finite lifetime effects can be treated as a convolution of $B_\pm$ jet functions for stable top quarks with a Breit-Wigner, and we describe models for S that are consistent in the presence of perturbative corrections. In Sec. II C we discuss the structure of large logarithms and present the factorization with log resummation. In Sec. III we discuss the connection between renormalization and the resummation of large logs in SCET and HQET, derive the consistency conditions, and summarize results for the NLL renormalization-group evolution. Results for the matching, running, and matrix elements in SCET including the soft hemisphere function are given in Sec. IV. In Sec. V we give matching, running, and matrix-element results in HQET. A short-distance jet-mass scheme is discussed in detail in Sec. VI, including its relation to other schemes at one loop. In Sec. VII we discuss the nonperturbative soft function model and the scheme for the gap parameter we use in our numerical analysis. An analysis of the one-loop cross section with NLL log summation is given in Sec. VIII for both the peak and tail regions. Conclusions are given in Sec. IX. Additional computational details are given in the Appendices A, B, C, D, E, and F.

II. FORMALISM

A. Invariant mass cross section

In this section we review the main definitions of effective theory objects needed for our calculations of terms in the factorization theorem in Eq. (3). Further details can be found in Ref. [2]. Starting from QCD, the two-jet cross section $\sigma(e^+e^- \to \gamma^*, Z^* \to j_t j_{\bar t})$ can be written as

$$\sigma = \sum_X^{\text{res.}} (2\pi)^4 \delta^4(q - p_X) \sum_{i,j=a,v} L_{\mu\nu}^{ij} \langle 0|\mathcal{J}_j^{\dagger\nu}(0)|X\rangle \times \langle X|\mathcal{J}_i^\mu(0)|0\rangle, \tag{6}$$

where $q = p_{e^-} + p_{e^+}$, and $q^2 = Q^2$, and $L_{\mu\nu}^{ij}$ is the leptonic tensor including vector and axial vector contributions from photon and Z boson exchange. This result is valid to all orders in the QCD coupling but lowest order in the electroweak interactions. The superscript "res." on the summation symbol denotes a restriction on the sum over final states to the kinematic situation given in Eq. (1). The QCD top-quark currents are $\mathcal{J}_i^\mu = \bar\psi(x)\Gamma_i^\mu\psi(x)$, where $\Gamma_v^\mu = \gamma^\mu$ and $\Gamma_a^\mu = \gamma^\mu\gamma_5$. In Ref. [2] we started with Eq. (6) and derived the factorization theorem for the double differential invariant mass distribution in the peak region in Eq. (3). There the factor σ_0 is the tree-level Born cross section,

$$\sigma_0 = N_c \frac{4\pi\alpha^2}{3Q^2}\bigg[e_t^2 - \frac{2Q^2 v_e v_t e_t}{Q^2 - m_Z^2} + \frac{Q^4(v_e^2 + a_e^2)(v_t^2 + a_t^2)}{(Q^2 - m_Z^2)^2}\bigg], \tag{7}$$

where $v_f = (T_3^f - 2Q_f \sin^2\theta_W)/(2\sin\theta_W\cos\theta_W)$ and $a_f = T_3^f/(2\sin\theta_W\cos\theta_W)$. Equation (3) can be easily generalized to include the angular distribution in $\cos(\theta)$ where θ is the angle between the top jet direction and the e^- momentum:

$$\frac{d^3\sigma}{dM_t^2 dM_{\bar t}^2 d\cos(\theta)} = \frac{\sigma_0(\theta)}{\sigma_0}\frac{d^2\sigma}{dM_t^2 dM_{\bar t}^2}, \tag{8}$$

where

$$\begin{aligned}\sigma_0(\theta) &= \frac{d\sigma_0}{d\cos(\theta)} \\ &= \frac{\pi N_c\alpha^2}{2Q^2}\bigg[\bigg\{e_t^2 - \frac{2Q^2 v_e v_t e_t}{Q^2 - m_Z^2} \\ &\quad + \frac{Q^4(v_e^2 + a_e^2)(v_t^2 + a_t^2)}{(Q^2 - m_Z^2)^2}\bigg\}(1 + \cos^2\theta) \\ &\quad + \bigg\{\frac{4Q^2 e_t^2 a_e a_t}{Q^2 - m_Z^2} - \frac{8Q^4 a_e v_e a_t v_t}{(Q^2 - m_Z^2)^2}\bigg\}\cos\theta\bigg].\end{aligned} \tag{9}$$

The remaining functions in Eq. (3) include H_Q, a hard function that encodes quark-gluon interactions at the production scale Q, H_m which encodes perturbative effects[2] at the scale m, $B_\pm$, the jet functions for the top jet and antitop jet, respectively, and the soft function S which encodes nonperturbative information about soft hadrons radiated between the hard jets. The convolution with the soft function causes a correlation between the two-jet functions and affects the invariant mass spectrum. Each of the functions H, H_m, B_+, B_-, and S in Eq. (3) can be defined as matrix elements of operators in an appropriate effective field theory (EFT), or as matching coefficients between two EFT's. At the scale Q the matching of QCD currents onto SCET is given by a convolution formula [3]

$$\mathcal{J}_i^\mu(0) = \int d\omega d\bar\omega C(\omega, \bar\omega, \mu) J_i^\mu(\omega, \bar\omega, \mu), \tag{10}$$

where C contains short-distance dynamics, while J_i^μ describes all scales that are longer distance than Q. After making a field redefinition [5] the SCET production cur-

---

[2] The coefficient H_m is also sensitive to the ratio m/Q through its anomalous dimension. Here m/Q is the cusp angle by which the heavy quarks are off the light cone [50]. See also Sec. V below.

rent at leading order in λ is given by

$$J_i^\mu(\omega, \bar\omega, \mu) = [\bar\chi_{n,\omega} Y_n^\dagger S_n^\dagger \Gamma_i^\mu S_{\bar n} Y_{\bar n} \chi_{\bar n,\bar\omega}](0), \tag{11}$$

where we have collinear fields and Wilson lines defined in the jet fields $\chi_{n,\omega}(0) = \delta(\omega - \bar n \cdot \mathcal{P})(W_n^\dagger \xi_n)(0)$ and $\chi_{\bar n,\bar\omega}(0) = \delta(\bar\omega - n \cdot \mathcal{P})(W_{\bar n}^\dagger \xi_{\bar n})(0)$, as well as soft Y-Wilson lines and mass-mode S-Wilson lines to be discussed below. Here the (0) indicates that the fields are at coordinate $x^\mu = 0$; recall that this x^μ dependence carries information about residual momenta at scales $\lesssim Q\lambda^2 = m^2/Q$. The dependence on larger momenta is encoded in the labels of the collinear fields [6]. For example, $\delta(\omega - \bar n \cdot P)$ forces the total minus-label momentum of $(W_n^\dagger \xi_n)$ to be ω. In terms of C defined in Eq. (10), the hard function appearing in Eq. (3) is simply

$$H_Q(Q, \mu) = |C(Q, -Q, \mu)|^2, \tag{12}$$

and after including RG evolution we have $H_Q(Q, \mu) = H_Q(Q, \mu_Q) U_{H_Q}(Q, \mu_Q, \mu)$ where U_{H_Q} is the evolution kernel discussed below in Secs. II C and III.

We obtain the SCET two-jet cross section by replacing the QCD current in Eq. (6) with the SCET current. The resulting expression can be factorized as discussed in Ref. [2]

$$\begin{aligned} \frac{d^2\sigma}{dM_t^2 dM_{\bar t}^2} &= \sigma_0 H_Q(Q, \mu) \mathcal{M}(m_J, \mu) \\ &\quad \times \int_{-\infty}^{\infty} d\ell^+ d\ell^- J_n(s_t - Q\ell^+, m_J, \Gamma_t, \mu) \\ &\quad \times J_{\bar n}(s_{\bar t} - Q\ell^-, m_J, \Gamma_t, \mu) S(\ell^+, \ell^-, \mu, m_J). \end{aligned} \tag{13}$$

This result can be used to compute the cross section in the ultra-tail region, where $s_{t,\bar t} \sim m^2$. Because of the large suppression this region is not interesting experimentally, however we will still discuss formal aspects of Eq. (13) in detail because it is an important step towards deriving the peak region factorization theorem, and is also important for making the analogy with massless event shapes. The soft function $S(\ell^+, \ell^-, \mu, m_J)$ in Eq. (13) is the same as the soft function in Eq. (3), up to perturbative effects due to top-quark vacuum polarization graphs denoted by the extra argument m_J. It can be either derived by using eikonal Ward identities [51] or properties of the coupling of soft gluons to collinear particles in SCET [18]. For the case of hemisphere invariant masses it is $S(\ell^+, \ell^-) = S_{\rm hemi}(\ell^+, \ell^-)$ where

$$\begin{aligned} S_{\rm hemi}(\ell^+, \ell^-) &\equiv \frac{1}{N_c} \sum_{X_s} \delta(\ell^+ - k_s^{+a}) \delta(\ell^- - k_s^{-b}) \\ &\quad \times \langle 0 | (\bar Y_{\bar n})^{cd} (Y_n)^{ce}(0) | X_s \rangle \\ &\quad \times \langle X_s | (Y_n^\dagger)^{ef} (\bar Y_{\bar n}^\dagger)^{df}(0) | 0 \rangle \\ &= \frac{1}{N_c} \langle 0 | (\bar Y_{\bar n})^{cd} (Y_n)^{ce}(0) \delta(\ell^+ - (\hat P_a^+)^\dagger) \\ &\quad \times \delta(\ell^- - \hat P_b^-)(Y_n^\dagger)^{ef} (\bar Y_{\bar n}^\dagger)^{df}(0) | 0 \rangle. \end{aligned} \tag{14}$$

The same function $S_{\rm hemi}$ appears in event shapes for massless two-jet production, and besides the m_J and Γ_t dependence, Eq. (13) is analogous to the factorization theorem for massless dijets [20–22]. In Eq. (14) c, d, e, f are color indices, $N_c = 3$, and the soft Wilson lines are

$$\begin{aligned} Y_n(x) &= \bar{\rm P} \exp\left(-ig \int_0^\infty ds n \cdot A_s(ns + x) \right), \\ Y_n^\dagger(x) &= {\rm P} \exp\left(ig \int_0^\infty ds n \cdot A_s(ns + x) \right), \\ \bar Y_{\bar n}^\dagger(x) &= {\rm P} \exp\left(ig \int_0^\infty ds \bar n \cdot \bar A_s(\bar n s + x) \right), \\ \bar Y_{\bar n}(x) &= \bar{\rm P} \exp\left(-ig \int_0^\infty ds \bar n \cdot \bar A_s(\bar n s + x) \right), \end{aligned} \tag{15}$$

with $\bar A_\mu = \bar T^A A_\mu^A$ for the antitriplet representation, where $\bar T^A = -(T^A)^T$. In Eq. (14) k_s^a is defined as the soft momentum components from the state X_s that are included in the experimental determination of M_t (and k_s^b for $M_{\bar t}$). We also have operators $\hat P_a^+ = n \cdot \hat P_a$ and $\hat P_b^- = \bar n \cdot \hat P_b$ that project out the soft momentum components k_s^{+a} and k_s^{-b}

$$\hat P_a |X_s\rangle = k_s^a |X_s\rangle, \qquad \hat P_b |X_s\rangle = k_s^b |X_s\rangle. \tag{16}$$

For hemisphere masses the operator $\hat P_a^+$ is defined to project out the total plus momentum of soft particles in hemisphere-a (and $\hat P_b^-$ the minus momentum in hemisphere-b). In Ref. [2] it was shown that $S(\ell^+, \ell^-)$ does not depend on the top-quark width, and when we pass below the top quark mass scale is only modified by a perturbative prefactor,

$$S(\ell^+, \ell^-, \mu, m_J) = T_0(m_J, \mu) S(\ell^+, \ell^-, \mu). \tag{17}$$

The matching coefficient $T_0(m_J, \mu)$ is induced by the coupling of A_s^μ gluons to top-vacuum polarization bubbles at zero momentum. This result applies at any order in α_s, but at NLL order $T_0 = 1$.

In Eq. (13) the mass-mode function $\mathcal{M}(m_J, \mu)$ contains virtual perturbative corrections due to gluons A_m^μ and quarks ψ_m with momenta $p^\mu \sim (m_J, m_J, m_J)$, and is given by

$$\mathcal{M}(m_J, \mu) = \frac{1}{N_c^2} |\langle 0 | \bar S_{\bar n}^{ab} S_n^{ab} | 0 \rangle|^2. \tag{18}$$

The definition of these mass-mode S-Wilson lines is identical to those in Eq. (15), except that they involve gluon fields A_m^μ which couple to massive top quarks for any momentum, and which have zero-bin subtractions to avoid double counting the momentum region accounted for by the A_s^μ gluons. This implies that $\mathcal{M}(m_J, \mu)$ only gets contributions from graphs with a top-vacuum polarization bubble [52–54] coupling to the A_m^μ gluons. At NLL order the function $\mathcal{M}(m_J, \mu) = 1$, but is relevant at NNLL order and beyond when considering virtual top loops. Note that due to the invariant mass constraint $s \ll mQ$, the ψ_m quarks never appear in the final state. This is important for the validity of Eq. (13).

Matrix elements of top-quark collinear fields in SCET give the jet functions J_n for the top-quark jet, and $J_{\bar n}$ for the antitop jet,

$$\begin{aligned} J_n(Qr_n^+ - m_J^2, m_J, \Gamma_t, \mu) &= \frac{-1}{4\pi N_c Q}\,\mathrm{Im}\Big[i \int d^4x\, e^{i r_n \cdot x} \langle 0 | \mathrm{T}\{\bar\chi_{n,Q}(0) \bar{n}\!\!\!/ \chi_n(x)\} | 0 \rangle \Big], \\ J_{\bar n}(Qr_{\bar n}^- - m_J^2, m_J, \Gamma_t, \mu) &= \frac{1}{4\pi N_c Q}\,\mathrm{Im}\Big[i \int d^4x\, e^{i r_{\bar n} \cdot x} \langle 0 | \mathrm{T}\{\bar\chi_{\bar n,-Q}(x) n\!\!\!/ \chi_{\bar n}(0)\} | 0 \rangle \Big]. \end{aligned} \tag{19}$$

These jet functions J_n and $J_{\bar n}$ depend on both the mass and width of the top quarks. The matrix elements of collinear fields are defined with the zero-bin subtractions [55], which avoids double counting the soft region.

For predictions in the peak region, the J_n and $J_{\bar n}$ functions should be factorized further by integrating out the top-quark mass. This is accomplished by matching onto jet functions $B_\pm$ in HQET with boosted heavy quarks. The relevant Feynman rules are given in Appendix B. The jet-function matching takes the simple form [2]

$$\begin{aligned} J_n(s_t, m_J, \Gamma_t, \mu_Q) &= T_+(m_J, \mu_Q) B_+(\hat s_t, \Gamma_t, \mu_Q) + \mathcal{O}\Big(\frac{\Gamma}{m}\Big) + \mathcal{O}\Big(\frac{\hat s_t}{m}\Big), \\ J_{\bar n}(s_{\bar t}, m_J, \Gamma_t, \mu_Q) &= T_-(m_J, \mu_Q) B_-(\hat s_{\bar t}, \Gamma_t, \mu_Q) + \mathcal{O}\Big(\frac{\Gamma_t}{m}\Big) + \mathcal{O}\Big(\frac{\hat s_{\bar t}}{m}\Big). \end{aligned} \tag{20}$$

The HQET jet functions B_+ and B_- also depend on the residual mass term δm_J that fixes the mass definition in HQET. They are defined by

$$B_\pm(\hat s, \Gamma_t, \mu) = \mathrm{Im}[\mathcal{B}_\pm(\hat s, \Gamma_t, \mu)], \tag{21}$$

where the $\mathcal{B}_\pm$ are vacuum matrix elements of T-products of HQET operators

$$\begin{aligned} \mathcal{B}_+(2v_+ \cdot r, \Gamma_t, \mu) &= \frac{-i}{4\pi N_c m} \int d^4x\, e^{i r \cdot x} \langle 0 | T\{\bar h_{v_+}(0) W_n(0) W_n^\dagger(x) h_{v_+}(x)\} | 0 \rangle, \\ \mathcal{B}_-(2v_- \cdot r, \Gamma_t, \mu) &= \frac{i}{4\pi N_c m} \int d^4x\, e^{i r \cdot x} \langle 0 | T\{\bar h_{v_-}(x) W_{\bar n}(x) W_{\bar n}^\dagger(0) h_{v_-}(0)\} | 0 \rangle. \end{aligned} \tag{22}$$

Here for $B_+(\hat s_t, \Gamma_t, \mu)$ we have $\hat s_t = 2v_+ \cdot r$, while for $B_-(\hat s_{\bar t}, \Gamma_t, \mu)$ we have $\hat s_{\bar t} = 2v_- \cdot r$. The gluons in W_n and $W_{\bar n}^\dagger$ and HQET fields $h_{v_\pm}$ are only sensitive to fluctuations below m and are built of gluons $A_\pm^\mu$ describing low energy fluctuations down to $p^2 \sim \Gamma^2$ in the top and antitop rest frames, respectively. In Ref. [2] these gluons were called ultracollinear. We emphasize that to make the matching consistent, the collinear gluons in Eq. (22) have zero-bin subtractions for the same region as those in the SCET jet functions. These subtractions ensure that the $B_\pm$ jet functions do not double-count the soft region encoded in S, and are critical for ensuring that the functions $B_\pm$ are IR finite, as we discuss further in Appendix A. In Eq. (22) the Wilson lines are

$$\begin{aligned} W_n^\dagger(x) &= \mathrm{P}\exp\Big(ig \int_0^\infty ds\, \bar n \cdot A_+(\bar n s + x) \Big), \\ W_n(x) &= \bar{\mathrm{P}}\exp\Big(-ig \int_0^\infty ds\, \bar n \cdot A_+(\bar n s + x) \Big), \end{aligned} \tag{23}$$

with analogous formulas for $W_{\bar n}$ and $W_{\bar n}^\dagger$ in terms of $n \cdot A_-$. Note that if the Wilson lines W_n and $W_{\bar n}$ were absent, then $\mathcal{B}_\pm$ would just define the HQET heavy quark/antiquark propagators [8]. The Wilson lines, let us say for $\mathcal{B}_+$, encode the color dynamics of gluons that are soft in the top rest frame and come from the highly boosted antitop quark, and they render this vacuum matrix element into a gauge-invariant physical object. The analogous situation with top and antitop switched applies for the vacuum matrix element $\mathcal{B}_-$. For the SCET jet functions, the Wilson lines appearing in Eqs. (11) and (19) have the analogous physical interpretation where the top-quark mass has not yet been integrated out.

In the final factorization theorem in Eq. (3) we have the $B_\pm$ functions, as well as the matching condition for the mass fluctuations,

$$H_m(m,\mu) = T_+(m,\mu)T_-(m,\mu)T_0(m,\mu)\mathcal{M}(m,\mu). \tag{24}$$

In bHQET all dynamic effects associated with the top-quark mass appear in H_m, and there are no mass-mode quarks or gluons in this theory. Since T_0 and $\mathcal{M}(m,\mu)$ encode finite matching corrections at the scale $\mu \simeq m$ due to top-vacuum polarization, we have $T_0(m,\mu)\mathcal{M}(m,\mu) = 1 + \mathcal{O}(\alpha_s^2)$, and so these factors drop out from our NLL analysis. Therefore in later sections we simply use $H_m = T_+T_-$. This coefficient H_m becomes sensitive to the ratio Q/m through its anomalous dimensions which depends on a logarithm of $v_+\cdot\bar{n} = v_-\cdot n = Q/m$. Including the RG summation of these logarithms gives the coefficient $H_m(m, Q/m, \mu_m, \mu) = H_m(m,\mu_m)U_{H_m}(Q/m,\mu_m,\mu)$ appearing in the factorization theorem, where U_{H_m} is the bHQET current evolution factor discussed below in Secs. II C and III. Note that in principle $H_m(m,\mu)$ and the factors in Eq. (24) can also have Q/m dependence at NNLL. For related discussions see Refs. [56,57].

Alternatively, the matching coefficient of SCET and HQET jet functions given by H_m in Eq. (24) can be determined from currents,

$$H_m(m,\mu) = |C_m(m,\mu)|^2, \tag{25}$$

where the boosted HQET current is

$$J_i^\mu(\mu) = C_m(m,\mu)J^\mu_{\mathrm{bHQET}}(\mu), \tag{26}$$

with

$$J^\mu_{\mathrm{bHQET}} = (\bar{h}_{v_+}W_n)Y_n^\dagger\Gamma_i^\mu Y_{\bar{n}}(W_{\bar{n}}^\dagger h_{v_-}). \tag{27}$$

The soft Wilson lines Y in this current are the same as those used in the SCET soft function. The only distinction is that soft gluons in bHQET no longer couple to massive top bubbles.

Because of the large width of the top quarks the $B_\pm$ jet functions can be computed in perturbation theory. At tree level they are Breit-Wigner distributions

$$\begin{aligned} B_\pm^{\mathrm{tree}}(\hat{s},\Gamma_t) &= \mathrm{Im}[\mathcal{B}_\pm^{\mathrm{tree}}(\hat{s},\Gamma_t)] = \mathrm{Im}\left[\frac{-1}{\pi m}\frac{1}{\hat{s}+i\Gamma_t}\right] \\ &= \frac{1}{\pi m}\frac{\Gamma_t}{\hat{s}^2+\Gamma_t^2}, \end{aligned} \tag{28}$$

where we have adopted a normalization such that

$$\int_{-\infty}^{+\infty} ds B_\pm^{\mathrm{tree}}(\hat{s},\Gamma_t) = 1. \tag{29}$$

The Wilson coefficients in the factorization theorem in Eq. (3) are also normalized to unity at tree level, $H_Q = 1$ and $H_m = 1$.

B. Factorization of lifetime effects and soft-function models

The leading order bHQET Lagrangian is

$$\mathcal{L}_\pm = \bar{h}_{v_\pm}\left(iv_\pm\cdot D_\pm - \delta m + \frac{i}{2}\Gamma_t\right)h_{v_\pm}. \tag{30}$$

In light-cone coordinates, $(+,-,\perp)$, we have $v_+^\mu = (m/Q, Q/m, 0)$ and $v_-^\mu = (Q/m, m/Q, 0)$ and gluons/residual momenta scaling as $D_+^\mu \sim \Gamma(m/Q, Q/m, 1)$ and $D_-^\mu \sim \Gamma(Q/m, m/Q, 1)$. Unlike standard HQET, the ultracollinear gluon fields in bHQET are defined with zero-bin subtractions [55] for the soft region. In Eq. (30) Γ_t is a Wilson coefficient obtained by matching to the full theory and is equal to the top-quark total width. This is true to leading order in electroweak interactions, to $\mathcal{O}(m^2/Q^2)$ and $\mathcal{O}(\Gamma/m)$ in the power counting, and to all orders in α_s.[3] Finally,

$$\delta m = m_{\mathrm{pole}} - m \tag{31}$$

is the residual mass term that fixes the top-quark mass definition m that is used in the HQET computations. It needs to be consistent with the bHQET power counting [2],

$$\delta m \sim \hat{s}_t \sim \hat{s}_{\bar{t}} \sim \Gamma, \tag{32}$$

can be computed perturbatively, and is UV and IR finite. Note that the way in which Eq. (30) will be used is to compute a jet function where the width smears over a set of states of invariant mass $m\Gamma_t \gg \Lambda^2_{\mathrm{QCD}}$. Thus, for our analysis there are no $\Lambda_{\mathrm{QCD}}/\Gamma_t$ corrections to Eq. (30), just corrections of $\mathcal{O}(\Lambda_{\mathrm{QCD}}/m)$.

In Eq. (21) the jet functions $B_\pm$ are expressed in terms of the imaginary part of vacuum matrix elements $\mathcal{B}_\pm$ in Eq. (22). From $\mathcal{L}_\pm$ it is straightforward to see that $B_\pm$ can be obtained from the imaginary part of the vacuum matrix element $\mathcal{B}_\pm^{\Gamma=0}$ for (fictitious) stable top quarks by shifting the energy variable $\hat{s} \to \hat{s} + i\Gamma_t$,

---

[3] Concerning the m/Q expansion this is true because for $Q \gg m$ the hemisphere mass definition is inclusive in the top and antitop decay products up to $\mathcal{O}(m^2/Q^2)$ corrections [2]. Concerning the Γ/m expansion this is related to the fact that finite lifetime corrections are related to off-shell corrections that are $\hat{s}/m$-suppressed [58]. Concerning the α_s expansion this can be seen by carrying out the matching with free quark states and noting that the full theory computation of $t \to bW$ gives the total rate. Now only the operator of interest $(i\Gamma_t/2)\bar{h}_v h_v$ allows for decays in the effective theory, but it corresponds to a conserved current and so does not get renormalized [8].

$$\begin{aligned} B_\pm(\hat{s},\Gamma_t,\mu) &= \mathrm{Im}[\mathcal{B}_\pm(\hat{s},\Gamma_t,\mu)] \\ &= \mathrm{Im}[\mathcal{B}_\pm^{\Gamma=0}(\hat{s}+i\Gamma_t,\mu)]. \end{aligned} \tag{33}$$

Here we defined results for stable top quarks, namely, the jet function $B_\pm^{\Gamma=0}(\hat{s},\mu)\equiv B_\pm(\hat{s},0,\mu)$, and a vacuum matrix element $\mathcal{B}_\pm^{\Gamma=0}(\hat{s},\mu)\equiv\mathcal{B}_\pm(\hat{s},0,\mu)$. They are related by

$$B_\pm^{\Gamma=0}(\hat{s},\mu)=\mathrm{Im}[\mathcal{B}_\pm^{\Gamma=0}(\hat{s},\mu)], \tag{34}$$

and we will refer to $B_\pm^{\Gamma=0}$ as the stable jet function in what follows. The result in Eq. (33) is in complete analogy to the relation between the production rate of top-quark pairs in the nonrelativistic threshold region, $E_{\mathrm{c.m.}}\approx 2m$, where the leading order finite lifetime effects can be implemented by the shift $E_{\mathrm{c.m.}}\to E_{\mathrm{c.m.}}+i\Gamma_t$ prior to taking the imaginary part of the $e^+e^-\to e^+e^-$ forward scattering matrix element [16].

To separate the different physical effects in the cross section it is convenient to derive a factorization theorem for the leading order finite lifetime effects to all orders in α_s. To do so we define the function

$$g(x)\equiv-\frac{i}{2}\mathcal{B}_\pm^{\Gamma=0}(x,\mu)=-\frac{i}{2}\mathcal{B}_\pm(x,0,\mu). \tag{35}$$

It is analytic everywhere in the complex x-plane, except along the positive real axis, $x\geq 0$, where the vacuum matrix elements $\mathcal{B}_\pm^{\Gamma=0}$, defined using Eq. (22) with $\Gamma_t=0$, has a cut for intermediate states having invariant masses larger than the top-quark mass. Using the residue theorem for a contour that envelops the cut, it is then straightforward to derive the dispersion relation

$$g(a)=\frac{1}{2\pi i}\int_0^\infty dx\frac{\mathrm{Disc}[g(x)]}{x-a}, \tag{36}$$

where a is any point in the complex plane not on the positive real axis. With the choice $a=\hat{s}+i\Gamma_t$ and a change of variable $x=\hat{s}-\hat{s}'$, this dispersion relation can be brought into the form

$$B_\pm(\hat{s},\Gamma_t,\mu)=\int_{-\infty}^{\hat{s}}d\hat{s}'B_\pm^{\Gamma=0}(\hat{s}-\hat{s}',\mu)\frac{\Gamma_t}{\pi(\hat{s}'^2+\Gamma_t^2)}. \tag{37}$$

Note that the upper limit $\hat{s}$ of the integration can be replaced by $+\infty$ since the stable jet function only has support for positive values of its energy variable. Equation (37) states that the bHQET jet functions for the physical unstable top quark can be written as a convolution of the stable jet functions with a Breit-Wigner function of the width Γ_t. Thus the leading order finite lifetime effects can be factorized from the jet function.[4] This means, in particular, that the renormalization properties of the jet functions for stable and unstable top quarks are equivalent—a fact that might not be obvious since the evolution of the jet functions involves convolutions with distributions.

Equation (37) reflects the fact that the top-quark width acts as an infrared cutoff for the jet function through smearing over a Breit-Wigner function [60]. In the factorization theorem in Eq. (3) additional smearing is provided by the convolution with the soft function, where the width of the distribution $S(\ell^+,\ell^-)$ is of order the hadronic scale Λ. Equation (37) allows us to group both types of smearing into a common infrared function R, with the following modified version of the factorization theorem:

$$\frac{d^2\sigma}{dM_t^2dM_{\bar{t}}^2}=\sigma_0H_Q(Q,\mu_m)H_m\Big(m_J,\frac{Q}{m_J},\mu_m,\mu\Big)\int_{-\infty}^{\infty}d\ell^+d\ell^-B_+^{\Gamma=0}\Big(\hat{s}_t-\frac{Q\ell^+}{m_J},\mu\Big)B_-^{\Gamma=0}\Big(\hat{s}_{\bar{t}}-\frac{Q\ell^-}{m_J},\mu\Big)R(\ell^+,\ell^-,\Gamma_t,\mu). \tag{38}$$

The result involves only the stable jet functions and an infrared function defined as

$$R(\ell^+,\ell^-,\Gamma_t,\mu)\equiv\Big(\frac{m\Gamma_t}{Q\pi}\Big)^2\int_0^\infty d\tilde{\ell}^+\int_0^\infty d\tilde{\ell}^-\frac{S(\tilde{\ell}^+,\tilde{\ell}^-,\mu)}{[(\ell^+-\tilde{\ell}^+)^2+(\frac{m\Gamma_t}{Q})^2][(\ell^--\tilde{\ell}^-)^2+(\frac{m\Gamma_t}{Q})^2]}. \tag{39}$$

In the $\Gamma_t\to 0$ limit we have $R(\ell^+,\ell^-,\Gamma_t=0,\mu)=S(\ell^+,\ell^-,\mu)$, since the Breit-Wigner factors reduce to delta-functions. If $\hat{s}_{t,\bar{t}}\gg\Gamma_t$, as in the tail region, then R can be simplified with an operator product expansion whose first term depends on the partonic soft function S_{part} which can be computed in perturbation theory. In this region $\tilde{\ell}^\pm\sim s_{t,\bar{t}}/Q\gg\Lambda$, and for these momenta $S(\tilde{\ell}^\pm,\mu)=S_{\mathrm{part}}(\tilde{\ell}^\pm,\mu)$ up to power corrections of $\mathcal{O}(\Lambda Q/s_{t,\bar{t}})$. For the case $\Gamma_t\gg\frac{Q}{m}\Lambda$, R can be computed using an operator product expansion even in the peak region, taking Eq. (39) with $\frac{Q\Lambda}{m\Gamma_t}\ll 1$, and again the leading term is determined by S_{part}. This is similar to $B\to X_s\gamma$ in the multiscale operator product expansion (OPE) [47,61]

---

[4] Note that subleading finite lifetime effects, which are suppressed by Γ_t/m, cannot be factorized as in Eq. (37) since they are not described by a simple shift of the energy into the complex plane [15,17,59].

where smearing over the soft function makes it computable in an OPE. On the other hand, for top quarks $\Gamma_t \lesssim \frac{Q}{m}\Lambda$, and the infrared function is significantly affected by nonperturbative effects in S. Thus the cross section in the peak region cannot be determined entirely from perturbation theory.

These properties serve as an important guideline for the construction of a consistent model for the soft function to be used beyond the tree-level approximation. They require that the perturbative corrections contained in the partonic soft function *must be included* in a viable model in order to obtain the correct leading order term in the operator product expansion for the cases $\tilde{\ell}^{\pm} \gg \Lambda$ and $\Gamma \gg \frac{Q}{m}\Lambda$ mentioned above. As discussed in Ref. [30] one way to give a consistent implementation of the partonic soft function in S is to use a convolution form

$$S(\ell^+, \ell^-, \mu) = \int_{-\infty}^{+\infty} d\tilde{\ell}^+ \int_{-\infty}^{+\infty} d\tilde{\ell}^- \times S_{\text{part}}(\ell^+ - \tilde{\ell}^+, \ell^- - \tilde{\ell}^-, \mu, \delta) \times S_{\text{mod}}(\tilde{\ell}^+, \tilde{\ell}^-), \tag{40}$$

where S^{part} is the soft function computed in perturbation theory at μ, and S^{mod} is a hadronic function satisfying

$$\begin{aligned} &\int_{-\infty}^{+\infty} d\ell^+ \int_{-\infty}^{+\infty} d\ell^- S^{\text{mod}}(\ell^+, \ell^-) = 1, \\ &\int_{-\infty}^{+\infty} d\ell^+ \int_{-\infty}^{+\infty} d\ell^- (\ell^+)^n (\ell^-)^m S^{\text{mod}}(\ell^+, \ell^-) \\ &\quad \sim (\Lambda_{\text{QCD}})^{n+m}, \end{aligned} \tag{41}$$

for $n + m \geq 1$. An analogous formula to Eq. (40) was used to incorporate moment constraints in the study of the soft function in $b \to s\ell^+\ell^-$ in Ref. [62]. This form ensures that S reduces to S_{part} for $\ell^{\pm} \gg \Lambda$, and that for all kinematic regions it has the proper μ dependence for the $\overline{\text{MS}}$-scheme. It also gives the proper result for R in taking the limit $\Gamma \gg \frac{Q\Lambda}{m}$ of Eq. (39). The model in Eq. (40) is specified by parameters in S_{mod} which involve the hadronic scale Λ, and also by the choice of the scale μ in S_{part}. The convolution generates logarithms of the form $\ln(\ell^{\pm}/\mu)$ and $\ln(\Lambda/\mu)$ to be discussed in the next section. There are also complications related to removing a $u = 1/2$ renormalon (as indicated by the subtraction constant δ in S_{part}) and introducing a renormalon free gap parameter $\bar{\Delta}$ in the soft function [30]. We will use the prescription in Eq. (40) for our numerical studies of the factorization theorem in Sec. VIII. Our choice of S^{mod} and a review of how the renormalon subtractions work are given in Sec. VII.

C. Summation of large logs in SCET and HQET

In this section we discuss the summation of large logs between $Q \gg m \gg \Gamma$ for the peak region, and between $Q \gg m \gg \hat{s}$ in the tail region. We also discuss the ultratail region where $Q \gg \hat{s} \sim m \gg m^2/Q$. In both SCET and bHQET we can define unitary evolution functions U_i, associated with the renormalization-group evolution for hard, jet, and soft functions in Eqs. (3) and (13). These U_i factors are indicated by the arrows in Figs. 2 and 3. The figures show that there are two ways of doing the renormalization-group evolution. In the first one, referred to as "top-down," we run the SCET and bHQET production currents, starting with matching at a high scale, and running toward the low scales. In the second one, referred to as "bottom-up," we run the individual jet and soft functions, starting with initial conditions at the low scales and running up.

The UV renormalization of the currents in SCET and bHQET generates U_{H_Q} and U_{H_m}, respectively. Since the renormalization of a current does not depend on the choice of states, these factors do not carry information about the

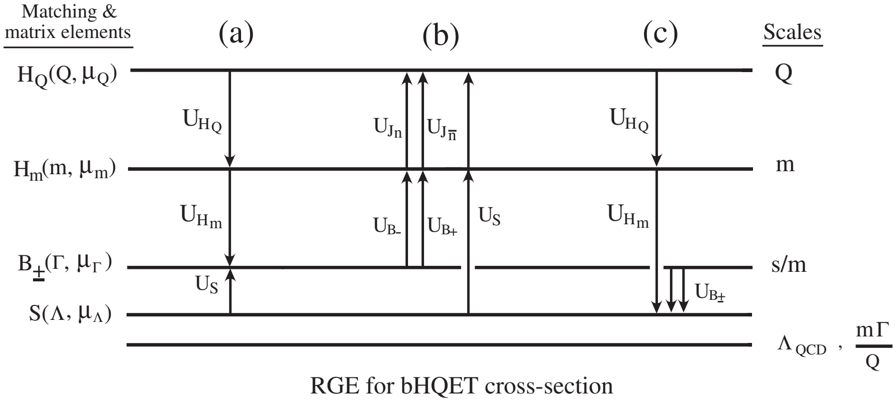

FIG. 2. Matching, running, and matrix elements that determine the functions in the factorization theorem in Eq. (3) for the peak region (when $s/m \sim \Gamma$) and for the tail region (when $s/m \gtrsim \Gamma$). The running in U_{H_Q} and U_{H_m} is local, while that in U_{J_n}, $U_{J_{\bar{n}}}$, U_S, and U_B involves convolutions. Here the distribution width is $\Gamma \sim \Gamma_t + Q\Lambda/m$. Cases (a), (b), and (c) show three equivalent ways to sum large logs with the renormalization group. The consistency equations discussed in the text express the equivalence of running from the top-down in case (a) and from the bottom-up in case (b). Case (c) is used for our numerical analysis.

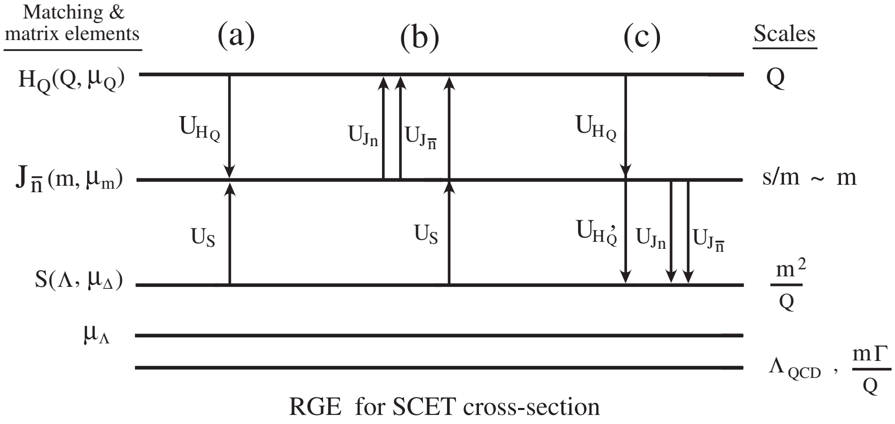

FIG. 3. Matching, running, and matrix elements that determine the functions in the factorization theorem for the ultra-tail region, in Eq. (13). The running in U_{H_Q} is local, while that in U_{J_n}, $U_{J_{\bar{n}}}$, and U_S involves convolutions. Cases (a), (b), and (c) show three equivalent ways to sum large logs with the renormalization group. The consistency equation discussed in the text expresses the equivalence of running from the top-down in case (a) and from the bottom-up in case (b).

constraints used to define M_t and $M_{\bar{t}}$. Instead U_{H_Q} and U_{H_m} only affect the overall normalization of the invariant mass distribution. On the other hand the jet and soft functions have evolution through U_J, U_B, and U_S which involve convolutions that change their respective shape. In general the jet and soft functions also incorporate the prescriptions to define M_t and $M_{\bar{t}}$.[5] Hence, although it is expected on general grounds, it is not immediately obvious how the running of these functions becomes independent of the prescription used to define these invariant masses. The equivalence of the top-down and bottom-up approaches ensures that the changes in shape of the jet and soft function cancel out in the convolution for any region in μ where they overlap in Fig. 2, and yield the same result as obtained from U_{H_Q} and U_{H_m}. In the field theory this result is encoded in a SCET consistency condition between U_{H_Q}, U_J, and U_s, and a bHQET consistency condition between U_{H_m}, U_B, and U_s, where as we will show to all orders in perturbation theory the soft-function evolution factorizes as

$$U_S(\ell^+, \ell^-) = U_s(\ell^+) U_s(\ell^-). \tag{42}$$

The consistency conditions between the scales μ and μ_0 are

$$\begin{aligned} \sqrt{U_{H_Q}(Q, \mu, \mu_0)}\, U_J(s, \mu_0, \mu) &= \frac{1}{Q} U_s\Big(\frac{s}{Q}, \mu, \mu_0\Big), \\ \sqrt{U_{H_m}\Big(\frac{Q}{m}, \mu, \mu_0\Big)}\, U_B(\hat{s}, \mu_0, \mu) &= \frac{m}{Q} U_s\Big(\frac{m\hat{s}}{Q}, \mu, \mu_0\Big). \end{aligned} \tag{43}$$

The derivation of Eqs. (42) and (43) will be given in Sec. III C below, while field theory definitions of the U_i are given in Secs. III A and III B. Note that this discussion implies that the SCET factorization theorem in Eq. (13) can be formulated at any scale $\mu > m$, and the final factorization theorem in Eq. (3) can be formulated at any scale $\mu < m$ without affecting the renormalization-group evolution. For $\mu > m$ we have $n_f = 6$ flavors, while for $\mu < m$ we have $n_f = 5$ flavors for these evolution factors.

In the peak region factorization theorem in Eq. (3) the $B_\pm$ and S functions are evaluated at a common scale μ. Since they involve logarithms of the form $\ln[(-\hat{s} - i\Gamma_t)/\mu]$ and $\ln(\Lambda/\mu)$, where Γ_t and the hadronic scale Λ differ, it is natural to consider using different low energy scales μ_Γ and μ_Λ for the jet and soft functions, respectively. In this case we have a region between μ_Γ and μ_Λ where the consistency conditions no longer apply. Thus for the general situation shown in Fig. 2 the factorization theorem becomes

$$\begin{aligned} \frac{d^2\sigma}{dM_t^2 dM_{\bar{t}}^2} = {}& \sigma_0 H_Q(Q, \mu_m) H_m\Big(m, \frac{Q}{m}, \mu_m, \mu_\Gamma\Big) \int_{-\infty}^{\infty} d\ell^+ d\ell^- \\ & \times \int_{-\infty}^{\infty} d\ell'^+ d\ell'^- U_S(\ell'^+, \ell'^-, \mu_\Gamma, \mu_\Lambda) \\ & \times B_+\Big(\hat{s}_t - \frac{Q\ell^+}{m}, \Gamma, \mu_\Gamma\Big) B_-\Big(\hat{s}_{\bar{t}} - \frac{Q\ell^-}{m}, \Gamma, \mu_\Gamma\Big) \\ & \times S(\ell^+ - \ell'^+, \ell^- - \ell'^-, \mu_\Lambda), \end{aligned} \tag{44}$$

or equivalently

---

[5] In the class of observables we consider this is the case for S, while $J_{n,\bar{n}}$ and $B_\pm$ are inclusive because they do not depend on the invariant mass prescription which only affects radiation at large angles.

$$\frac{d^2\sigma}{dM_t^2 dM_{\bar t}^2} = \sigma_0 H_Q(Q,\mu_m) H_m\Big(m, \frac{Q}{m}, \mu_m, \mu_\Lambda\Big) \int_{-\infty}^{\infty} d\hat s_t' d\hat s_{\bar t}' U_{B_+}(\hat s_t - \hat s_t', \mu_\Lambda, \mu_\Gamma) U_{B_-}(\hat s_{\bar t} - \hat s_{\bar t}', \mu_\Lambda, \mu_\Gamma) \times \int_{-\infty}^{\infty} d\ell^+ d\ell^- B_+\Big(\hat s_t' - \frac{Q\ell^+}{m}, \Gamma, \mu_\Gamma\Big) B_-\Big(\hat s_{\bar t}' - \frac{Q\ell^-}{m}, \Gamma, \mu_\Gamma\Big) S(\ell^+, \ell^-, \mu_\Lambda). \quad (45)$$

We will always take $\mu_\Gamma > \mu_\Lambda$ (although technically these equations are still valid for the case $\mu_\Lambda > \mu_\Gamma$). The evolution kernels U_B and U_S sum the large logs between μ_Γ and μ_Λ, while the large logs that only affect the overall normalization are summed into H_Q and H_m. In Fig. 2 we display three equivalent ways to sum the large logs, labeled cases (a), (b), and (c). In case (a) we run all terms, from the top-down, from μ_Q down to μ_Γ, and we run the soft function from the bottom-up starting at μ_Λ and ending at μ_Γ. In case (b) we run the soft function from μ_Λ all the way to μ_Q, and the jet functions from μ_Γ to μ_m, and then from μ_m to μ_Q. Applying the consistency equations between μ_Q–μ_m and μ_m–μ_Γ, cases (a) and (b) are equivalent, and both give the result shown in Eq. (44). If we take case (a) and apply the consistency equation between μ_Γ and μ_Λ we obtain another equivalent result, case (c), with the result shown in Eq. (45). We will use case (c) for our analysis.

In the previous section we derived a form of the factorization formula (38), which combines the finite lifetime effects and the nonperturbative effects into an infrared function R. This form gives useful insights for the proper choice of the scales μ_Γ and μ_Λ. In terms of stable jet functions and R in Eq. (39) the resummed factorization theorem in Eq. (45) becomes

$$\frac{d^2\sigma}{dM_t^2 dM_{\bar t}^2} = \sigma_0 H_Q(Q,\mu_m) H_m\Big(m, \frac{Q}{m}, \mu_m, \mu_\Lambda\Big) \int_{-\infty}^{\infty} d\hat s_t' d\hat s_{\bar t}' U_{B_+}(\hat s_t - \hat s_t', \mu_\Lambda, \mu_\Gamma) U_{B_-}(\hat s_{\bar t} - \hat s_{\bar t}', \mu_\Lambda, \mu_\Gamma) \times \int_{-\infty}^{\infty} d\ell^+ d\ell^- B_+^{\Gamma=0}\Big(\hat s_t' - \frac{Q\ell^+}{m_J}, \mu_\Gamma\Big) B_-^{\Gamma=0}\Big(\hat s_{\bar t}' - \frac{Q\ell^-}{m_J}, \mu_\Gamma\Big) R(\ell^+, \ell^-, \Gamma_t, \mu_\Lambda). \quad (46)$$

From the convolution in this result we see that the smearing with R provides important information on the infrared cutoff for the fluctuations described by jet functions, and hence the choice of μ_Γ that minimizes large logs. Likewise, we see from the definition of R in Eq. (39) and the form of the soft function in Eq. (40) that μ_Λ is affected by a smearing caused by nonperturbative effects as well as by the scale $m\Gamma/Q$ in the Breit-Wigner functions. Hence in the peak region we should run down to the scales

$$\mu_\Gamma \simeq \mathcal{O}\Big(\Gamma_t + \frac{Q\Lambda}{m} + \frac{s_{t,\bar t}}{m}\Big), \qquad \mu_\Lambda \simeq \mathcal{O}\Big(\Lambda + \frac{m\Gamma_t}{Q} + \frac{s_{t,\bar t}}{Q}\Big). \quad (47)$$

In principle μ_Γ can be substantially larger than Γ_t depending on the Q/m we are interested in. Also with a very large width (which does not apply for the top quark), μ_Λ could be substantially larger than the hadronic scale, which would allow for a perturbative prediction of the invariant mass distribution in the peak region. For the realistic case of $\Gamma_t \sim 1.5$ GeV the scale where the logs would be strictly minimized is in the nonperturbative regime, and we will specify the soft function at scales $\mu_\Lambda \sim 1$GeV to be close to this regime. In the tail region we have $\hat s \gtrsim \Gamma$ or $\hat s \gg \Gamma$ and the convolution in Eq. (46) sets $\ell^\pm \sim m\hat s_{t,\bar t}/Q \gg \Lambda$, so to sum the large logs in this region we should instead run down to the scales

$$\mu_\Gamma \simeq \mathcal{O}\Big(\frac{s_{t,\bar t}}{m}\Big), \qquad \mu_\Lambda \simeq \mathcal{O}\Big(\frac{s_{t,\bar t}}{Q}\Big). \quad (48)$$

The results above are designed to study situations where $s \ll m^2$, which is important for a precision extraction of the top mass. In our formalism it is also possible to study the cross section in the ultra-tail region, $|M_{t,\bar t} - m_J| \sim m_J$, with renormalization group improvement. This is the closest analog to the resummation for massless event shapes in regions where the jet invariant mass $M^2 \gg Q\Lambda$. In this case we use the SCET factorization theorem in Eq. (13) which is valid as long as $Q^2 \gg m^2, s$. Again we take different renormalization scales for the jet functions (μ_m) and soft function (μ_Δ) as shown in Fig. 3. The SCET factorization theorem in the jet-mass scheme is [here $m_J = m_J(\mu_m)$]

$$\begin{aligned}\frac{d^2\sigma}{dM_t^2 dM_{\bar t}^2} &= \sigma_0 H_Q(Q,\mu_m)\mathcal{M}(m_J,\mu_m)\int_{-\infty}^{\infty} d\ell^+ d\ell^- \int_{-\infty}^{\infty} d\ell'^+ d\ell'^- U_S(\ell'^+, \ell'^- \mu_m, \mu_\Delta) J_n(s_t - Q\ell^+, m_J, \mu_m)\\ &\quad\times J_{\bar n}(s_{\bar t} - Q\ell^-, m_J, \mu_m) S_{\rm part}(\ell^+ - \ell'^+, \ell^- - \ell'^-, \mu_\Delta, m_J)\\ &= \sigma_0 H_Q(Q,\mu_m)\mathcal{M}(m_J,\mu_m) U_{H_Q}^{(5)}(Q,\mu_m,\mu_\Delta)\int_{-\infty}^{\infty} ds_t' ds_{\bar t}' U_J(s_t - s_t', \mu_\Lambda, \mu_m) U_J(s_{\bar t} - s_{\bar t}', \mu_\Lambda, \mu_m)\\ &\quad\times \int_{-\infty}^{\infty} d\ell^+ d\ell^- J_n(s_t' - Q\ell^+, m_J, \mu_m) J_{\bar n}(s_{\bar t}' - Q\ell^-, m_J, \mu_m) S_{\rm part}(\ell^+, \ell^-, \mu_\Delta, m_J). \end{aligned} \tag{49}$$

With analogy to the discussion above we show three equivalent ways to sum the large logs in Fig. 3, cases (a), (b), and (c). Here cases (a) and (b) give the first result displayed in Eq. (49) and are related by applying the consistency equation between μ_Q and μ_m. Case (c) gives the second result in Eq. (49) and is related to case (a) by using the consistency condition between μ_m and μ_Δ. In the region below m where top bubbles have been integrated out we have $n_f = 5$ active flavors, so $n_f = 5$ for U_S in case (a), and $n_f = 5$ for $U_{H_Q}^{(5)}(\mu_m, \mu_\Delta)$ and U_J in case (c). For $H_Q(Q, \mu_m)$ we always have $n_f = 6$. In the ultra-tail region we generically have $s_{t,\bar t} \sim m^2$, and hence the logs in the jet functions are minimized with $\mu_m \sim m$. The convolution with the soft function involves momenta $\ell^\pm \sim s/Q \sim m^2/Q$, and hence the large logs are summed for $\mu_\Delta \simeq m^2/Q$.

III. RENORMALIZATION AND ANOMALOUS DIMENSIONS

In this section we set up our notation and conventions for renormalization of the quantities defined in Sec. II A in the $\overline{\rm MS}$ scheme. In QCD the vector current is conserved (although in $\overline{\rm MS}$ one must be careful with the definition [63]), but in the effective theory the currents are renormalized. In the running pictured in Fig. 2 we have both local running (anomalous dimensions that depend only on conserved kinematic variables) and convolution running (anomalous dimensions that depend on variables that can be changed by dynamics in another sector). Convolution running involves an integration over anomalous dimensions that are functions. The coefficients H_Q and H_m have local running, while the functions $J_{n,\bar n}$, $B_\pm$, and S have convolution running. In this context an example of local running are the logarithms summed up by the RG evolution of gauge couplings, and an example of convolution running are logs summed by the Altarelli-Parisi evolution equations (which are collinear UV logs in SCET). Another important attribute of these functions is whether their anomalous dimensions involve $\ln(\mu)$ factors and hence sum double Sudakov logarithms. These $\ln(\mu)$ factors are induced by cusp angles involving lightlike Wilson lines [64–69].

Thus, in considering the renormalization-group evolution in SCET and bHQET the physical meaning of the logarithms that are being summed depends on which of four cases we are in: (1) local single logs, (2) local double logs, (3) convolution with single logs, (4) convolution with double logs. In case (1) we have local running without a $\ln(\mu)$ in the anomalous dimension, and the evolution just corresponds to the change of a coupling constant $c(\mu)$ from integrating out virtual effects. This is the standard case, well known from the running of the gauge couplings and of the electroweak effective Hamiltonian of four-quark operators. On the other hand, the UV renormalization in cases (2), (3), (4) are induced by particular types of phase space restrictions on real radiation that are built into the effective theory. In case (2) we have local running with a $\ln(\mu)$ in the anomalous dimension, while in case (3) and (4) we have convolution running without and with a $\ln(\mu)$ in the anomalous dimension, respectively. These cases are discussed further in Appendix D, and will be mentioned as they arise in the analysis below.

A. SCET renormalization

Top-down running.—In SCET we can renormalize the current J_i^μ by switching from a bare to renormalized Wilson coefficient,

$$C^{\rm bare} = Z_c C = C + (Z_c - 1)C, \tag{50}$$

where insertions of $(Z_c - 1)C$ are treated as counterterms that render insertions of the current together with the bare Wilson coefficient UV finite. Field, coupling, and mass renormalization are given by

$$\begin{aligned} \xi_n^{\rm bare} &= Z_\psi^{1/2}\xi_n, & A_n^{\rm bare} &= Z_A^{1/2} A_n,\\ m^{\rm bare} &= m + \delta_m, & g^{\rm bare} &= Z_g \mu^\epsilon g, \end{aligned} \tag{51}$$

and are all identical to those in QCD [3,7,70].[6] For later convenience we also write the mass counterterm as

$$\delta_m = (\delta_m)^{\rm pole} + \delta m, \tag{52}$$

where $(\delta_m)^{\rm pole}$ is the counterterm in the pole scheme, and for mass schemes other than the pole scheme the remainder, $\delta m = m^{\rm pole} - m$, contains finite perturbative corrections. Equations (50) and (51) suffice to cancel all UV divergences involving J_i^μ. The SCET factorization theo-

---

[6] This is true to all orders in α_s because there are no zero-bin subtractions [55] for the collinear two-point functions. To see this note that all soft-loop corrections to these functions vanish in Feynman gauge since $n^2 = 0$. Thus there is no region that is double-counted and would require a subtraction.

rem in Eq. (13) is generated by a time-ordered product of two J_i^μ currents. The factorization theorem shown in Eq. (13) only involves renormalized objects. These depend on the choice of renormalization scheme in SCET, but this dependence cancels out between H_Q, J_n, $J_{\bar n}$, and S. The renormalization-group equation for C and H_Q are

$$\begin{aligned} \mu\frac{d}{d\mu}C(Q,\mu) &= \gamma_c(Q,\mu)C(Q,\mu), \\ \mu\frac{d}{d\mu}H_Q(Q,\mu) &= \gamma_{H_Q}(Q,\mu)H_Q(Q,\mu), \end{aligned} \tag{53}$$

where from Eq. (50) $\gamma_c = -Z_c^{-1}\mu d/d\mu Z_c$, and since $H_Q = |C|^2$ we have $\gamma_{H_Q} = \gamma_c + \gamma_c^*$. Since the current J_i^μ involves lightlike Wilson lines in the n and $\bar n$ direction, the anomalous dimension has a $\ln(\mu/Q)$ cusp-anomalous dimension term. The general form is

$$\gamma_{H_Q}(Q,\mu) = \Gamma_{H_Q}[\alpha_s]\ln\Big(\frac{\mu^2}{Q^2}\Big) + \gamma_{H_Q}[\alpha_s]. \tag{54}$$

The running of H_Q is in case (2) and sums local double logs. Here the current is affected by small invariant mass phase space restrictions imposed on real radiation, which leads to an incomplete cancellation of real and virtual contributions from soft and collinear effects. Once we integrate out virtual effects in the EFT and evolve the current down to the scale of these restrictions the cancellation again becomes effective. This is manifest through the elimination of large logarithms in EFT matrix elements at the low scale. The process of integrating out virtual effects and performing the RG evolution sums double logs between the production scale Q and scale of the phase space restrictions. For the solution to the RGE equation for H_Q we write

$$H_Q(Q,\mu) = H_Q(Q,\mu_Q)U_{H_Q}(Q,\mu_Q,\mu), \tag{55}$$

where $H_Q(Q,\mu_Q)$ is the matching condition at the hard scale of order Q and $U_{H_Q}(\mu_Q,\mu)$ the evolution factor with $\mu_Q > \mu$. The evolution contained in U_H is illustrated in Fig. 2.

Bottom-up running.—It is well known that there is an alternative but equivalent way to renormalize composite operators like J_i^μ, which is often referred to as operator renormalization (see Ref. [71] for a review). In this approach the UV divergences in matrix-element insertions of the bare operators are absorbed into the renormalization Z-factors multiplying UV-finite renormalized operators, $(J_i^\mu)^{\rm bare} = Z_J J_i^\mu$. The equivalence of the two approaches implies that $Z_J = (Z_c^{-1})^T$, where the transpose is only relevant in the case of a multidimensional operator basis.

Here we consider a variant of operator renormalization that introduces Z-factors for the objects J_n, $J_{\bar n}$, and S in the SCET factorization theorem, Eq. (13). We will refer to this procedure as factorized operator renormalization. In Sec. II A these objects were defined by matrix elements of time-ordered products of fields, where each involves a subset of the fields contained in the current J_i^μ. To switch from bare to renormalized matrix elements we write

$$\begin{aligned} J_{n,\bar n}^{\rm bare}(s) &= \int ds' Z_{J_{n,\bar n}}(s-s',\mu)J_{n,\bar n}(s',\mu), \\ S^{\rm bare}(\ell^+,\ell^-) &= \int d\ell'^+ d\ell'^- Z_S(\ell^+-\ell'^+,\ell^--\ell'^-,\mu) \\ &\quad\times S(\ell'^+,\ell'^-,\mu). \end{aligned} \tag{56}$$

These equations can be inverted using $\int ds Z_{J_n}^{-1}(s''-s)Z_{J_n}(s-s') = \delta(s''-s')$, etc. Note that the Z-factors only depend on differences of momenta because the renormalization is local for position space fields (as discussed further in Appendix D). The RGE's read

$$\begin{aligned} \mu\frac{d}{d\mu}J_{n,\bar n}(s,\mu) &= \int ds'\gamma_{J_{n,\bar n}}(s-s',\mu)J_{n,\bar n}(s',\mu), \\ \mu\frac{d}{d\mu}S(\ell^+,\ell^-,\mu) &= \int d\ell'^+ d\ell'^-\gamma_S(\ell^+-\ell'^+,\ell^--\ell'^-,\mu)S(\ell'^+,\ell'^-,\mu), \end{aligned} \tag{57}$$

with the anomalous dimensions being defined as

$$\begin{aligned} \gamma_{J_{n,\bar n}}(s-s',\mu) &= -\int ds'' Z_{J_{n,\bar n}}^{-1}(s-s'',\mu)\mu\frac{d}{d\mu}Z_{J_{n,\bar n}}(s''-s',\mu), \\ \gamma_S(\ell^+-\ell'^+,\ell^--\ell'^-,\mu) &= -\int d\ell''^+ d\ell''^- Z_S^{-1}(\ell^+-\ell''^+,\ell^--\ell''^-,\mu)\mu\frac{d}{d\mu}Z_S(\ell''^+-\ell'^+,\ell''^--\ell'^-,\mu). \end{aligned} \tag{58}$$

Renormalizability of the theory requires that they are finite as $\epsilon \rightarrow 0$, and the general form for these anomalous dimensions is discussed in Appendix D. For the solutions of the RGE's we write

$$J_{n,\bar{n}}(s,\mu) = \int ds' U_J(s-s',\mu,\mu_0) J_{n,\bar{n}}(s',\mu_0),$$
$$S(\ell^+,\ell^-,\mu) = \int d\ell'^+ d\ell'^- U_S(\ell^+ - \ell'^+, \ell^- - \ell'^-, \mu, \mu_0) S(\ell'^+,\ell'^-,\mu_0). \tag{59}$$

Note that depending on the setup of scales, as illustrated in Fig. 2, the evolution kernels U_J and U_S evolve to higher scales ($\mu > \mu_0$) or to lower scales ($\mu < \mu_0$).

At any order in α_s the anomalous dimensions in Eq. (58) have the general form

$$\gamma_F(t-t',\mu) = -\frac{2\Gamma[\alpha_s]}{j\mu^j}\left[\frac{\mu^j \theta(t-t')}{t-t'}\right]_+ + \gamma[\alpha_s]\delta(t-t'), \tag{60}$$

where j is the dimension of the convolution variable t'. Although the soft function anomalous dimension has two variables, we will show below in Sec. III C that it can be written as

$$\gamma_S(\ell^+,\ell^-) = \delta(\ell^+)\gamma_s(\ell^-) + \delta(\ell^-)\gamma_s(\ell^+), \tag{61}$$

where γ_s has the form in Eq. (60). Equation (60) involves a plus function, which we define by the limit in Eq. (C1). This is similar to the Altarelli-Parisi kernel in deep-inelastic scattering, except for the presence of μ^j. This explicit dependence on μ must appear to make the plus function dimensionless, and using Eq. (C3) can be written as a $\ln(\mu)$ factor multiplying a $\delta(t-t')$. Thus they sum double logs, making them fall in case (4), which is a combination of case (2) described above and case (3). For case (3) the real and virtual effects cancel for the soft contributions, but not for collinear ones, leaving single logarithms to be summed by the RGE's. The convolution with plus functions arises because there are angular restrictions on the radiation such as those that occur when an energetic proton state absorbs partons in deep inelastic scattering (DIS). Summing logs in this case involves a convolution since the logarithms generated by the collinear effects depend on a momentum fraction.

Viewed from the bottom-up each of the jet and soft functions in our factorization theorem has an evolution equation corresponding to case (4). However, in SCET when the soft function and collinear jets are combined in the factorization theorem their convoluted product no longer has angular restrictions. So the evolution of the product does not involve a convolution. The product still restricts the radiation to small invariant mass and so falls into case (2), of local running with double logs as we mentioned above.

B. bHQET renormalization

Top-down running.—Next we discuss the renormalization in bHQET. The renormalization constant for the bHQET current for the counterterm method is defined as

$$C_m^{\rm bare} = Z_{C_m} C_m = C_m + (Z_{C_m} - 1)C_m. \tag{62}$$

While gluon field and coupling renormalization in HQET and QCD are equivalent, the top-quark field renormalization differs, with $h_v^{\rm bare} = Z_h^{1/2} h_v$. The bHQET factorization theorem in Eq. (3) is generated by a time-ordered product of two $J^\mu_{\rm bHQET}$ currents [2]. The soft graphs in bHQET are identical to those in SCET up to top-quark vacuum polarization graphs [2], and the infrared divergences of the collinear graphs in SCET exactly match those in bHQET. The mass-mode function $\mathcal{M}$ is IR finite and just enters in the H_m matching coefficient. Thus, the same cancellation between collinear and soft graphs that yielded local running in SCET also occurs in bHQET. So the running of C_m is also local. We will demonstrate this explicitly in the one-loop computations shown below.

Next recall that the + and − bHQET sectors are decoupled, so the anomalous dimension for C_m can only depend on the quantities $\bar{n}\cdot v_- = Q/m$, $n\cdot v_+ = Q/m$, and $n\cdot\bar{n} = 2$. With this theory we are interested in studying small invariant mass fluctuations *around* the top-quark mass m. Thus the renormalization-group evolution is not related to stronger kinematic restrictions on the magnitude of the overall invariant mass of top plus lighter degrees of freedom. Here the evolution falls into case (1) rather than case (2). However, the anomalous dimension of the bHQET current $J^\mu_{\rm bHQET}$ still contains a remnant of the $\ln(\mu/Q)$ term in Eq. (54) in the form of a dependence on $\ln(m/Q)$. This μ-independent logarithmic term is related to a cusp between Wilson lines. This can be made explicit through the field redefinition $h_{v_\pm} \to W_{v_\pm} h^{(0)}_{v_\pm}$, where $W_{v_\pm}$ are Wilson lines defined in analogy to Eq. (23) and $h^{(0)}_{v_\pm}$ are heavy quark fields that no longer couple to gluon fields at leading power. For the operator $\bar{h}_{v_+} W_n(0)$ that appears, for example, in the bHQET current of Eq. (27) this leads to $\bar{h}^{(0)}_{v_+} W^\dagger_{v_+} W_n(0)$. Insertions of this operator lead to the anomalous dimension depending on logarithms of the cusp angle $n\cdot v_+ = Q/m$. [50,72,73]. Unlike SCET, this angle is fixed and independent of μ because the overall invariant mass is $\sim m^2$ and does not become parametrically smaller from the RG evolution.

The RG equations for C_m and $H_m = |C_m|^2$ are

$$\mu\frac{d}{d\mu}C_m\left(m,\frac{Q}{m},\mu\right) = \gamma_{C_m}\left(\frac{Q}{m},\mu\right)C_m\left(m,\frac{Q}{m},\mu\right),$$
$$\mu\frac{d}{d\mu}H_m\left(m,\frac{Q}{m},\mu\right) = \gamma_{H_m}\left(\frac{Q}{m},\mu\right)H_m\left(m,\frac{Q}{m},\mu\right), \tag{63}$$

where $\gamma_{C_m} = -Z^{-1}_{C_m}\mu d/d\mu Z_{C_m}$ and $\gamma_{H_m} = \gamma_{C_m} + \gamma^*_{C_m}$, and the general form of the anomalous dimension is

$$\gamma_{H_m}(Q/m,\mu) = \Gamma_{H_m}[\alpha_s]\ln\left(\frac{m^2}{Q^2}\right) + \gamma_{H_m}[\alpha_s]. \quad (64)$$

We write the solution to Eq. (63) as

$$H_m\left(m,\frac{Q}{m},\mu_m,\mu\right) = H_m(m,\mu_m)U_{H_m}\left(\frac{Q}{m},\mu_m,\mu\right), \quad (65)$$

where $H_m(m,\mu_m)$ is the matching condition of the bHQET current at the SCET-bHQET matching scale $\mu_m \sim m$ and $U_{H_m}(Q/m,\mu_m,\mu)$ is the evolution factor describing the running to a scale $\mu < \mu_m$. The local evolution generated by U_{H_m} is illustrated in Fig. 2. Note that the right-hand side (RHS) of Eq. (65) is not μ_m independent at the order one is working, since part of this dependence is canceled by the $U_Q(\mu_Q,\mu_m)$ in $H_Q(Q,\mu_m)$. This is indicated by the μ_m argument on the left-hand side (LHS) of Eq. (65).

Bottom-up running.—Next consider the equivalent approach of factorized operator renormalization in bHQET. In this case we introduce Z-factors for the jet functions $B_\pm$ and the soft function S rather than counterterm contributions for the bHQET current. The resulting evolution equations for the soft function S agree with those in SCET except for the change from $n_f = 6$ to $n_f = 5$, and will not be repeated. To switch from bare to renormalized HQET jet functions we write

$$B_\pm^{\rm bare}(\hat s) = \int d\hat s' Z_{B_\pm}(\hat s - \hat s',\mu)B_\pm(\hat s',\mu), \quad (66)$$

where $\int d\hat s Z_{B_\pm}^{-1}(\hat s'' - \hat s,\mu)Z_{B_\pm}(\hat s - \hat s',\mu) = \delta(\hat s'' - \hat s')$. The RG equations are

$$\mu\frac{d}{d\mu}B_\pm(\hat s,\mu) = \int d\hat s' \gamma_{B_\pm}(\hat s - \hat s',\mu)B_\pm(\hat s',\mu), \quad (67)$$

with anomalous dimension

$$\gamma_{B_\pm}(\hat s - \hat s',\mu) = -\int d\hat s'' Z_{B_\pm}^{-1}(\hat s - \hat s'',\mu)\mu \times \frac{d}{d\mu}Z_{B_\pm}(\hat s'' - \hat s',\mu). \quad (68)$$

The general form for this anomalous dimension can be found in Appendix D. For the solutions to the RGE we write

$$B_\pm(\hat s,\mu) = \int d\hat s' U_B(\hat s - \hat s',\mu,\mu_\Gamma)B_\pm(\hat s',\mu_\Gamma). \quad (69)$$

The evolution kernels U_B take us from the low-scale μ_Γ to a scale μ. Depending on the setup of scales, as shown in Fig. 2, we can have $\mu > \mu_\Gamma$ or $\mu < \mu_\Gamma$.

C. Consistency conditions in SCET and bHQET

In this section we derive the factorization of the soft function evolution factor in Eq. (42) and the SCET and bHQET consistency equations quoted above in Eq. (43).

Using Eq. (56) we can obtain a finite result for the SCET factorization theorem by determining the UV divergences for the Z-factors $Z_{J_{n,\bar n}}$ and Z_S from each individual SCET Feynman diagram contributing to $J_{n,\bar n}$ and S. If we instead use the counterterm method with the current renormalization factor Z_c then a consistent form for the counterterm is only obtained once all collinear and soft vertex graphs that contribute to the factorization theorem at some order in α_s are added up. Since the two methods render UV-finite results and lead to the same predictions, there is a consistency relation between the renormalization constants for the operator and the counterterm renormalization method which is very useful for practical computations. To derive it we start with Eq. (13) and switch to $J_n^{\rm bare}$, $J_{\bar n}^{\rm bare}$, and $S^{\rm bare}$ using first counterterm renormalization and then factorized operator renormalization. Equating the results we find that

$$\begin{aligned}|Z_c|^2\delta(s - Q\ell'^+)\delta(\bar s - Q\ell'^-) &= \int d\ell^+ d\ell^- Z_{J_n}^{-1}(s - Q\ell^+)Z_{J_{\bar n}}^{-1}(\bar s - Q\ell^-)\\ &\quad\times Z_S^{-1}(\ell^+ - \ell'^+,\ell^- - \ell'^-). \end{aligned} \quad (70)$$

The consistency condition can also be written in terms of the evolution kernels that solve the individual RGE's. To derive this form we consider the factorization theorem Eq. (13) at the scale μ_0, and use $H_Q(Q,\mu_0) = H_Q(Q,\mu)U_{H_Q}(\mu,\mu_0)$. Then we write down the factorization theorem Eq. (13) again at the scale μ and relate the $J_{n,\bar n}$ and S at the scale μ to those evaluated at μ_0 using Eqs. (59). Equating the two results gives the consistency condition

$$\begin{aligned}&U_{H_Q}(Q,\mu,\mu_0)\delta(s - Q\ell'^+)\delta(\bar s - Q\ell'^-)\\ &= \int d\ell^+ d\ell^- U_{J_n}(s - Q\ell^+,\mu,\mu_0)U_{J_{\bar n}}(\bar s - Q\ell^-,\mu,\mu_0)\\ &\quad\times U_S(\ell^+ - \ell'^+,\ell^- - \ell'^-,\mu,\mu_0). \end{aligned} \quad (71)$$

Next we multiply Eq. (71) by $U_J(Q\ell'^\pm,\mu_0,\mu)$, shift $\ell^\pm \to \ell^\pm + \ell'^\pm$, and integrate over $\ell'^\pm$ to turn the products of U_J factors on the RHS into delta functions. Carrying out the $\ell^\pm$ integrals then leaves

$$\begin{aligned}U_S\left(\frac{s}{Q},\frac{\bar s}{Q},\mu,\mu_0\right) &= Q^2 U_{H_Q}(Q,\mu,\mu_0)U_{J_n}(s,\mu_0,\mu)\\ &\quad\times U_{J_{\bar n}}(\bar s,\mu_0,\mu). \end{aligned} \quad (72)$$

This implies a separable structure for U_S to all orders in perturbation theory, so we write

$$U_S(\ell^+,\ell^-,\mu,\mu_m) = U_s(\ell^+,\mu,\mu_m)U_s(\ell^-,\mu,\mu_m). \quad (73)$$

This result for U_S implies

$$
\begin{aligned}
\mu\frac{d}{d\mu}U_S(\ell^+,\ell^-) &= \Big[\mu\frac{d}{d\mu}U_s(\ell^+)\Big]U_s(\ell^-) \\
&\quad + U_s(\ell^+)\Big[\mu\frac{d}{d\mu}U_s(\ell^-)\Big] \\
&= \int d\ell'^+ d\ell'^-[\gamma_s(\ell^+-\ell'^+) \\
&\quad \times\delta(\ell^- - \ell'^-) + \delta(\ell^+ - \ell'^+) \\
&\quad \times\gamma_s(\ell^- - \ell'^-)]U_s(\ell'^+)U_s(\ell'^-),
\end{aligned}
\tag{74}
$$

so the soft-function anomalous dimension has the general form shown in Eq. (61). Now using the fact that $U_{J_n} = U_{J_{\bar n}} = U_J$, Eqs. (72) and (73) give the final result for the SCET consistency equation

$$
\sqrt{U_{H_Q}(Q,\mu,\mu_0)}\,U_J(s,\mu_0,\mu) = \frac{1}{Q}U_s\Big(\frac{s}{Q},\mu,\mu_0\Big). \tag{75}
$$

This relation expresses the equivalence of running the factorization theorem between μ_Q and μ_m from top-down versus from bottom-up as pictured in Fig. 2. It also states that when the convolution RGE's for each of J_n, $J_{\bar n}$, and S are combined as shown in the factorization theorem, the result is local running through U_{H_Q} without a convolution. This means, in particular, that the renormalization-group evolution of the soft function does not depend on the phase space constraints that are imposed dividing up the soft radiation in M_t and $M_{\bar t}$. This is verified explicitly at $\mathcal{O}(\alpha_s)$ in Sec. IV D where we show that the anomalous dimension of the soft function is unchanged if invariant mass prescriptions are applied that differ from the hemisphere prescription.

Next let us derive the consistency equation in bHQET. Again the use of the factorized operator renormalization using $Z_{B_\pm}$ and Z_S correspond to determining the UV divergences of the individual Feynman diagrams contributing to B_+, B_-, and S. If we instead use current renormalization via Z_{C_m} then the consistent form of the counterterm is only obtained once all vertex graphs contributing to the factorization theorem at a certain order in α_s are added up. In analogy to SCET this leads to consistency conditions for the renormalization factors and the solutions of the anomalous dimensions. The derivation goes along the same lines as in the SCET case, but starting from Eq. (3). The consistency condition for the renormalization factors is

$$
\begin{aligned}
&|Z_{C_m}|^2\delta\Big(\hat s - \frac{Q\ell'^+}{m}\Big)\delta\Big(\hat{\bar s} - \frac{Q\ell'^-}{m}\Big) \\
&\quad = \int d\ell^+ d\ell^- Z^{-1}_{B_+}\Big(\hat s - \frac{Q\ell^+}{m}\Big)Z^{-1}_{B_-}\Big(\hat{\bar s} - \frac{Q\ell^-}{m}\Big) \\
&\qquad \times Z_S^{-1}(\ell^+ - \ell'^+, \ell^- - \ell'^-),
\end{aligned}
\tag{76}
$$

and for the evolution kernels reads

$$
\begin{aligned}
&U_{H_m}\Big(\frac{Q}{m},\mu,\mu_0\Big)\delta\Big(\hat s - \frac{Q\ell'^+}{m}\Big)\delta\Big(\hat{\bar s} - \frac{Q\ell'^-}{m}\Big) \\
&\quad = \int d\ell^+ d\ell^- U_{B_+}\Big(\hat s - \frac{Q\ell^+}{m},\mu,\mu_0\Big) \\
&\qquad \times U_{B_-}\Big(\hat{\bar s} - \frac{Q\ell^-}{m},\mu,\mu_0\Big) \\
&\qquad \times U_S(\ell^+ - \ell'^+, \ell^- - \ell'^-, \mu, \mu_\Lambda).
\end{aligned}
\tag{77}
$$

Removing the δ-functions and integrals in an analogous manner to what we did for SCET above, we obtain the final bHQET consistency condition

$$
\sqrt{U_{H_m}\Big(\frac{Q}{m},\mu,\mu_0\Big)}\,U_B(\hat s,\mu_0,\mu) = \frac{m}{Q}U_s\Big(\frac{m\hat s}{Q},\mu,\mu_0\Big). \tag{78}
$$

This result expresses the equivalence of running the factorization theorem between μ_m and μ_Λ using either a top-down or bottom-up approach, as illustrated in Fig. 2. It also states that when the convolution RGE's for each of B_+, B_-, and S are combined as shown in the factorization theorem that the result is local running for H_m through U_{H_m} without a convolution.

These consistency conditions are important phenomenologically because they state that the RG evolution from the hard scales down to a common low energy scale for jet and soft functions does not affect the shape of the invariant mass distributions. Since we have a consistency condition in both SCET and bHQET the mass scale m does not affect this protection of the invariant mass shape from large log modification. The smooth transition between the SCET and bHQET consistency conditions is related to a correspondence between geometry and the dimension of the variables in the factorization theorem, as we discuss in Appendix D. Once the $B_\pm$ jet functions reach the scale μ_Γ where their logs are minimized, then further evolution of the soft function to μ_Λ generates logs that affect the shape of the invariant mass distribution.

D. NLL resummation

To sum large logarithms to NLL we must solve Eq. (54) for U_{H_Q}, Eq. (60) for U_F, and Eq. (64) for U_{H_m}. As discussed in Appendix D the general solutions are

$$
\begin{aligned}
U_{H_Q}(Q,\mu_0,\mu) &= e^K\Big(\frac{\mu_0^2}{Q^2}\Big)^\omega, \\
U_{H_m}\Big(\frac{Q}{m},\mu_0,\mu\Big) &= e^{K_\gamma}\Big(\frac{m^2}{Q^2}\Big)^\omega, \\
U_F(t-t',\mu,\mu_0) &= \frac{e^K(e^{\gamma_E})^\omega}{\mu_0^j\Gamma(-\omega)}\Big[\frac{(\mu_0^j)^{1+\omega}\theta(t-t')}{(t-t')^{1+\omega}}\Big]_+.
\end{aligned}
\tag{79}
$$

Here $\omega = \omega(\mu,\mu_0)$, $K = K(\mu,\mu_0)$, and $K_\gamma = K_\gamma(\mu,\mu_0)$ are solutions to the integrals in Eq. (D8). Note that for ω,

TABLE I. Dimension j and anomalous dimensions $\Gamma[\alpha_s]$, Γ_0, γ_0, and Γ_1 for the hard, jet, and soft functions in SCET and bHQET using the notation in Eqs. (80) and (81). Values for the one and two-loop cusp-anomalous dimensions [74] are shown. For each case our notation for the resummation functions ω and K is also given.

	F	j	$\Gamma_F[\alpha_s]$	Γ_0	γ_0	Γ_1	ω	K
SCET hard function	H_Q	2	$-2\Gamma^{\rm cusp}[\alpha_s]$	$-8C_F$	$-12C_F$	$-2\Gamma_1^{\rm cusp}$	ω_0	K_0
SCET jet function	$J_{n,\bar n}$	2	$2\Gamma^{\rm cusp}[\alpha_s]$	$8C_F$	$6C_F$	$2\Gamma_1^{\rm cusp}$	ω_1	K_1
Soft hemisphere function	S	1	$-\Gamma^{\rm cusp}[\alpha_s]$	$-4C_F$	0	$-\Gamma_1^{\rm cusp}$	ω_2	K_2
bHQET jet function	$B_\pm$	1	$\Gamma^{\rm cusp}[\alpha_s]$	$4C_F$	$4C_F$	$\Gamma_1^{\rm cusp}$	ω_1	K_3
bHQET hard function	H_m	2	$-2\Gamma^{\rm cusp}[\alpha_s]$	$-8C_F$	$-8C_F$	$-2\Gamma_1^{\rm cusp}$	ω_0	K_{00}
		$\Gamma_0^{\rm cusp} = 4C_F$, $\Gamma_1^{\rm cusp} = 4C_F[(\frac{67}{9}-\frac{\pi^2}{3})C_A - \frac{10n_f}{9}]$						

K, and K_γ we use the notation that the first argument μ is always the final scale of the evolution while the second argument μ_0 is always the initial scale. This notation is also chosen for the U_F evolution factors of the soft and jet functions, but differs from our notation for the evolution factors for the current Wilson coefficients, U_{H_Q} and U_{H_m} where the opposite ordering is used. Thus writing

$$\Gamma[\alpha_s] = \frac{\alpha_s(\mu)}{4\pi}\Gamma_0 + \left[\frac{\alpha_s(\mu)}{4\pi}\right]^2\Gamma_1 + \ldots,$$
$$\gamma[\alpha_s] = \frac{\alpha_s(\mu)}{4\pi}\gamma_0 + \left[\frac{\alpha_s(\mu)}{4\pi}\right]^2\gamma_1 + \ldots, \qquad (80)$$

we must determine Γ_0, Γ_1, and γ_0. The determination of Γ_0 and γ_0 from one-loop diagrams is discussed in Secs. IV and V below, and the results are summarized in Table I. To determine Γ_1 we make use of the fact that to all orders in perturbation theory $\Gamma[\alpha_s]$ is proportional to the cusp-anomalous dimension, $\Gamma[\alpha_s] \propto \Gamma^{\rm cusp}[\alpha_s]$. The constant of proportionality is also determined by the one-loop computations and is summarized in Table I. At two-loop order the cusp-anomalous dimension has the form

$$\Gamma^{\rm cusp}[\alpha_s] = \frac{\alpha_s(\mu)}{4\pi}\Gamma_0^{\rm cusp} + \left[\frac{\alpha_s(\mu)}{4\pi}\right]^2\Gamma_1^{\rm cusp} + \ldots, \qquad (81)$$

with results for $\Gamma_0^{\rm cusp}$ and $\Gamma_1^{\rm cusp}$ also shown in Table I. For QCD $C_A = 3$, $C_F = 4/3$, and we have n_f flavors. Solving Eq. (D8) also requires the two-loop β-function

$$\mu\frac{d}{d\mu}\alpha_s(\mu) = \beta[\alpha_s]$$
$$= -2\alpha_s(\mu)\left\{\frac{\alpha_s(\mu)}{4\pi}\beta_0 + \left[\frac{\alpha_s(\mu)}{4\pi}\right]^2\beta_1 + \ldots\right\}, \qquad (82)$$

where

$$\beta_0 = 11C_A/3 - 2n_f/3,$$
$$\beta_1 = 34C_A^2/3 - 10C_An_f/3 - 2C_Fn_f. \qquad (83)$$

Defining

$$r = \frac{\alpha_s(\mu)}{\alpha_s(\mu_0)}, \qquad (84)$$

and substituting Eqs. (80) and (82) into the integrals in Eq. (D8) gives

$$\omega(\mu,\mu_0) = -\frac{\Gamma_0}{j\beta_0}\left[\ln(r) + \left(\frac{\Gamma_1}{\Gamma_0} - \frac{\beta_1}{\beta_0}\right)\frac{\alpha_s(\mu_0)}{4\pi}(r-1)\right],$$
$$K_\gamma(\mu,\mu_0) = -\frac{\gamma_0}{2\beta_0}\ln r,$$
$$K(\mu,\mu_0) = \frac{-2\pi\Gamma_0}{\beta_0^2}\left\{\frac{(r-1-r\ln r)}{\alpha_s(\mu)} + \frac{\gamma_0\beta_0}{4\pi\Gamma_0}\ln r + \left(\frac{\Gamma_1}{\Gamma_0} - \frac{\beta_1}{\beta_0}\right)\frac{(1-r+\ln r)}{4\pi} + \frac{\beta_1}{8\pi\beta_0}\ln^2 r\right\}. \qquad (85)$$

Taken together with Eq. (79) and the appropriate values for Γ_0, γ_0, and Γ_1 from Table I, this determines the NLL-evolution kernels.

IV. SCET RESULTS

A. Current matching and running in SCET

To determine the Wilson coefficient C of Eq. (10) we match renormalized QCD and SCET S-matrix elements, which we will simply call amplitudes in the following. The QCD vertex graphs are given in Fig. 4 where momenta p and $\bar p$ are defined. We use dimensional regularization for UV divergences and small off-shell momenta to regulate the IR divergences, letting $p^2 - m^2 = \bar p^2 - m^2 = \Delta^2 \neq 0$. Since the SCET current should reproduce the infrared physics of the QCD current, we can perform the matching

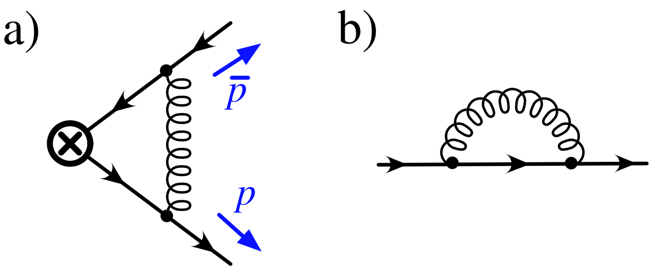

FIG. 4 (color online). One-loop vertex corrections in QCD.

with arbitrary external states and for any infrared regulator, as long as the same IR regulators are used in the full and effective theories. The values obtained for the Wilson coefficients will be independent of the choice of IR regulator.

Results for the QCD graphs in Fig. 4 are summarized in Eq. (A1) of Appendix A. The result for the amplitude includes the vertex graph, $\overline{\rm MS}$ wave function contributions, and the residue term, $V_{4a} + \Gamma_i^\mu(Z_\psi - 1) + \Gamma_i^\mu(R_\psi - 1)$, where the subscript 4a on the V indicates that it is the result for Fig. 4(a). The form of the residue term is required to ensure consistency with physical S-matrix elements. We work in the limit $\Delta^2 \ll m^2 \ll Q^2$. The QCD amplitude is

$$\langle p, \bar{p}|\mathcal{J}_i^\mu|0\rangle_{\rm QCD} = \Gamma_i^\mu\bigg[1 + \frac{\alpha_s C_F}{4\pi}\bigg\{2\ln^2\bigg(\frac{-Q^2}{m^2}\bigg) - 4\ln\bigg(\frac{-Q^2}{m^2}\bigg)\ln\bigg(\frac{Q^2}{\Delta^2}\bigg) + 3\ln\bigg(\frac{-Q^2}{m^2}\bigg) + 4\ln\bigg(\frac{m^2}{-\Delta^2}\bigg) + \frac{2\pi^2}{3}\bigg\}\bigg], \tag{86}$$

where for simplicity we use the shorthand notation Δ^2 and Q^2 for $\Delta^2 + i0$ and $Q^2 + i0$, respectively. For the SCET computation we have the graphs in Fig. 5 which are evaluated in Eqs. (A5) and (A6) of Appendix A with nonzero $\Delta^2 = p^2 - m^2$ and $\bar{\Delta}^2 = \bar{p}^2 - m^2$. The sum of collinear and soft vertex graphs, wave function contribution, and residue is $V_{5a} + V_{5b} + V_{5c} + \Gamma_i^\mu(Z_\xi - 1) + \Gamma_i^\mu(R_\xi - 1)$. For $\bar{\Delta} = \Delta > 0$ and again taking the limit $\Delta^2 \ll m^2 \ll Q^2$ we obtain

$$\langle p, \bar{p}|J_i^\mu|0\rangle_{\rm SCET} = \Gamma_i^\mu\bigg[1 + \frac{\alpha_s C_F}{4\pi}\bigg\{\frac{2}{\epsilon^2} + \frac{3}{\epsilon} + \frac{2}{\epsilon}\ln\bigg(\frac{\mu^2}{-Q^2}\bigg) + 2\ln^2\bigg(\frac{\mu^2}{-\Delta^2}\bigg) + 2\ln^2\bigg(\frac{m^2}{-\Delta^2}\bigg) - \ln^2\bigg(\frac{\mu^2 Q^2}{(-\Delta^2)(\Delta^2)}\bigg) + 4\ln\bigg(\frac{m^2}{-\Delta^2}\bigg) + 3\ln\bigg(\frac{\mu^2}{m^2}\bigg) + 8 + \frac{\pi^2}{2}\bigg\}\bigg]. \tag{87}$$

The remaining divergences in Eq. (87) are canceled by the current counterterm $Z_C - 1$ giving

$$Z_c = 1 - \frac{\alpha_s C_F}{4\pi}\bigg[\frac{2}{\epsilon^2} + \frac{3}{\epsilon} + \frac{2}{\epsilon}\ln\bigg(\frac{\mu^2}{-Q^2 - i0}\bigg)\bigg]. \tag{88}$$

The running generated by Z_c sums $\ln^2\mu$ terms and falls in case (2) as defined in Sec. III. The renormalized amplitude in SCET then reads

$$\langle p, \bar{p}|Z_c J_i^\mu|0\rangle_{\rm SCET} = \Gamma_i^\mu\bigg[1 + \frac{\alpha_s C_F}{4\pi}\bigg\{2\ln^2\bigg(\frac{\mu^2}{-\Delta^2}\bigg) + 2\ln^2\bigg(\frac{m^2}{-\Delta^2}\bigg) - \ln^2\bigg(\frac{\mu^2 Q^2}{-\Delta^4}\bigg) + 4\ln\bigg(\frac{m^2}{-\Delta^2}\bigg) + 3\ln\bigg(\frac{\mu^2}{m^2}\bigg) + 8 + \frac{\pi^2}{2}\bigg\}\bigg]. \tag{89}$$

Subtracting Eq. (89) from (86) all dependence on the IR scales m and Δ cancels. This is an explicit demonstration that at one-loop massive SCET has the same IR structure as in QCD. Evaluating the difference at the scale $\mu = \mu_Q$ gives the matching condition of the current Wilson coefficient,

$$C(Q, \mu_Q) = 1 + \frac{\alpha_s C_F}{4\pi}\bigg[-\ln^2\bigg(\frac{\mu_Q^2}{-Q^2 - i0}\bigg) - 3\ln\bigg(\frac{\mu_Q^2}{-Q^2 - i0}\bigg) - 8 + \frac{\pi^2}{6}\bigg]. \tag{90}$$

As expected from the limit $Q \gg m$ the matching condition is mass independent and there are no large logarithms for $\mu_Q \simeq Q$.

The result in Eq. (90) is independent of the choice of the IR regulator and should therefore agree with the matching conditions for the massless quark production current. In Ref. [18] the matching coefficient was computed using on-shell massless quarks, and Eq. (90) agrees with their result. With the regulator used in Ref. [18] the SCET diagrams are scaleless and vanish in dimensional regularization. To see more explicitly how the massless computation gives the same matching coefficient we repeat the previous computation with an off-shellness $p^2 = \bar{p}^2 \gg m^2$, where $Q^2 \gg p^2 = \bar{p}^2$. For this case the renormalized one-loop QCD

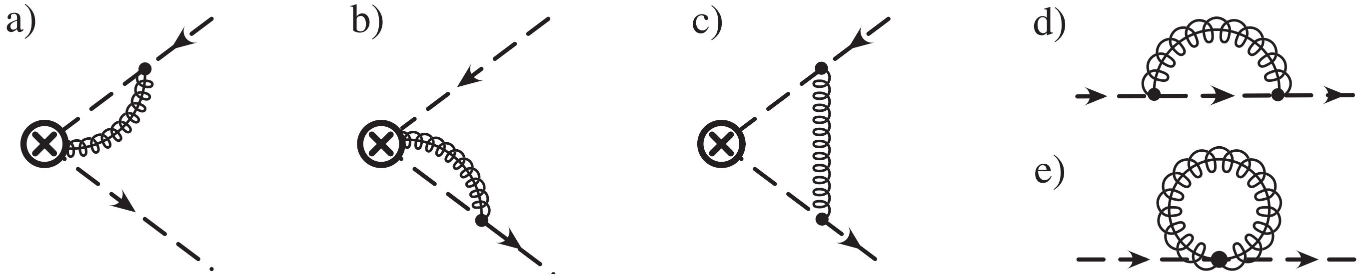

FIG. 5. One-loop vertex and self-energy corrections in massive SCET. Gluons with a line through them are collinear, while those without are soft. The soft-gluon wave function renormalization graph vanishes in Feynman gauge and is not shown.

amplitude is

$$\langle p, \bar{p}|\mathcal{J}_i^\mu|0\rangle|_{\mathrm{QCD}} = \Gamma_i^\mu\biggl[1 + C_F\frac{\alpha_s}{4\pi}\biggl\{-\ln\biggl(\frac{-Q^2}{\mu^2}\biggr) - 2\ln^2\biggl(\frac{p^2}{Q^2}\biggr) - 4\ln\biggl(\frac{p^2}{Q^2}\biggr) - \frac{2\pi^2}{3}\biggr\}\biggr], \tag{91}$$

and from Eqs. (A5) and (A6) the renormalized amplitude in SCET has the form

$$\langle p, \bar{p}|Z_c J_i^\mu|0\rangle_{\mathrm{SCET}} = \Gamma_i^\mu\biggl[1 + \frac{\alpha_s C_F}{4\pi}\biggl\{2\ln^2\biggl(\frac{\mu^2}{-p^2}\biggr) - \ln^2\biggl(\frac{\mu^2 Q^2}{-p^4}\biggr) + 4\ln\biggl(\frac{\mu^2}{-p^2}\biggr) + 8 - \frac{5\pi^2}{6}\biggr\}\biggr]. \tag{92}$$

To obtain Eq. (92) the current counterterm in Z_C from Eq. (88) was used. Taking the difference of Eqs. (91) and (92) gives exactly Eq. (90), as expected.

The imaginary parts in $C(Q, \mu_Q)$ and the Z-factor in Eq. (88) arise from real QCD intermediate states in the QCD vertex diagram that are not accounted for in the corresponding SCET diagrams. These SCET graphs account only for fluctuations associated to sectors for the n and $\bar{n}$ directions, while the QCD diagrams do not have such a restriction. Note that the complex Z-factor also means that the anomalous dimension γ_C is complex. However, only $|C|^2$ appears in the factorization theorem in Eq. (3) and so the complex phase cancels. This treatment is consistent because in the derivation of the factorization theorem the part of the phase space integration encoded in the sum over the n and $\bar{n}$ directions is carried out explicitly prior to the formulation of the jet and soft functions in SCET. The matching coefficient appearing in the factorization theorem therefore reads

$$\begin{aligned} H_Q(Q, \mu_Q) &= |C(Q, \mu_Q)|^2 \\ &= 1 + \frac{\alpha_s C_F}{4\pi}\biggl[-2\ln^2\biggl(\frac{Q^2}{\mu_Q^2}\biggr) + 6\ln\biggl(\frac{Q^2}{\mu_Q^2}\biggr) - 16 + \frac{7\pi^2}{3}\biggr]. \end{aligned} \tag{93}$$

To evolve the Wilson coefficient to lower scales we need to solve the RG equation in Eq. (53). The anomalous dimensions are obtained from Z_c in Eq. (88) and $\mu d/d\mu\alpha_s = -2\epsilon\alpha_s + \beta(\alpha_s)$,

$$\begin{aligned} \gamma_c(\mu) &= -Z_c^{-1}(\mu)\mu\frac{d}{d\mu}Z_c(\mu) \\ &= -\frac{\alpha_s C_F}{\pi}\biggl[\ln\frac{\mu^2}{-Q^2 - i0} + \frac{3}{2}\biggr], \\ \gamma_{H_Q}(\mu) &= \gamma_c(\mu) + \gamma_c^*(\mu) = -\frac{\alpha_s C_F}{4\pi}\biggl[8\ln\frac{\mu^2}{Q^2} + 12\biggr]. \end{aligned} \tag{94}$$

Comparing this result to Eq. (54) we find $\Gamma_0^{H_Q} = -8C_F$ and $\gamma_0^{H_Q} = -12C_F$ for the coefficients discussed in Sec. III D. Also $\Gamma_{H_Q}[\alpha_s] = -2\Gamma^{\mathrm{cusp}}[\alpha_s]$ and so $\Gamma_1^{H_Q} = -2\Gamma_1^{\mathrm{cusp}}$. The solution for the evolution factor is

$$U_{H_Q}(Q, \mu_Q, \mu) = e^{K_0}\biggl(\frac{\mu_Q^2}{Q^2}\biggr)^{\omega_0}, \tag{95}$$

where $\omega_0 = \omega_0(\mu, \mu_Q)$ and $K_0 = K_0(\mu, \mu_Q)$ are determined at NLL order using Eq. (85) for "ω" and "K." At LL order the solutions are

$$\begin{aligned} \omega_0^{LL}(\mu, \mu_Q) &= \frac{4C_F}{\beta_0}\ln r, \\ K_0^{LL}(\mu, \mu_Q) &= \frac{16\pi C_F}{\beta_0^2}\frac{(r - 1 - r\ln r)}{\alpha_s(\mu)}, \end{aligned} \tag{96}$$

with $r = \alpha_s(\mu)/\alpha_s(\mu_Q)$. Note that solving the RG equation directly for $C(Q, \mu)$ leads to an extra phase factor,

$$C(Q, \mu) = \sqrt{H_Q(Q, \mu)}\biggl[\frac{\alpha_s(\mu)}{\alpha_s(\mu_Q)}\biggr]^{2\pi i(C_F/\beta_0)}, \tag{97}$$

which does not, however, appear in the physical cross section. Its origin is the same as for the phase contained in the current matching condition $C(Q, \mu_Q)$.

B. SCET jet functions and their running

In this section we compute the SCET jet functions J_n and $J_{\bar{n}}$, defined in Eq. (19), perturbatively to $\mathcal{O}(\alpha_s)$. Because of charge conjugation symmetry, the results for J_n and $J_{\bar{n}}$ are identical, so for simplicity we focus on the former. The purpose of the calculation is twofold. First we determine the renormalization factor Z_{J_n}, the anomalous dimension γ_{J_n}, and evolution kernel U_{J_n} for the jet function. Second, the renormalized jet function at the scale $\mu_m \simeq m$ is needed to determine the matching condition of the bHQET jet function, which we work out in Sec. V B below. Since both running and matching do not depend on infrared effects below m we are free to do the computations for stable top quarks. Thus in this section we set the electroweak gauge coupling to zero and neglect finite lifetime effects.

From Eq. (19), the tree-level jet function is simply given by the imaginary part of the collinear propagator:

$$J_n(s, m, \Gamma = 0, \mu)|_{\mathrm{tree}} = \delta(s). \tag{98}$$

At one loop, the jet functions are given by the imaginary part of the diagrams shown in Fig. 6, and results for the individual graphs are summarized in Appendix A. We will consider the one-loop jet function with and without expanding in $s \ll m^2$.

Prior to taking the imaginary part the tree-level graph plus the sum of one-loop graphs from Eq. (A10) give

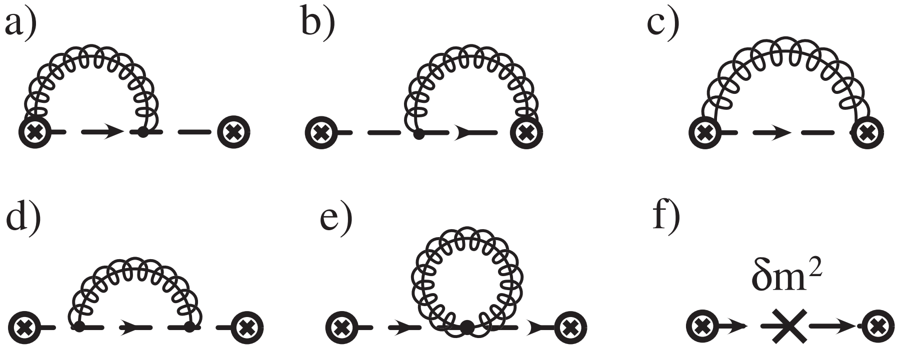

FIG. 6. SCET graphs for the one-loop top-quark jet function. Dashed lines are n-collinear quarks and springs are n-collinear gluons.

$$J_{\rm tree} + J_{6a} + J_{6b} + J_{6c} + J_{6d} + J_{6e} + J_{6f} = \frac{-1}{\pi s} - \frac{2m\delta m}{\pi s^2} - \frac{\alpha_s C_F}{4\pi^2 s}\biggl\{\frac{4}{\epsilon^2} + \frac{4}{\epsilon}\ln\Bigl(\frac{\mu^2}{-s}\Bigr) + \frac{3}{\epsilon} + 2\ln^2\Bigl(\frac{\mu^2}{-s}\Bigr) - 2\ln^2\Bigl(\frac{m^2}{-s}\Bigr) - 4{\rm Li}_2\Bigl(\frac{-s}{m^2}\Bigr) + 3\ln\Bigl(\frac{\mu^2}{-s}\Bigr) + 4\ln\Bigl(\frac{m^2}{-s}\Bigr)\ln\Bigl(\frac{m^2+s}{-s}\Bigr) + \frac{m^2(m^2+2s)}{(s+m^2)^2}\ln\Bigl(\frac{m^2}{-s}\Bigr) - \frac{s}{m^2+s} + 8 + \pi^2\biggr\}, \tag{99}$$

where $s = s + i0$ and $\delta m = m^{\rm pole} - m$. Hence in the pole-mass scheme $\delta m = 0$. The one-loop massive jet function J_n also appears in the computation for $B \to X_c \ell \bar{\nu}$ in the end point region studied in Ref. [75]. Identifying the combination $n_+ \cdot pu'$ in Ref. [75] with our variable s we find agreement with their pole-mass result. Expanding Eq. (99) in $s \ll m^2$ we find

$$[J_{\rm tree} + J_{6a} + J_{6b} + J_{6c} + J_{6d} + J_{6e} + J_{6f}]_{s\ll m^2} = \frac{-1}{\pi s} - \frac{2m\delta m}{\pi s^2} - \frac{\alpha_s C_F}{4\pi^2 s}\biggl\{\frac{4}{\epsilon^2} + \frac{4}{\epsilon}\ln\Bigl(\frac{\mu^2}{-s}\Bigr) + \frac{3}{\epsilon} + 2\ln^2\Bigl(\frac{\mu^2}{-s}\Bigr) + 2\ln^2\Bigl(\frac{m^2}{-s}\Bigr) + 3\ln\Bigl(\frac{\mu^2}{m^2}\Bigr) - 4\ln\Bigl(\frac{-s}{m^2}\Bigr) + 8 + \pi^2\biggr\}. \tag{100}$$

For later convenience we write $s = x\kappa_1^2$ where x is dimensionless and $\kappa_1 > 0$ is a dummy scale with dimensions of mass. Taking the imaginary part of Eq. (99) using the results in Appendix C we find that the bare SCET jet function is

$$J_n^{\rm bare}(s) = \delta(s) - 2m\delta m\delta'(s) + \frac{\alpha_s C_F}{4\pi}\biggl[\delta(s)\biggl\{\frac{4}{\epsilon^2} + \frac{3}{\epsilon} + \frac{4}{\epsilon}\ln\Bigl(\frac{\mu^2}{\kappa_1^2}\Bigr) + 2\ln^2\Bigl(\frac{\mu^2}{\kappa_1^2}\Bigr) + 2\ln^2\Bigl(\frac{m^2}{\kappa_1^2}\Bigr) + 3\ln\Bigl(\frac{\mu^2}{\kappa_1^2}\Bigr) + \ln\Bigl(\frac{m^2}{\kappa_1^2}\Bigr) + 8 - \frac{\pi^2}{3}\biggr\} - \frac{4}{\kappa_1^2}\biggl[\frac{\kappa_1^2\theta(s)}{s}\biggr]_+\biggl\{\frac{1}{\epsilon} + \ln\Bigl(\frac{\mu^2}{\kappa_1^2}\Bigr) + \ln\Bigl(\frac{m^2}{\kappa_1^2}\Bigr) + 1\biggr\} + \frac{8}{\kappa_1^2}\biggl[\frac{\kappa_1^2\theta(s)\ln(s/\kappa_1^2)}{s}\biggr]_+ + \theta(s)\biggl\{\frac{s}{(m^2+s)^2} - \frac{4}{s}\ln\Bigl(1 + \frac{s}{m^2}\Bigr)\biggr\}\biggr]. \tag{101}$$

When we expand Eq. (101) for $s \ll m^2$ all terms have a singular $\mathcal{O}(s^{-1})$ behavior except for the last two $\theta(s)$ terms which are $\mathcal{O}(s^0)$ and can be dropped in the peak region. The result of this expansion agrees with taking the imaginary part of Eq. (100).

To renormalize $J_n^{\rm bare}$ the required jet function Z-factor defined in Eq. (56) is

$$Z_{J_n}(s-s') = \delta(s-s') + \frac{\alpha_s C_F}{4\pi}\biggl\{\delta(s-s')\biggl[\frac{4}{\epsilon^2} + \frac{3}{\epsilon}\biggr] - \frac{4}{\epsilon\mu^2}\biggl[\frac{\mu^2\theta(s-s')}{s-s'}\biggr]_+\biggr\}, \tag{102}$$

which gives the anomalous dimension

$$\gamma_{J_n}(s-s') = -\frac{\alpha_s(\mu)C_F}{4\pi}\biggl\{\frac{8}{\mu^2}\biggl[\frac{\mu^2\theta(s-s')}{s-s'}\biggr]_+ - 6\delta(s-s')\biggr\}. \tag{103}$$

Note that $J_n^{\rm bare}(s)$, $Z_{J_n}(s-s')$ as well as $\gamma_{J_n}(s-s')$ are all independent of the choice for κ_1. The Z-factor and the anomalous dimension also do not depend on the mass scheme that is being employed (determined by δm). Comparing this result to Eq. (60) we find $\Gamma_0^{J_{n,\bar{n}}} = 8C_F$ and $\gamma_0^{J_{n,\bar{n}}} = 6C_F$ for the coefficients discussed in

Sec. III D. Also $\Gamma_{J_{n,\bar{n}}}[\alpha_s] = 2\Gamma^{\mathrm{cusp}}[\alpha_s]$ and so $\Gamma_1^{J_{n,\bar{n}}} = 2\Gamma_1^{\mathrm{cusp}}$. These coefficients give us the NLL-evolution kernel that evolves the jet function from the scale μ_0 to μ:

$$U_{J_n}(s - s', \mu, \mu_0) = \frac{e^{K_1}(e^{\gamma_E})^{\omega_1}}{\Gamma(-\omega_1)\mu_0^2}\left[\frac{\mu_0^{2+2\omega_1}\theta(s - s')}{(s - s')^{1+\omega_1}}\right]_+, \tag{104}$$

where $\omega_1 = \omega_1(\mu, \mu_0)$ and $K_1 = K_1(\mu, \mu_0)$ are determined at NLL order from Eq. (85) with $r = \alpha_s(\mu)/\alpha_s(\mu_0)$. At LL order they are

$$\begin{aligned} \omega_1^{LL}(\mu, \mu_0) &= -\frac{4C_F}{\beta_0}\ln r, \\ K_1^{LL}(\mu, \mu_0) &= -\frac{16\pi C_F}{\beta_0^2}\frac{(r - 1 - r\ln r)}{\alpha_s(\mu)}. \end{aligned} \tag{105}$$

The resummation induced by U_{J_n} falls in case (4), it sums double logs, and involves a convolution.

Finally, taking into account the counterterm in Eq. (102) the renormalized jet function for a stable top quark at $\mathcal{O}(\alpha_s)$ reads

$$\begin{aligned} J_n(s, m, \Gamma = 0, \mu) = {}& \delta(s) - 2m\delta m\delta'(s) + \frac{\alpha_s(\mu)C_F}{4\pi}\left[\delta(s)\left\{2\ln^2\left(\frac{\mu^2}{\kappa_1^2}\right) + 2\ln^2\left(\frac{m^2}{\kappa_1^2}\right) + \ln\left(\frac{m^2}{\kappa_1^2}\right) + 3\ln\left(\frac{\mu^2}{\kappa_1^2}\right) + 8 - \frac{\pi^2}{3}\right\}\right. \\ & \left. + \frac{8}{\kappa_1^2}\left[\frac{\theta(x)\ln(x)}{x}\right]_+ - \frac{4}{\kappa_1^2}\left[\frac{\theta(x)}{x}\right]_+\left\{1 + \ln\left(\frac{m^2}{\kappa_1^2}\right) + \ln\left(\frac{\mu^2}{\kappa_1^2}\right)\right\} + \theta(s)\left\{\frac{s}{(m^2 + s)^2} - \frac{4}{s}\ln\left(1 + \frac{s}{m^2}\right)\right\}\right]. \end{aligned} \tag{106}$$

Here $x = s/\kappa_1^2$ and the result is independent of the choice of κ_1. The last term in Eq. (106) is regular in the small x limit and can be dropped in the peak region. In the ultra-tail region discussed in Appendix F this term generates the "nonsingular" contribution of the SCET function.

From Eq. (106) we can see that for the variable range $s \sim m\Gamma$ further matching and RG evolution is needed for J_n: there is no choice of μ that minimizes all the logarithmic terms. The particular terms in which the large logarithms appear are controlled by the choice of κ_1, but no choice of κ_1 removes them completely. For example, with $\kappa_1 = m$ and $\mu = m$ we still have $\ln(x) \sim \ln(\Gamma/m)$; while for $\kappa_1^2 = m\Gamma$ and $\mu = \kappa_1$ we have $\ln(m^2/\kappa_1^2) \sim \ln(\Gamma/m)$. This motivates the matching onto bHQET and RG evolution between m and Γ to be carried out in Sec. V below. For later convenience we quote the leading result for J_n when $s \ll m^2$ using the choice $\kappa_1 = m$,

$$\begin{aligned} J_n(s, m, \Gamma = 0, \mu)|_{s \ll m^2} = {}& \delta(s) - 2m\delta m\delta'(s) + \frac{\alpha_s(\mu)C_F}{4\pi} \\ & \times\left[\delta(s)\left\{2\ln^2\left(\frac{\mu^2}{m^2}\right) + 3\ln\left(\frac{\mu^2}{m^2}\right)\right.\right. \\ & \left. + 8 - \frac{\pi^2}{3}\right\} + \frac{8}{m^2}\left[\frac{\theta(x)\ln(x)}{x}\right]_+ \\ & \left. - \frac{4}{m^2}\left[\frac{\theta(x)}{x}\right]_+\left\{1 + \ln\left(\frac{\mu^2}{m^2}\right)\right\}\right]. \end{aligned} \tag{107}$$

C. Hemisphere soft function and its running

In this section we determine the $\mathcal{O}(\alpha_s)$ renormalization-group evolution of the hemisphere soft function, $S_{\mathrm{hemi}}(\ell^+, \ell^-, \mu)$ and its renormalized partonic expression from one-loop perturbation theory, $S_{\mathrm{part}}(\ell^+, \ell^-, \mu)$, which is needed to construct the soft-function model defined in Eq. (40). This model builds in the fact that the full nonperturbative S has the same dependence on μ as S_{part}.

For the computation we use the squared matrix-element expression in Eq. (14) for a no-gluon and a single-gluon final state. The corresponding Feynman diagrams are shown in Fig. 7, where the solid lines denote the four Y-Wilson lines. Figure 7(a), 7(b), and 7(g) are the virtual graphs with $|X_s\rangle = |0\rangle$, while Fig. 7(c)–7(f) are the real emission graphs with $|X_s\rangle = |\varepsilon_\mu^A\rangle$. Results for the graphs are summarized in Eq. (A13) of Appendix A. Together with the tree-level matrix element the bare hemisphere soft function reads

$$\begin{aligned} S_{\mathrm{part}}^{\mathrm{bare}}(\ell^+, \ell^-) = {}& \delta(\ell^+)\delta(\ell^-) + \frac{C_F\alpha_s}{\pi}\frac{e^{\epsilon\gamma_E}}{\epsilon\Gamma(1-\epsilon)}\frac{\mu^{2\epsilon}}{\kappa_2^{2\epsilon}} \\ & \times\left[\frac{\delta(\ell^-)\theta(\ell^+)}{\kappa_2}\left(\frac{\kappa_2}{\ell^+}\right)^{1+2\epsilon}\right. \\ & \left. + \frac{\delta(\ell^+)\theta(\ell^-)}{\kappa_2}\left(\frac{\kappa_2}{\ell^-}\right)^{1+2\epsilon}\right]. \end{aligned} \tag{108}$$

Note that $S_{\mathrm{part}}^{\mathrm{bare}}(\ell^+, \ell^-)$ is independent of the dummy mass scale $\kappa_2 > 0$ introduced here. However κ_2 facilitates the application of the standard distribution relation for dimensionless variables

$$\frac{\theta(x)}{x^{1+2\epsilon}} = -\frac{\delta(x)}{2\epsilon} + \left[\frac{\theta(x)}{x}\right]_+ - 2\epsilon\left[\frac{\theta(x)\ln x}{x}\right]_+ + \mathcal{O}(\epsilon^2). \tag{109}$$

The relation leads to the following expression for the bare hemisphere soft function:

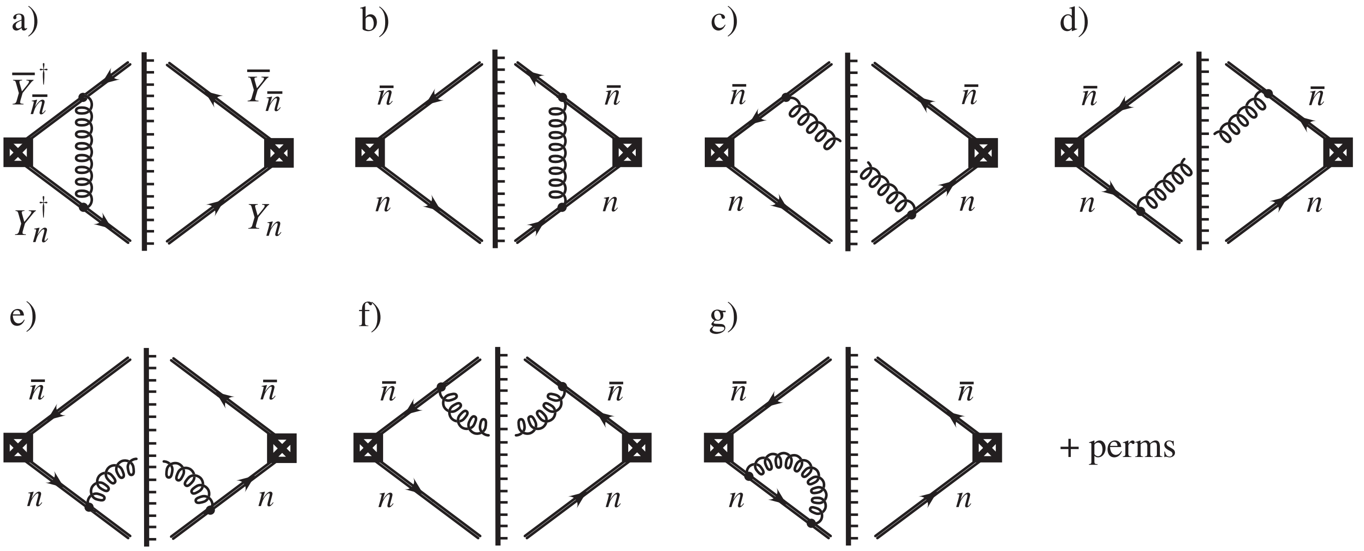

FIG. 7. Graphs for the hemisphere soft function at one loop. In this figure the solid lines denote Y-Wilson lines, and the line with ticks is the final state cut.

$$S_{\rm part}^{\rm bare}(\ell^+,\ell^-) = \delta(\ell^+)\delta(\ell^-) + \frac{C_F\alpha_s}{\pi}\bigg\{-\frac{\delta(\ell^+)\delta(\ell^-)}{\epsilon^2} + \frac{\delta(\ell^-)}{\epsilon\kappa_2}\bigg[\frac{\kappa_2\theta(\ell^+)}{\ell^+}\bigg]_+ + \frac{\delta(\ell^+)}{\epsilon\kappa_2}\bigg[\frac{\kappa_2\theta(\ell^-)}{\ell^-}\bigg]_+ - \frac{\delta(\ell^+)\delta(\ell^-)}{\epsilon}\ln\bigg(\frac{\mu^2}{\kappa_2^2}\bigg) + G_S(\ell^+,\ell^-)\bigg\}, \tag{110}$$

where $G_S(\ell^+,\ell^-)$ contains the finite terms

$$G_S(\ell^+,\ell^-,\mu) = \frac{1}{2}\delta(\ell^+)\delta(\ell^-)\bigg[\frac{\pi^2}{6} - \ln^2\bigg(\frac{\mu^2}{\kappa_2^2}\bigg)\bigg] + \frac{\delta(\ell^-)}{\kappa_2}\ln\bigg(\frac{\mu^2}{\kappa_2^2}\bigg)\bigg[\frac{\kappa_2\theta(\ell^+)}{\ell^+}\bigg]_+ + \frac{\delta(\ell^+)}{\kappa_2}\ln\bigg(\frac{\mu^2}{\kappa_2^2}\bigg)\bigg[\frac{\kappa_2\theta(\ell^-)}{\ell^-}\bigg]_+ - \frac{2\delta(\ell^-)}{\kappa_2}\bigg[\frac{\theta(\ell^+)\ln(\ell^+/\kappa_2)}{\ell^+/\kappa_2}\bigg]_+ - \frac{2\delta(\ell^+)}{\kappa_2}\bigg[\frac{\theta(\ell^-)\ln(\ell^-/\kappa_2)}{\ell^-/\kappa_2}\bigg]_+. \tag{111}$$

The renormalization factor for the hemisphere soft function then reads

$$Z_s(\ell'^+ - \ell^+, \ell'^- - \ell^-) = \delta(\ell^+ - \ell'^+)\delta(\ell^- - \ell'^-) - \frac{C_F\alpha_s}{\pi}\bigg\{\frac{\delta(\ell^+ - \ell'^+)\delta(\ell^- - \ell'^-)}{\epsilon^2} - \frac{\delta(\ell^- - \ell'^-)}{\epsilon\mu} \times \bigg[\frac{\mu\theta(\ell^+ - \ell'^+)}{\ell^+ - \ell'^+}\bigg]_+ - \frac{\delta(\ell^+ - \ell'^+)}{\epsilon\mu}\bigg[\frac{\mu\theta(\ell^- - \ell'^-)}{\ell^- - \ell'^-}\bigg]_+\bigg\}, \tag{112}$$

while the renormalized soft function is

$$S_{\rm part}(\ell^+,\ell^-,\mu) = \delta(\ell^+)\delta(\ell^-) + \frac{C_F\alpha_s(\mu)}{\pi}G_S(\ell^+,\ell^-,\mu). \tag{113}$$

We caution once more that the soft function is in general dominated by nonperturbative effects, so the partonic and perturbative result in Eq. (113) can only be used in the framework of the soft-function model of Eq. (40) or in situations where an operator product expansion can be carried out. We also note that to $\mathcal{O}(\alpha_s)$ the renormalized partonic soft function can be factored in the form

$$S_{\rm part}(\ell^+,\ell^-,\mu) = S_{\rm part}(\ell^+,\mu)S_{\rm part}(\ell^-,\mu), \tag{114}$$

where the partonic soft function with one kinematic variable is

$$S_{\rm part}(\ell^\pm,\mu) = \delta(\ell^\pm) + \frac{C_F\alpha_s(\mu)}{\pi}\bigg\{\delta(\ell^\pm)\bigg[\frac{\pi^2}{24} - \frac{1}{4}\ln^2\bigg(\frac{\mu^2}{\kappa_2^2}\bigg)\bigg] + \frac{1}{\kappa_2}\ln\bigg(\frac{\mu^2}{\kappa_2^2}\bigg)\bigg[\frac{\kappa_2\theta(\ell^\pm)}{\ell^\pm}\bigg]_+ - \frac{2}{\kappa_2}\bigg[\frac{\theta(\ell^\pm)\ln(\ell^\pm/\kappa_2)}{\ell^\pm/\kappa_2}\bigg]_+\bigg\}. \tag{115}$$

The factored form in Eq. (114) was expected at $\mathcal{O}(\alpha_s)$

because the single gluon in the real graphs of Fig. 7 can make either ℓ^+ or ℓ^- nonzero but not both. Because there is in general more than one real parton in the real graphs at $\mathcal{O}(\alpha_s^2)$ and beyond, the factored form of $S_{\rm part}$ is not expected to hold in general, nor for the full nonperturbative soft function S.

From Z_s in Eq. (112) one obtains the anomalous dimension

$$\gamma_S(\ell^+,\ell^-) = \delta(\ell^-)\gamma_s(\ell^+) + \delta(\ell^+)\gamma_s(\ell^-),$$
$$\gamma_s(\ell^\pm) = \frac{2C_F\alpha_s}{\pi}\frac{1}{\mu}\left[\frac{\mu\theta(\ell^\pm)}{\ell^\pm}\right]_+. \tag{116}$$

As anticipated from the form of the consistency condition discussed in Sec. III A, it has a separable structure in the light-cone variables ℓ^+ and ℓ^-. This separation for $\gamma_S(\ell^+,\ell^-)$ holds to all orders in α_s as discussed in Sec. III C. Comparing this result to Eq. (60) we find $\Gamma_0^s = -4C_F$, $\gamma_0^s = 0$, and infer $\Gamma_1^s = -\Gamma_1^{\rm cusp}$ for the coefficients discussed in Sec. III D. The anomalous dimension of various soft functions in SCET were studied in Ref. [76], and, in particular, the one-loop anomalous dimension for the jet-energy soft function in $e^+e^- \to$ dijets was derived. This anomalous dimension has the same form but opposite sign of the anomalous dimension in Eq. (116). However this is inconsequential, since there is no simple relation between the jet-energy soft function and the hemisphere soft function studied here. The hemisphere soft function's γ_s is the same as the anomalous dimension for the soft function for Drell-Yan in the end point region at one loop [43].

Before solving the soft-function anomalous dimension we pause to consider the number of active flavors in the RGE. For the SCET computation we can consider the five lightest flavors to be massless. In addition because we are above the scale of the top mass, we have a top-quark loop contribution to the soft-gluon induced β-function. The top-quark bubble couples to the soft gluon with a multipole expansion since the soft gluon has $p^2 \ll m^2$ for the purpose of power counting. Thus the bubble enters as an insertion of the vacuum polarization function at zero-momentum on the gluon line, $\Pi(0)$. The renormalization of this $\Pi(0)$ means that for $\mu > m$ there are a total of $n_f = 6$ flavors for the SCET running of the soft function. For $\mu < m$ the contributions from these top bubbles are integrated out, and the soft function runs with $n_f = 5$ flavors. Thus, in particular, we always have $n_f = 5$ for the soft function in bHQET.

To solve the RG equation in Eq. (57) we can use that the same equation holds for the evolution kernel $U_S(\ell^+,\ell^-,\mu,\mu_0)$ defined in Eq. (59) that describes the running of the soft function from μ_0 to the scale μ. Using the separable form $U_S(\ell^+,\ell^-,\mu,\mu_0) = U_s(\ell^+,\mu,\mu_0)U_s(\ell^-,\mu,\mu_0)$ of Eq. (73) one obtains from Eq. (116) the relations

$$\mu\frac{d}{d\mu}U_s(\ell^\pm,\mu,\mu_0) = \pm K U_s(\ell^\pm,\mu,\mu_0) + \int d\ell'^\pm \times \gamma_s(\ell^\pm - \ell'^\pm)U_s(\ell'^\pm,\mu,\mu_0). \tag{117}$$

Here K is a separation constant that can be set to zero.[7] The solution for $U_s(\ell^\pm,\mu,\mu_\Lambda)$ is given by Eq. (79),

$$U_s(\ell^\pm,\mu,\mu_0) = \frac{e^{K_2}(e^{\gamma_E})^{\omega_2}}{\mu_0\Gamma(-\omega_2)}\left[\frac{\mu_0^{1+\omega_2}\theta(\ell^\pm)}{(\ell^\pm)^{1+\omega_2}}\right]_+,$$
$$U_S(\ell^+,\ell^-,\mu,\mu_0) = \frac{e^{2K_2}(e^{\gamma_E})^{2\omega_2}}{\mu_0^2\Gamma(-\omega_2)^2}\left[\frac{\mu_0^{1+\omega_2}\theta(\ell^+)}{(\ell^+)^{1+\omega_2}}\right]_+ \times \left[\frac{\mu_0^{1+\omega_2}\theta(\ell^-)}{(\ell^-)^{1+\omega_2}}\right]_+, \tag{118}$$

where at NLL order we use Eq. (85) for $\omega_2 = \omega_2(\mu,\mu_0)$ and $K_2 = K_2(\mu,\mu_0)$ with the values of $\Gamma_{0,1}$ and γ_1 determined above. At LL order these are

$$\omega_2^{LL}(\mu,\mu_0) = \frac{4C_F}{\beta_0}\ln\left[\frac{\alpha_s(\mu)}{\alpha_s(\mu_0)}\right],$$
$$K_2^{LL}(\mu,\mu_0) = \frac{8\pi C_F}{\beta_0^2}\frac{(r - 1 - r\ln r)}{\alpha_s(\mu)}, \tag{119}$$

where $r = \frac{\alpha_s(\mu)}{\alpha_s(\mu_0)}$. The running generated by Eq. (118) falls in case (4). Note that for the jet function $\omega_1(\mu,\mu_0) > 0$ for $\mu > \mu_0$, while for the soft function $\omega_2(\mu,\mu_0) < 0$. Although this affects the behavior of the jet and the soft functions for large values of their arguments, the convolution of the jet functions and soft function always remains finite.

The factorization of the soft-function evolution, $U_S(\ell^+,\ell^-) = U_s(\ell^+)U_s(\ell^-)$, is necessary for the consistency equation in Eq. (75) to hold since it allows the cancellation to independently occur for the two jets, which are each convoluted with one of the variables of the soft function. Using Eqs. (95), (104), and (118) and the relations

$$\omega_0(\mu_0,\mu) = -\omega_1(\mu_0,\mu) = -\omega_2(\mu,\mu_0),$$
$$e^{(1/2)K_0(\mu_0,\mu)}e^{K_1(\mu_0,\mu)} = e^{K_2(\mu,\mu_0)}\left[\frac{\mu}{\mu_0}\right]^{-\omega_2(\mu,\mu_0)}, \tag{120}$$

we find

---

[7] Note that keeping the $\pm K$ term simply adds a multiplicative factor of $(\mu/\mu_\Lambda)^{\pm K}$ to the solutions, and cancels in the product $U_S(\ell^+,\ell^-) = U_s(\ell^+)U_s(\ell^-)$.

$$[U_{H_Q}(Q,\mu,\mu_0)]^{1/2}U_J(s,\mu_0,\mu)=\left[\frac{\mu}{Q}\right]^{-\omega_2}\left[\frac{\mu}{\mu_0}\right]^{-\omega_2}\frac{e^{K_2}(e^{\gamma_E})^{\omega_2}}{\mu^2\Gamma(-\omega_2)}\left[\left(\frac{\mu^2}{\mu_0 Q}\right)^{1+\omega_2}\frac{\theta(s)\mu_0^{1+\omega_2}}{(s/Q)^{1+\omega_2}}\right]_+=\frac{1}{Q}U_s\left(\frac{s}{Q},\mu,\mu_0\right). \quad (121)$$

This verifies that the SCET consistency condition is satisfied for the NLL-evolution factors. The consistency equations can also be verified at the level of the distributions in Eq. (71) using the results in Appendix D. Between $\mu_Q = 5m$ and $\mu_m = m = 172$ GeV we find $0 \le \omega_0(\mu_Q, \mu) \lesssim 0.14$ at LL and NLL order.

D. Universal running for a class of $M_{t,\bar{t}}$ definitions

In the last section we showed that the soft function for hemisphere invariant masses satisfies the SCET consistency condition. Since the renormalization is not sensitive to low energy properties of the soft function, like the mass definitions, one should expect that there is a broader class of soft functions that are consistent with the RGE in our factorization theorem. In this section we demonstrate this explicitly by working with a broader set of mass definitions and calculating the corresponding soft functions to $\mathcal{O}(\alpha_s)$.

In Ref. [2] it was shown that the form of the factorization theorem in Eqs. (3) and (38) is retained for any $M_{t,\bar{t}}$ prescription that assigns the hard top and antitop decay jets unambiguously to M_t and $M_{\bar{t}}$, and the momentum of every soft particle to *either* M_t or $M_{\bar{t}}$. The former condition ensures that the jet functions $B_\pm$, which are fully inclusive for the top decay products and collinear radiation, remain unchanged. The latter condition ensures that concentrating on $M_{t,\bar{t}}$ in the peak region automatically selects events in the dijet region for which the SCET-bHQET setup can be applied. The first condition is satisfied by reconstruction methods since for $Q \gg m$ the hard jets and collinear radiation are collimated to two back-to-back regions of the detector and the decay products only have a power-suppressed probability of $\mathcal{O}(m^2/Q^2)$ to show up in the opposite hemisphere [2]. The second condition restricts us to invariant mass definitions that incorporate all soft radiation. Examples include the hemisphere definition used in the last section, and particle recombination methods such as those based on k_T jet algorithms [77] with a $y_{\rm cut}$ parameter chosen so that all soft radiation is assigned to the hard jets from the top/antitop decay. Based on the equivalence of the top-down and the bottom-up approach to the renormalization of quantities in the factorization theorem, and the fact that the renormalization of the top-antitop production currents can only depend on virtual corrections, it was concluded in Ref. [2] that the renormalization properties of this class of soft functions does not depend on the prescription how the soft-gluon momenta are assigned to M_t and $M_{\bar{t}}$.

Let us now extend the soft-function analysis beyond hemisphere masses, by setting up a more general definition for M_t and $M_{\bar{t}}$ and hence for the matrix element defining $S(\ell^+, \ell^-, \mu)$. Since the contributions from the virtual graphs in Fig. 7(b), 7(b), and 7(g) are unaffected by phase space constraints it is sufficient to consider the graphs 7(c)–7(f) describing real soft-gluon final states. It is useful to write the gluon phase space integral given in Eq. (A12) in terms of the perp-momentum $q_\perp$ and the angular variable

$$x \equiv \tan\frac{\theta}{2} = e^{-\eta}, \quad (122)$$

where θ is the gluon angle and η the rapidity with respect to the top momentum direction. This gives

$$\begin{aligned}\tilde{\mu}^{2\epsilon}&\int\frac{d^{d-1}q}{(2\pi)^{d-1}}\frac{1}{q^+q^-(q^++q^-)}\\ &=\tilde{\mu}^{2\epsilon}\frac{(4\pi)^{-2+\epsilon}}{\Gamma(1-\epsilon)}\int_0^\infty dq^+\int_0^\infty dq^-(q^+q^-)^{-1-\epsilon}\\ &=2\tilde{\mu}^{2\epsilon}\frac{(4\pi)^{-2+\epsilon}}{\Gamma(1-\epsilon)}\int_0^\infty\frac{dx}{x}\int_0^\infty\frac{dq_\perp}{q_\perp^{1+2\epsilon}}, \quad (123)\end{aligned}$$

where $\tilde{\mu}$ is given in terms of μ in Eq. (A4). For the hemisphere invariant mass prescription gluons in hemisphere-a $(0 \le x \le 1)$ are assigned to the top, and gluons in hemisphere-b $(1 \le x \le \infty)$ are assigned to the antitop. One can interpret this hemisphere prescription as a crude jet algorithm. A prescription such as the k_T jet algorithm [77], that is tuned such that the total number of final jets equals the number of hard jets from the top and antitop quark decays, leads to a more complicated pattern since it depends on the particular momentum configuration of the hard jets.

However, the situation is simplified since at leading order in the power counting the hard jets are assigned unambiguously to the top and antitop invariant masses. Thus upon averaging over all hard jet configurations the jet algorithm assigns a soft gluon to either M_t or $M_{\bar{t}}$ according to a probability function, $f(x)$, that depends only on the angle θ. Expressing the phase space integration of the $\mathcal{O}(\alpha_s)$ soft function for this general jet algorithm we have

$$\begin{aligned}S_{6c}+S_{6d}&=2\frac{C_F\alpha_s}{\pi}\frac{(4\pi)^\epsilon\tilde{\mu}^{2\epsilon}}{\Gamma(1-\epsilon)}\int_0^\infty\frac{dx}{x}\int_0^\infty\frac{dq_\perp}{q_\perp^{1+2\epsilon}}\\ &\quad\times\{f(x)\delta(\ell^-)\delta(\ell^+-q_\perp x)+[1-f(x)]\\ &\quad\times\delta(\ell^--q_\perp/x)\delta(\ell^+)\}\\ &=2\frac{C_F\alpha_s}{\pi}\frac{(4\pi)^\epsilon\tilde{\mu}^{2\epsilon}}{\Gamma(1-\epsilon)}\left\{\frac{\delta(\ell^-)}{(\ell^+)^{1+2\epsilon}}\int_0^\infty\frac{dx}{x^{1-2\epsilon}}f(x)\right.\\ &\quad\left.+\frac{\delta(\ell^+)}{(\ell^-)^{1+2\epsilon}}\int_0^\infty\frac{dx}{x^{1+2\epsilon}}[1-f(x)]\right\}, \quad (124)\end{aligned}$$

where $f(x)$ gives the probability that a soft gluon with x is assigned to M_t. For the hemisphere masses we have $f(x) = \Theta(1-x)$. Consistency at leading order in the m/Q power counting requires that $f(0) = 1$ and $f(\infty) = 0$, i.e. the soft gluon is assigned with unit probability to M_t ($M_{\bar{t}}$) if it is radiated in exactly the top (antitop) momentum direction.

Using the identity of Eq. (109) and the scaling variable κ_2 from the previous subsection it is then straightforward to determine the bare soft function:

$$\begin{aligned} S^{\rm bare}(\ell^+,\ell^-) &= \delta(\ell^+)\delta(\ell^-) \\ &\quad + \frac{C_F\alpha_s}{\pi}\bigg\{-\frac{\delta(\ell^+)\delta(\ell^-)}{\epsilon^2} \\ &\quad + \frac{\delta(\ell^-)}{\epsilon\mu}\bigg[\frac{\mu\theta(\ell^+)}{\ell^+}\bigg]_+ + \frac{\delta(\ell^+)}{\epsilon\mu}\bigg[\frac{\mu\theta(\ell^-)}{\ell^-}\bigg]_+ \\ &\quad + \tilde{G}_S(\ell^+,\ell^-)\bigg\}, \end{aligned} \tag{125}$$

where it is the finite terms that depend on the arbitrary probability function $f(x)$

$$\begin{aligned} \tilde{G}_S(\ell^+,\ell^-) &= \frac{1}{2}\delta(\ell^+)\delta(\ell^-)\bigg[\frac{\pi^2}{6} - 8f_1\bigg] \\ &\quad + 2f_0\frac{\delta(\ell^-)}{\mu}\bigg[\frac{\mu\theta(\ell^+)}{\ell^+}\bigg]_+ \\ &\quad - 2f_0\frac{\delta(\ell^+)}{\mu}\bigg[\frac{\mu\theta(\ell^-)}{\ell^-}\bigg]_+ \\ &\quad - \frac{2\delta(\ell^-)}{\mu}\bigg[\frac{\theta(\ell^+)\ln(\ell^+/\mu)}{\ell^+/\mu}\bigg]_+ \\ &\quad - \frac{2\delta(\ell^+)}{\mu}\bigg[\frac{\theta(\ell^-)\ln(\ell^-/\mu)}{\ell^-/\mu}\bigg]_+, \end{aligned} \tag{126}$$

and

$$f_n \equiv \int_0^\infty dx\bigg(\frac{\ln^n x}{x}\bigg)_+ f(x). \tag{127}$$

For the hemisphere masses $f_n = 0$ for any n, and $\tilde{G}_S(\ell^+,\ell^-)$ reduces to $G_S(\ell^+,\ell^-)$ in Eq. (111). For a more general prescription for the soft-gluon assignments that is symmetric under the exchange of top and antitop, i.e. has $f(x) = 1 - f(1/x)$, then one still has $f_0 = 0$, while f_1 is in general nonvanishing.

The result in Eq. (125) demonstrates that the UV divergences and the RG evolution of the soft function are not affected by the phase space constraints imposed on the soft gluons, whereas the UV-finite contributions depend on them. This demonstrates to $\mathcal{O}(\alpha_s)$ that the form of the factorization theorem in Eqs. (3) and (38) is retained for the class of invariant mass definitions described above, and that different mass prescriptions only affect the form of the soft function, but not its renormalization scale dependence.

V. HQET RESULTS

To describe scales below the top mass we need to integrate out m by switching from SCET to bHQET. Here we describe the bHQET analogs of the matching, running, and matrix-element results given in the previous section on SCET.

A. bHQET current matching and running

In this section we determine the matching and the running of the $t\bar{t}$ current in bHQET at $\mathcal{O}(\alpha_s)$. For this we need to consider the one-loop graphs in Fig. 8. For convenience, the relevant bHQET Feynman rules have been collected in Appendix B, as are the results for the individual graphs. We use dimensional regularization for UV divergences and off-shell momenta to regulate the IR divergences. For the top and antitop quark momenta we take $p^\mu = mv_+^\mu + r_+^\mu$ and $\bar{p}^\mu = mv_-^\mu + r_-^\mu$, respectively, and then let $p^2 - m^2 = 2mv_+\cdot r_+ = \Delta^2$, and $\bar{p}^2 - m^2 = 2mv_-\cdot r_- = \Delta^2$, with $\Delta \neq 0$.

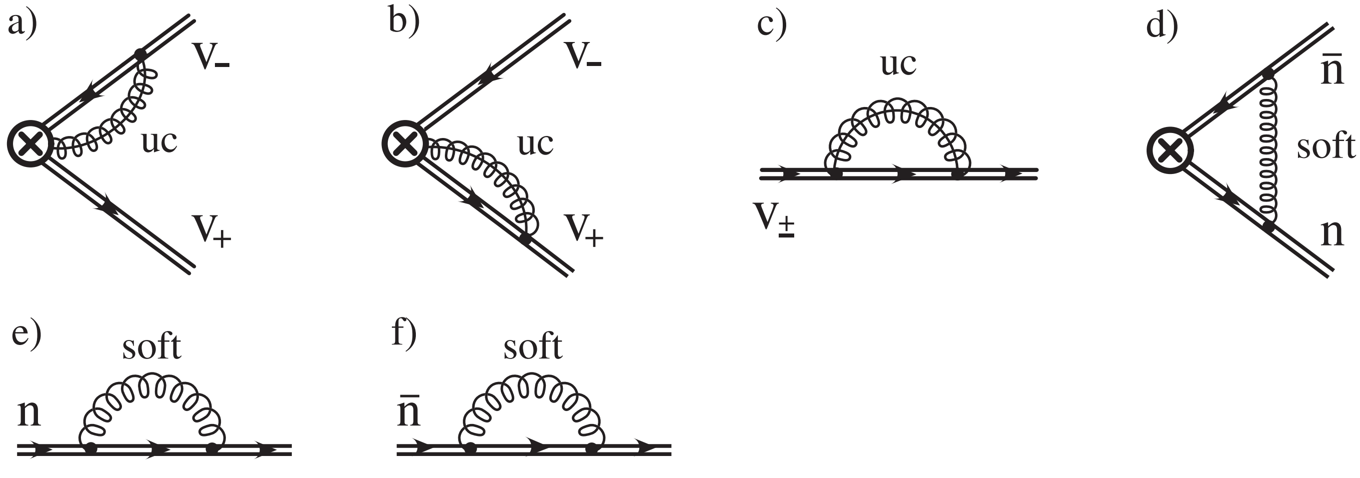

FIG. 8. Nonzero one-loop vertex and wave function corrections in boosted HQET. Graphs (a), (b), and (c) involve heavy quark fields $h_{v_\pm}$, while graphs (d), (e), and (f) only involve the Wilson lines $Y_n^\dagger$ and $Y_{\bar{n}}$.

The sum of the three vertex contributions, the wave function contribution and the residue is $V_{7a} + V_{7b} + V_{7c} + \Gamma_i^\mu(Z_h - 1) + \Gamma_i^\mu(R_h - 1)$ and gives the bare amplitude

$$\langle p, \bar{p}|\mathcal{J}_i^\mu|0\rangle_{\mathrm{bHQET}} = \bar{h}_{v_+}\gamma_\perp^\mu h_{v_-}\bigg[1 + \frac{\alpha_s C_F}{4\pi}\bigg(\frac{2}{\epsilon}\ln\frac{m^2}{-Q^2} + \frac{2}{\epsilon} - \ln^2\frac{\mu^2 Q^2}{-\Delta^4} + 4\ln^2\frac{m\mu}{-\Delta^2} + 4\ln\frac{m\mu}{-\Delta^2} + 4 + \frac{\pi^2}{3}\bigg)\bigg], \tag{128}$$

where $Q^2 = Q^2 + i0$ and $\Delta^2 = \Delta^2 + i0$. The UV divergences in the bHQET current are subtracted by the counterterm for the Wilson coefficient

$$Z_{C_m} = 1 - \frac{\alpha_s C_F}{4\pi}\bigg[\frac{2}{\epsilon}\ln\frac{m^2}{-Q^2} + \frac{2}{\epsilon}\bigg], \tag{129}$$

giving the renormalized bHQET amplitude

$$\langle p, \bar{p}|Z_{C_m}\mathcal{J}_i^\mu|0\rangle_{\mathrm{bHQET}} = \bar{h}_{v_+}\gamma_\perp^\mu h_{v_-}\bigg[1 + \frac{\alpha_s C_F}{4\pi}\bigg(-\ln^2\frac{\mu^2 Q^2}{-\Delta^4} + 4\ln^2\frac{m\mu}{-\Delta^2} + 4\ln\frac{m\mu}{-\Delta^2} + 4 + \frac{\pi^2}{3}\bigg)\bigg]. \tag{130}$$

As discussed already in Sec. III B the current renormalization constant contains a term $\ln(m/Q)/\epsilon$ with a coefficient that agrees with the coefficient of the $\ln(\mu/Q)/\epsilon$ term in the renormalization constant of the SCET current in Eq. (88). Also, the anomalous dimension of the bHQET current only exhibits single $1/\epsilon$ poles and thus sums only single $\ln(\mu)$ contributions. Although this running sums double logarithmic terms of the form $[\alpha_s(\mu)\ln(m/Q)\times\ln(\mu/m)]^k$, it formally belongs to class (1).

From the difference of the renormalized bHQET amplitude, $\langle p, \bar{p}|Z_{C_m}\mathcal{J}_i^\mu|0\rangle$, and the renormalized SCET amplitude in Eq. (89), we obtain the bHQET current matching conditions at the scale μ_m:

$$C_m(m, \mu_m) = 1 + \frac{\alpha_s C_F}{4\pi}\bigg(\ln^2\frac{\mu_m^2}{m^2} + \ln\frac{\mu_m^2}{m^2} + 4 + \frac{\pi^2}{6}\bigg). \tag{131}$$

The matching coefficient $H_m(m, \mu_m) = |C_m(m, \mu_m)|^2$ that appears in the factorization theorem reads

$$H_m(m, \mu_m) = 1 + \frac{\alpha_s C_F}{2\pi}\bigg(\ln^2\frac{\mu_m^2}{m^2} + \ln\frac{\mu_m^2}{m^2} + 4 + \frac{\pi^2}{6}\bigg). \tag{132}$$

This matching result only depends on the parameter m, and at the scale $\mu_m \sim m$ there are no large logarithms in $H_m(m, \mu_m)$.

The anomalous dimension is obtained from Z_{C_m} using Eq. (68) and gives

$$\begin{aligned}\gamma_{C_m}(\mu) &= -Z_{C_m}^{-1}(\mu)\mu\frac{d}{d\mu}Z_{C_m}(\mu)\\ &= \frac{\alpha_s C_F}{\pi}\bigg[\ln\frac{-Q^2 - i0}{m^2} - 1\bigg],\\ \gamma_{H_m}(\mu) &= \gamma_{C_m}(\mu) + \gamma_{C_m}(\mu)^* = \frac{\alpha_s C_F}{4\pi}\bigg[8\ln\frac{Q^2}{m^2} - 8\bigg].\end{aligned} \tag{133}$$

Comparing this result to Eq. (64) we find $\Gamma_0^{H_m} = -8C_F$, $\gamma_0^{H_m} = -8C_F$, and infer $\Gamma_1^{H_m} = -2\Gamma_1^{\mathrm{cusp}}$ for the coefficients discussed in Sec. III D. The solution for the evolution factor for the mass scale coefficient H_m in Eq. (65) reads

$$U_{H_m}\bigg(\frac{Q}{m}, \mu_m, \mu\bigg) = e^{K_{00}}\bigg(\frac{m^2}{Q^2}\bigg)^{\omega_0}, \tag{134}$$

where at NLL order we use the expressions in Eq. (85) for $\omega_0 = \omega_0(\mu, \mu_m)$ and $K_{00} = K_{00}(\mu, \mu_m)$. At LL order we have

$$K_{00}^{LL}(\mu, \mu_m) = \frac{4C_F}{\beta_0}\ln\bigg[\frac{\alpha_s(\mu)}{\alpha_s(\mu_m)}\bigg], \tag{135}$$

and just as in the running with U_{H_Q}, $\omega_0^{LL}(\mu, \mu_m) = (4C_F/\beta_0)\ln[\alpha_s(\mu)/\alpha_s(\mu_m)]$. Note that as in the case of the SCET current the RGE solution for the current Wilson coefficient $C_m(m, \mu_Q, \mu)$ contains an extra phase factor,

$$C_m(m, \mu) = \sqrt{H_m(m, \mu)}\bigg[\frac{\alpha_s(\mu)}{\alpha_s(\mu_m)}\bigg]^{2\pi i(C_F/\beta_0)}, \tag{136}$$

that does not, however, appear in the cross section.[8] The origin of this phase, and the reason it drops out of the final predictions, is the same as for the SCET current Wilson coefficient discussed in Sec. IV A.

B. bHQET jet functions matching and running

In this subsection we determine the bHQET jet functions $B_\pm$ defined in Eq. (21) at $\mathcal{O}(\alpha_s)$, obtaining one-loop corrections to the Breit-Wigner distributions in Eq. (28). The results for B_+ and B_- are identical by charge conjugation. We also determine the bHQET jet-function renormaliza-

---

[8] It is interesting to note that the result in Eq. (136) can be obtained from running the heavy-to-heavy current in HQET [8], analytically continuing to the production region [78], and expanding in m/Q.

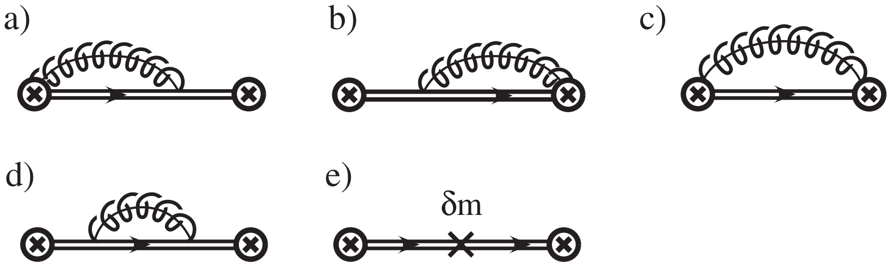

FIG. 9. bHQET graphs for the top-quark jet function.

tion factor Z_B, the jet anomalous dimension γ_B, the NLL-evolution kernel U_B, and finally $B_\pm$ at NLL order. By comparing the jet functions in bHQET and SCET we confirm that their IR divergences agree. Finally, we demonstrate that the matching condition for $H_m(m, \mu_Q)$, already obtained for the top-antitop currents in Eq. (132), is reproduced by jet-function matching. This is a reflection of the statement that we have the same soft function in the SCET and bHQET theories to $\mathcal{O}(\alpha_s)$. Thus the soft-function computations in Secs. IV C and IV D apply equally well for bHQET.

For the computation it is convenient to use the formulae from Sec. II B which determine the jet function for the unstable top quark from the results for a stable bHQET theory. To do this one can either use the relation equation (33) which shifts the invariant mass variable into the complex plane, or use the convolution relation in Eq. (37).

The bHQET jet functions are given by the imaginary part of the vacuum matrix elements $\mathcal{B}_\pm$ defined in Eq. (22). At tree level they are just given by the HQET propagator,

$$\mathcal{B}_\pm(\hat s, \Gamma_t = 0) = -\frac{1}{\pi m}\frac{1}{\hat s + i0}. \tag{137}$$

At one loop the diagrams contributing to the vacuum matrix elements $\mathcal{B}_\pm$ are shown in Fig. 9. Results for individual graphs are given in the appendix. The sum of the one-loop graphs in an arbitrary mass scheme gives the bare expression

$$\begin{aligned}\mathcal{B}^{\rm bare}_\pm&(\hat s, \Gamma_t = 0, \mu, \delta m)\\ &= -\frac{1}{\pi m}\frac{1}{\hat s + i0}\bigg\{1 + \frac{\alpha_s C_F}{4\pi}\bigg[\frac{2}{\epsilon^2} + \frac{4}{\epsilon}\ln\Big(\frac{\mu}{-\hat s - i0}\Big)\\ &\quad + \frac{2}{\epsilon} + 4\ln^2\Big(\frac{\mu}{-\hat s - i0}\Big) + 4\ln\Big(\frac{\mu}{-\hat s - i0}\Big) + 4 + \frac{5\pi^2}{6}\bigg]\bigg\}\\ &\quad - \frac{1}{\pi m}\frac{2\delta m}{(\hat s + i0)^2}.\end{aligned} \tag{138}$$

In general the residual mass term $\delta m = m_{\rm pole} - m$ is nonzero and uniquely fixes the mass scheme m that is being employed in HQET. In an arbitrary mass scheme we have $\mathcal{B}_\pm(\hat s, \Gamma_t, \mu, \delta m) = \mathcal{B}_\pm(\hat s - 2\delta m, \Gamma_t, \mu)$. Here δm is computed as a perturbative series in α_s. We have $\delta m \sim \alpha_s$ at lowest order, and the δm in the HQET Lagrangian, Eq. (30), should be included as a perturbative insertion. This yields the term shown in Eq. (138).

The result in Eq. (138) can be compared to the computation of initial state radiation from a heavy color scalar resonance produced by the collision of massless colored and neutral scalars in Ref. [15]. At leading order in the $1/m$ expansion the HQET gluon interactions are spin independent and so only affect the normalization. Furthermore to $\mathcal{O}(\alpha_s)$ there is no difference between initial state and final state radiation, the signs of the $i0$ terms in the eikonal propagators do not modify the result. In our calculation the analog of the initial state colored scalar in Ref. [15] is given by the final state Wilson lines in our jet function. Thus, we expect that the linear combination of terms in Eq. (138) in the pole-mass scheme where $\delta m = 0$ should be the same as obtained in the scalar computation [15], and we have checked that this is indeed the case. The scalar analysis of Ref. [15] was based on diagrams rather than deriving a factorization theorem, so an operator analogous to the one we give for our jet-functions was not given.

The renormalization of the vacuum matrix element and the jet functions for the stable or the unstable bHQET theory is equivalent, so one can obtain the renormalization factor for the jet functions from Eq. (138). The result reads

$$\begin{aligned}Z_{B_\pm}(\hat s - \hat s') = \delta(\hat s - \hat s') &+ \frac{\alpha_s C_F}{4\pi}\bigg\{\delta(\hat s - \hat s')\bigg[\frac{2}{\epsilon^2} + \frac{2}{\epsilon}\bigg]\\ &- \frac{4}{\mu\epsilon}\bigg[\frac{\mu\,\theta(\hat s - \hat s')}{\hat s - \hat s'}\bigg]_+\bigg\}.\end{aligned} \tag{139}$$

Note that the bHQET jet-functions Z-factor and their anomalous dimension do not depend on the mass scheme that is being used. The renormalized vacuum matrix element has the form

$$\begin{aligned}\mathcal{B}_\pm(\hat s, 0, \mu, \delta m) = -\frac{1}{\pi m}\frac{1}{\hat s + i0}\bigg\{1 &+ \frac{\alpha_s C_F}{4\pi}\\ &\times\bigg[4\ln^2\Big(\frac{\mu}{-\hat s - i0}\Big) + 4\ln\Big(\frac{\mu}{-\hat s - i0}\Big)\\ &+ 4 + \frac{5\pi^2}{6}\bigg]\bigg\} - \frac{1}{\pi m}\frac{2\delta m}{(\hat s + i0)^2}.\end{aligned} \tag{140}$$

The renormalized jet function accounting for the large top-quark width is then either given by taking the imaginary part of Eq. (140) upon the shift $\hat{s} \to \hat{s} + i\Gamma_t$ (see Eq. (33)) or by applying the convolutions formula of Eq. (37). The result is

$$\begin{aligned} B_\pm(\hat{s}, \Gamma_t, \mu, \delta m) = {}& \frac{1}{\pi m}\frac{\Gamma}{\hat{s}^2+\Gamma^2}\bigg\{1 + \frac{\alpha_s C_F}{4\pi}\bigg[\ln^2\bigg(\frac{\mu^2}{\hat{s}^2+\Gamma^2}\bigg) \\ & + 2\ln\bigg(\frac{\mu^2}{\hat{s}^2+\Gamma^2}\bigg) - 4\arctan^2\bigg(\frac{\Gamma}{\hat{s}}\bigg) \\ & + 4\frac{\hat{s}}{\Gamma}\arctan\bigg(\frac{\Gamma}{\hat{s}}\bigg)\bigg\{\ln\bigg(\frac{\mu^2}{\hat{s}^2+\Gamma^2}\bigg) + 1\bigg\} \\ & + 4 + \frac{5\pi^2}{6}\bigg]\bigg\} + \frac{1}{\pi m}\frac{(4\hat{s}\Gamma_t)\delta m}{(\hat{s}^2+\Gamma^2)^2}, \end{aligned} \tag{141}$$

where the arctan is evaluated in the third quadrant. In practice, in the presence of the width it is more convenient to not bother evaluating the imaginary part explicitly, and simply use $B_\pm(\hat{s}, \Gamma_t, \mu, \delta m) = \mathrm{Im}[\mathcal{B}_\pm(\hat{s} + i\Gamma_t, 0, \mu, \delta m)]$. We also present the stable bHQET jet function,

$$\begin{aligned} B_\pm^{\Gamma=0}(\hat{s}, \mu, \delta m) &= \mathrm{Im}[\mathcal{B}_\pm(\hat{s}, 0, \mu, \delta m)] \\ &= \delta(s) + \frac{\alpha_s(\mu)C_F}{\pi}\bigg\{\frac{2}{m\kappa_3}\bigg[\frac{\theta(z)\ln(z)}{z}\bigg]_+ \\ &\quad - \frac{1}{m\kappa_3}\bigg[1 + 2\ln\bigg(\frac{\mu}{\kappa_3}\bigg)\bigg]\bigg[\frac{\theta(z)}{z}\bigg]_+ \\ &\quad + \delta(s)\bigg[\ln^2\bigg(\frac{\mu}{\kappa_3}\bigg) + \ln\bigg(\frac{\mu}{\kappa_3}\bigg) + 1 - \frac{\pi^2}{8}\bigg]\bigg\} \\ &\quad - \frac{2\delta m}{m}\delta'(\hat{s}), \end{aligned} \tag{142}$$

where we have allowed for an arbitrary rescaling of $\hat{s} = \kappa_3 z$. A convenient choice for the parameter κ_3 is $\kappa_3 = \mu$, where $z = \hat{s}/\mu$ and

$$\begin{aligned} B_\pm^{\Gamma=0}(\hat{s}, \mu, \delta m) = {}& \delta(s) + \frac{\alpha_s(\mu)C_F}{\pi}\bigg\{\frac{2}{m\mu}\bigg[\frac{\theta(z)\ln(z)}{z}\bigg]_+ \\ & - \frac{1}{m\mu}\bigg[\frac{\theta(z)}{z}\bigg]_+ + \delta(s)\bigg[1 - \frac{\pi^2}{8}\bigg]\bigg\} \\ & - \frac{2\delta m}{m}\delta'(\hat{s}). \end{aligned} \tag{143}$$

To determine H_m we can match the bHQET and SCET jet-function results for $\hat{s} = s/m \ll m$. For the matching the top width only takes the role of an IR parameter, and the computation is most conveniently carried out for stable top quarks. If the same mass scheme is used in SCET and bHQET, then the δm terms are the same, and cancel in the matching. The jet-function matching coefficient can be obtained from matching either the jet functions or the vacuum matrix elements. For this computation it is convenient to pick $\kappa_3 = m$ in Eq. (142) and subtract it from Eq. (107) to obtain

$$T_\pm(m, \mu_m) = 1 + \frac{\alpha_s C_F}{4\pi}\bigg(\ln^2\frac{m^2}{\mu_m^2} - \ln\frac{m^2}{\mu_m^2} + 4 + \frac{\pi^2}{6}\bigg). \tag{144}$$

Using $H_m = T_+T_-$ this agrees with Eq. (132) at $\mathcal{O}(\alpha_s)$.

The anomalous dimension for the jet function is determined from Eq. (139) and reads

$$\gamma_B(\hat{s} - \hat{s}', \mu) = -\frac{\alpha_s C_F}{4\pi}\bigg\{\frac{8}{\mu}\bigg[\frac{\mu\theta(\hat{s} - \hat{s}')}{\hat{s} - \hat{s}'}\bigg]_+ - 4\delta(\hat{s} - \hat{s}')\bigg\}. \tag{145}$$

Comparing this result to Eq. (60) we find $\Gamma_0^B = 4C_F$, $\gamma_0^B = 4C_F$, and infer $\Gamma_1^B = \Gamma_1^{\mathrm{cusp}}$ for the coefficients discussed in Sec. III D. The solution for the evolution equation (69) is

$$U_B(\hat{s} - \hat{s}', \mu, \mu_0) = \frac{e^{K_3}(e^{\gamma_E})^{\omega_1}}{\mu_0\Gamma(-\omega_1)}\bigg[\frac{\mu_0^{1+\omega_1}\theta(\hat{s} - \hat{s}')}{(\hat{s} - \hat{s}')^{1+\omega_1}}\bigg]_+, \tag{146}$$

where $\omega_1 = \omega_1(\mu, \mu_0)$ and $K_3 = K_3(\mu, \mu_0)$ are determined at NLL order using Eq. (85) with $r = \alpha_s(\mu)/\alpha_s(\mu_0)$. At LL order

$$\begin{aligned} \omega_1^{LL}(\mu, \mu_0) &= -\frac{4C_F}{\beta_0}\ln\bigg[\frac{\alpha_s(\mu)}{\alpha_s(\mu_0)}\bigg], \\ K_3^{LL}(\mu, \mu_0) &= -\frac{8\pi C_F}{\beta_0^2}\frac{(r - 1 - r\ln r)}{\alpha_s(\mu)}. \end{aligned} \tag{147}$$

In comparing the bHQET jet function to that in SCET, the most striking difference is that the dimension-1 variable $\hat{s}$ is natural for bHQET, whereas in SCET we had a natural dimension-2 variable s. This causes a difference in the convolution of jet and soft functions in the two theories. However, comparing the bHQET jet-function evolution function U_B to the SCET evolution function U_J in Eq. (104), one notices that we have the same function ω_1 of α_s. This is crucial to the fact that the spectrum remains protected against large logs as we evolve below $\mu = m$, with the consistency condition in SCET carrying over to a consistency condition in bHQET, as given in Eq. (43). In particular, the relation between the soft and jet evolution factors, $\omega_1(\mu_0, \mu) = \omega_2(\mu, \mu_0)$, remains valid. This ensures that the plus functions in U_J and U_s match, which was the key to verifying the SCET consistency condition in Eq. (121) above. The fact that ω_1 is unchanged can be viewed as a compensation between a change in the *geometry* of the physical color flow governing the QCD dynamics in the two theories, and a change in the *dimension* j of the natural jet-function variable used in Appendix D. Here the geometric properties are encoded in the cusp-anomalous dimensions Γ_0, which are determined by the cusp angle between Wilson lines in the jet functions. In particular the equality of the ω_1's follows from the equality of the ratio

$$\frac{(\Gamma_0)^{J_{n,\bar{n}}}}{(j)^{J_{n,\bar{n}}}} = \frac{(\Gamma_0)^{B_\pm}}{(j)^{B_\pm}}, \tag{148}$$

as can be seen from Eq. (85) in Sec. III D. To verify the bHQET consistency condition to NLL order we use $\omega_0(\mu_0, \mu) = -\omega_1(\mu_0, \mu) = -\omega_2(\mu, \mu_0)$ and note that

$$\begin{aligned} e^{(1/2)K_{00}(\mu_0,\mu)} e^{K_3(\mu_0,\mu)} &= e^{(1/2)K_0(\mu_0,\mu)} e^{K_1(\mu_0,\mu)} \\ &= e^{K_2(\mu,\mu_0)} \left[\frac{\mu}{\mu_0}\right]^{-\omega_2(\mu,\mu_0)}, \end{aligned} \tag{149}$$

which allows us to obtain the desired result in Eq. (43):

$$\left[U_{H_m}\left(\frac{Q}{m}, \mu, \mu_0\right)\right]^{1/2} U_B(\hat{s}, \mu_0, \mu) = \left[\frac{m}{Q}\right]^{-\omega_2} \left[\frac{\mu}{\mu_0}\right]^{-\omega_2} \frac{e^{K_2}(e^{\gamma_E})^{\omega_2}}{\mu\Gamma(-\omega_2)} \left[\left(\frac{\mu m}{\mu_0 Q}\right)^{1+\omega_2} \frac{\theta(\hat{s})\mu_0^{1+\omega_2}}{(m\hat{s}/Q)^{1+\omega_2}}\right]_+ = \frac{m}{Q} U_s\left(\frac{m\hat{s}}{Q}, \mu, \mu_0\right). \tag{150}$$

Again the equivalent bHQET consistency equation with distributions given in Eq. (77) can be verified using results from Appendix D. Between $\mu_m = 172$ GeV and $\mu = 1$ GeV we find $0 \leq \omega_0(\mu_Q, \mu) \leq 0.93$ at LL and NLL order. Interestingly, from the factorization theorem in Eqs. (44) and (45) the U_B factor is run down from μ_Γ to μ_Λ giving $\omega_1 < 0$, or the U_S factor is run up from μ_Λ to μ_Γ giving $\omega_2 < 0$. Thus we never exceed the bound $\omega < 1$ on the range of validity of the convolution resummation formulas given in Appendix D.

Finally, we quote analytic results for the resummed bHQET jet functions. Using the tree-level result for bHQET propagator $\mathcal{B}_\pm$ in Eq. (137) as the initial condition at the scale μ_0 it is straightforward to determine the LL result at the scale μ by carrying out the integral in Eq. (69). For the vacuum matrix element this gives

$$\mathcal{B}_\pm^{\rm LL}(\hat{s}, 0, \mu) = \frac{1}{m\pi} e^{K_3^{\rm LL}(\mu,\mu_0)} (\mu_0 e^{\gamma_E})^{\omega_1^{\rm LL}} \frac{\Gamma(1+\omega_1^{\rm LL})}{(-\hat{s}-i0)^{1+\omega_1^{\rm LL}}}, \tag{151}$$

where $\omega_1^{\rm LL}$ and $K_3^{\rm LL}$ are given in Eq. (147). Now using Eq. (37) gives the LL bHQET jet function at the scale μ with the tree-level jet function $B_\pm^{\rm tree} = \Gamma/[\pi m(\hat{s}^2 + \Gamma^2)]$ as the input at the scale μ_0:

$$\begin{aligned} B_\pm^{\rm LL}(\hat{s}, \Gamma_t, \mu) = {}& \frac{1}{m\pi} e^{K_3^{\rm LL}(\mu,\mu_0)} (\mu_0 e^{\gamma_E})^{\omega_1^{\rm LL}} \Gamma(1+\omega_1^{\rm LL}) \\ & \times \mathrm{Im}\left[\frac{1}{(-\hat{s}-i\Gamma)^{1+\omega_1^{\rm LL}}}\right]. \end{aligned} \tag{152}$$

Since the boundary condition is specified at tree level the result does not involve δm. When the $\mathcal{O}(\alpha_s)$ jet function is taken as the initial condition at the scale μ_0 with NLL evolution we obtain what we will call the NLL result for the jet function. This result depends on δm and is given by the analytic result

$$\begin{aligned} B_\pm^{\rm NLL}(\hat{s}, \Gamma_t, \mu, \delta m) = {}& \frac{1}{m\pi} e^{K_3(\mu,\mu_0)} (\mu_0 e^{\gamma_E})^{\omega_1} \Gamma(1+\omega_1)\, \mathrm{Im}\left[\frac{1}{(-\hat{s}-i\Gamma_t)^{1+\omega_1}}\right. \\ & \times \left\{1 + \frac{C_F \alpha_s(\mu_0)}{\pi}\left[1 + \frac{\pi^2}{24} - \ln\left(\frac{-\hat{s}-i\Gamma_t}{\mu_0}\right) + H(\omega_1) + \left\{\ln\left(\frac{-\hat{s}-i\Gamma_t}{\mu_0}\right) - H(\omega_1)\right\}^2 + \Psi'(1+\omega_1)\right]\right. \\ & \left.\left. - \frac{2(1+\omega_1)\delta m}{(-\hat{s}-i\Gamma_t)}\right\}\right], \end{aligned} \tag{153}$$

where $H(\omega)$ is the harmonic number function and $\Psi'(z) = d/dz[\Gamma'(z)/\Gamma(z)]$ is the derivative of the polygamma function. This result was derived using Eq. (E6) from Appendix E.

VI. SHORT-DISTANCE TOP JET MASS AND THE TOP-QUARK POLE

One of the main goals of the factorization based analysis of $d^2\sigma/dM_t^2 dM_{\bar{t}}^2$ is to facilitate a high precision determination of the top-quark mass. To do so it is important to explore the correspondence between the top mass and the peak in the predicted $M_{t,\bar{t}}$ invariant mass distribution. Equation (3) shows that the peak position of the top/antitop invariant mass distributions is affected by perturbative corrections in the jet functions $B_\pm(\hat{s}, \Gamma_t, \mu)$ and by nonperturbative effects through the convolution with the soft function $S(\ell^+, \ell^-, \mu)$. In this section we analyze effects of the jet functions on the peak, and define a consistent short-distance jet-mass scheme. The jet functions were computed to $\mathcal{O}(\alpha_s)$ in Sec. V. In these computations the top-quark width Γ_t provides an IR cutoff that makes the perturbative determination of the jet-function line shape valid for any value of $\hat{s}$, and, in particular, for the peak region.

As can be seen from Fig. 9, the Feynman diagrams for $B_\pm$ contain the HQET heavy quark self-energy. The other diagrams are generated from the Wilson lines $W_{n,\bar{n}}$ and render the jet functions gauge invariant. In the pole-mass scheme the HQET self-energy develops a linear sensitivity to IR momenta [79]. This is caused by an ambiguity of $\mathcal{O}(\Lambda_{\rm QCD})$ in the pole mass, and hence in the pole scheme invariant mass variable $\hat{s}$, i.e. in $\hat{s} = (M^2_{t,\bar{t}} - m^2_{\rm pole})/m_{\rm pole}$ where $\delta m = 0$. In perturbation theory this ambiguity is associated to an asymptotic behavior $\propto \mu\alpha_s(\mu)^{n+1}\beta_0^n n!$, where μ is the scale employed for $\alpha_s(\mu)$ in the jet function. The situation is similar to the total cross section for top-antitop pair production in the threshold region $Q \sim 2m$ [80,81], where using the pole mass the peak position cannot be rendered stable in perturbation theory. Thus, in the pole-mass scheme $B_\pm$ is expected to have a poorly behaved perturbation series, indicating that it is not the pole mass that can be accurately determined from the measured invariant mass distribution. This is because the pole mass is defined order by order to be a zero of the inverse heavy quark two-point function that is not observable physically. This feature is demonstrated for the one-loop jet function below and will be analyzed at higher orders in Refs. [82,83].

It is therefore advantageous and even mandatory to switch to a short-distance mass scheme that can stabilize the location of the jet-function peak location in perturbation theory. In a general mass scheme the location of the peak is determined by

$$\frac{dB_\pm(\hat{s}, \Gamma_t, \mu, \delta m)}{d\hat{s}}\bigg|_{\hat{s}=\hat{s}_{\rm peak}} = \frac{dB_\pm(\hat{s} - 2\delta m, \Gamma_t, \mu)}{d\hat{s}}\bigg|_{\hat{s}=\hat{s}_{\rm peak}} = 0. \tag{154}$$

At tree level $\delta m = 0$ and the jet functions are equal to the Breit-Wigner functions in Eq. (28), so $\hat{s}_{\rm peak} = 0$. At $\mathcal{O}(\alpha_s)$ the jet functions $B_\pm$ are given by the expressions in Eqs. (141) and solving the condition in Eq. (154) perturbatively gives

$$\hat{s}^{\rm NLO}_{\rm peak} = 2\delta m - \frac{\alpha_s(\mu)C_F}{2}\Gamma_t\bigg[\ln\bigg(\frac{\mu}{\Gamma_t}\bigg) + \frac{3}{2}\bigg]. \tag{155}$$

As explained in Ref. [2] a viable short-distance mass scheme must have $\delta m \sim \alpha_s\Gamma_t$ in order not to violate the power counting. This condition rules out the $\overline{\rm MS}$-mass as a candidate since $\delta m_{\overline{\rm MS}} \sim \alpha_s m_t$, and hence violates the factorization theorem for the cross section. A viable short-distance mass scheme can be defined using Eq. (154) by demanding that $\hat{s}_{\rm peak} = 0$ order by order in perturbation theory. Equation (155) then determines δm at NLO. This mass satisfies the power counting criteria, but unfortunately has a complicated dependence on the renormalization scale. This can be seen from the peak position at LL order, derived using Eq. (152) for $B_\pm$ with the initial condition of a Breit-Wigner at the scale μ_0. This LL result is independent of the mass scheme and we find

$$\hat{s}^{\rm LL}_{\rm peak}(\mu, \mu_0) = -\Gamma_t \cot\bigg[\frac{\pi}{2 + \omega_1^{LL}(\mu, \mu_0)}\bigg] = \Gamma_t\frac{C_F\pi}{\beta_0}\ln\bigg[\frac{\alpha_s(\mu)}{\alpha_s(\mu_0)}\bigg] + \ldots \tag{156}$$

Here $\omega_1^{LL}(\mu, \mu_0)$ is given in Eq. (147), and in the second equality we show the leading term for small ω_1. Because of the nonlinear nature of the cotangent in Eq. (156) a mass scheme determined by $\hat{s}_{\rm peak} = 0$ is not transitive, in the sense that $\hat{s}^{\rm LL}_{\rm peak}(\mu, \mu_1) + \hat{s}^{\rm LL}_{\rm peak}(\mu_1, \mu_2) \neq \hat{s}^{\rm LL}_{\rm peak}(\mu, \mu_2)$. This makes a mass definition based on the peak position awkward to use. The problem occurs because the peak position is a local feature of $B_\pm(\hat{s}, \mu)$, while $B_\pm$ requires a convolution for its RG evolution as seen in Eq. (69). If Eq. (154) is evolved to a different renormalization scale then it involves an integral over $B_\pm$. In perturbation theory this nonlocal feature is reflected by terms $[C_F\alpha_s \ln]^k$ in the expansion of $\hat{s}^{\rm LL}_{\rm peak}$.

To define a transitive short-distance jet mass $m_J(\mu)$, which is still closely related to the peak position, we will use the first moment of $B_+^{\Gamma=0}$. To LL order it suffices to simply use an upper cutoff L_m on this moment, and define δm_J so that this moment vanishes

$$0 = \int_{-\infty}^{L_m} d\hat{s}\, \hat{s}\, B_+^{\Gamma=0}(\hat{s}, \mu, \delta m_J) = \int_{-\infty}^{L_m} d\hat{s}\, \hat{s}\, B_+^{\Gamma=0}(\hat{s} - 2\delta m_J, \mu). \tag{157}$$

Different choices of L_m define different schemes for the mass. As indicated, it also suffices to define the mass scheme using the zero-width jet function. As shown in Eq. (37) the jet function for a nonzero width is related to the stable one by

$$B_\pm(\hat{s}, \delta m_J, \Gamma_t, \mu) = \int_{-\infty}^{\hat{s}} d\hat{s}' B_\pm^{\Gamma=0}(\hat{s} - \hat{s}', \delta m_J, \mu) \times \frac{\Gamma_t}{\pi(\hat{s}'^2 + \Gamma_t^2)}, \tag{158}$$

and so the stability of $B_\pm^{\Gamma=0}$ is directly transferred to $B_\pm$. We can solve Eq. (157) keeping only the linear term in δm_J, thus

$$0 = \int_{-\infty}^{L_m} d\hat{s}\, \hat{s} B_+^{\Gamma=0}(\hat{s}, 0) - 2\delta m_J \int_{-\infty}^{L_m} d\hat{s}\, \hat{s} \frac{d}{d\hat{s}} B_+^{\Gamma=0}(\hat{s}, 0) + \mathcal{O}[(\delta m_J)^2\alpha_s]. \tag{159}$$

Integrating by parts gives the solution

$$\delta m_J = -\frac{\int_{-\infty}^{L_m} d\hat{s}\, \hat{s} B_+^{\Gamma=0}(\hat{s}, 0)}{[2\int_{-\infty}^{L_m} d\hat{s} B_+^{\Gamma=0}(\hat{s}, 0)] - 2L_m B_+^{\Gamma=0}(L_m, 0)}. \tag{160}$$

Expanding in α_s to one-loop order we find

$$\delta m_J(\mu) = L_m \frac{\alpha_s(\mu) C_F}{\pi}\left[\ln\left(\frac{\mu}{L_m}\right) + \frac{3}{2}\right]. \tag{161}$$

To obtain a consistent mass for top-quark jets we must choose the scheme parameter $L_m \sim \Gamma_t$. We will adopt $L_m = 1$ GeV for our analysis since then δm_J gives $|\hat{s}_{\text{peak}}^{\text{NLO}}| \leq 32$ MeV for $\mu = 2$–10 GeV and hence a very stable peak position. The use of a first moment to define a mass scheme as in Eq. (157) has been applied in a similar way earlier to inclusive B-decays [84], to give what is known as the shape-function scheme. However the shape-function scheme does result in a different mass definition from the jet scheme defined here.

To achieve cancellation of the $O(\Lambda_{\text{QCD}})$ renormalon ambiguity in the jet-mass scheme the scale μ in $\delta m_J(\mu)$ needs to agree with the renormalization scale used for the strong coupling in the corrections of the jet function. Using Eq. (31) the one-loop relation between the pole and jet mass m_J is:

$$m_J^{\text{NLO}}(\mu) = m_{\text{pole}} - L_m \frac{\alpha_s(\mu) C_F}{\pi}\left[\ln\left(\frac{\mu}{L_m}\right) + \frac{3}{2}\right]. \tag{162}$$

We can also derive a LL result for the running jet mass. From the NLO δm_J in Eq. (161) we can compute a renormalization-group equation for $m_J(\mu)$, whose LL solution is

$$m_J^{\text{LL}}(\mu) = m_J(\mu_0) + L_m \frac{2C_F}{\beta_0} \ln\left[\frac{\alpha_s(\mu)}{\alpha_s(\mu_0)}\right]. \tag{163}$$

To verify that this result contains all the leading logs, we use Eq. (152) to determine $(B_+^{\Gamma=0})^{\text{LL}}$ with evolution from μ_1 up to μ. Using the LL jet function in Eq. (152) and solving Eq. (157) without expanding in δm, we find a solution $\delta m(\mu, \mu_1)$ that contains all leading logs between μ_1 and μ. Then by taking $m_J^{\text{LL}}(\mu) = m_J(\mu_0) + \delta m(\mu_0, \mu_1) - \delta m(\mu, \mu_1)$ we obtain a μ_1-independent result that reproduces exactly Eq. (163). The jet mass $m_J(\mu)$ has a standard series of $[\beta_0 \alpha_s \ln]^k$ terms, and as far as its RG evolution is concerned behaves very similar to an $\overline{\text{MS}}$ mass. In particular, this jet mass is transitive at LL order.

Results for the jet functions are shown in Fig. 10(a), where we have plotted $mB_\pm(\hat{s}, \Gamma_t, \mu)$ at tree level (long dashed black line), and at NLO in the pole-mass scheme (green short dashed lines) and in the jet-mass scheme (solid red lines). We take $\Gamma_t = 1.43$ GeV. At $\mathcal{O}(\alpha_s)$ we use Eq. (141), taking $\delta m = 0$ in the pole-mass scheme, and taking δm_J with $L_m = 1$ GeV from Eq. (161) in the jet-mass scheme. For each $\mathcal{O}(\alpha_s)$ prediction we show two curves, one for $\mu = 2$ GeV (lower lines) and one for $\mu = 5$ GeV (upper lines). While the resonance peak is located at $\hat{s} = 0$ at tree level, in the pole scheme at one loop it is

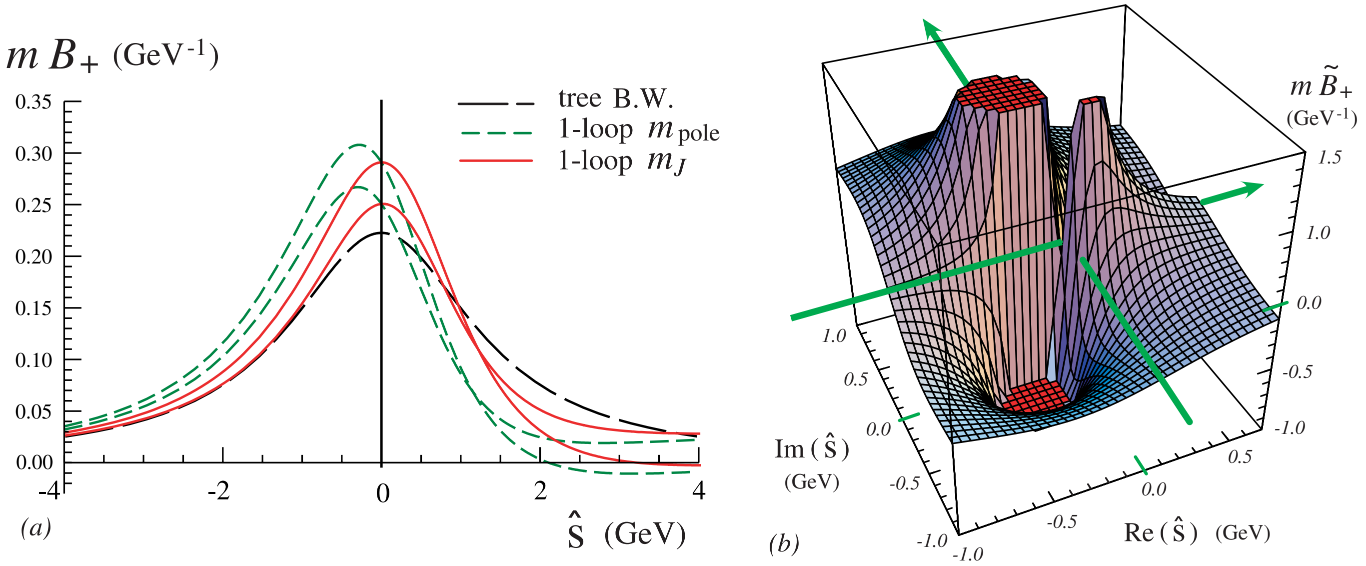

FIG. 10 (color online). (a) The bHQET jet function $mB_\pm(\hat{s}, \Gamma_t, \mu)$ as a function of $\hat{s}$ at tree level (black long dashed line) and $\mathcal{O}(\alpha_s)$ in the pole-mass scheme (green short dashed lines) and the jet-mass scheme (red solid lines) for $\mu = 2$ (lower lines) and 5 GeV (upper lines). (b) Imaginary part of $m\mathcal{B}_\pm(\hat{s}, 0, \mu)$ in the pole-mass scheme for $\mu = 2$ GeV plotted in the complex $\hat{s}$-plane. Solid green lines indicate $\text{Re}(\hat{s}) = 0$ or $\text{Im}(\hat{s}) = 0$ in the plane where $\text{Im}(m\mathcal{B}_\pm) = 0$. For the strong coupling we used $\alpha_s = 0.262$, 0.203 for $\mu = 2$, 5 GeV.

shifted by 250 MeV towards smaller masses. In the jet-mass scheme the peak is located at $\hat{s} \simeq 0$.

One may wonder how the shift of the jet function in the pole scheme arises, given that $\mathcal{B}_\pm$ in Eq. (141) obviously has a pole at $\hat{s} + i\Gamma_t = 0$. The reason this pole is not visible in Fig. 10(a) is that the jet function is modified by powers of $\ln[(-\hat{s} - i\Gamma_t)/\mu]$. To illustrate this, consider the inverse of the stable vacuum matrix element in the pole-mass scheme

$$[\tilde{\mathcal{B}}_\pm(\hat{s}, 0, \mu)]^{-1} \equiv -\pi m(\hat{s} + i0)\bigg\{1 - \frac{\alpha_s C_F}{4\pi} \times \bigg[4\ln^2\bigg(\frac{\mu}{-\hat{s} - i0}\bigg) + 4\ln\bigg(\frac{\mu}{-\hat{s} - i0}\bigg) + 4 + \frac{5\pi^2}{6}\bigg]\bigg\}. \tag{164}$$

In Fig. 10(b) the imaginary part of $m\tilde{\mathcal{B}}_\pm$ is plotted in the complex $\hat{s}$-plane for $\mu = 2$ GeV. The small positive peak visible at $\hat{s} = 0$ is related to the zero of $(\tilde{\mathcal{B}}_\pm)^{-1}$ at $\hat{s} = 0$ and thus connected to the pole mass. However, it is inaccessible physically when the finite top-quark width is accounted for, i.e. when $\tilde{\mathcal{B}}_\pm$ is evaluated in the upper complex half-plane at $\hat{s} + i\Gamma_t$. Moreover, it has the wrong causality structure since it leads to a small negative dip when approached from the upper complex half-plane. The vacuum matrix element is instead dominated by the pole on the negative real axis, that is visible as a large peak to the left of the smaller peak at $\hat{s} = 0$. Conceptually this means that the physical pole of the jet function is not located at the pole mass and that the pole mass *per se* is not tied to a physical object. This conclusion is fully compatible with previous work on the consequences of the pole-mass renormalon problem [85–90], from which it is already known that the pole mass is an unphysical parameter. The analysis of the calculable $\mathcal{B}_\pm$ provides a surprisingly direct view on the mechanism of how this is achieved within perturbation theory.

From Eq. (162) we see that the jet mass, $m_J(\mu)$, depends on the renormalization scale. This dependence arises because the jet functions have an anomalous dimension. In the jet-mass scheme we induce additional μ-dependence in the cross section that appears through $m_J(\mu)$ in the variable $\hat{s}$ and through the $\delta m_J(\mu)$ term in $B_\pm$. This μ-dependence cancels out order by order in perturbation theory. To implement the jet mass in the factorization theorem we proceed as follows. We take the value of the jet mass at a certain reference scale, $m_J(\mu_0)$, as the parameter one would like to determine from fitting the cross section to data. In terms of this parameter one determines the jet mass $m_J(\mu_\Gamma)$ via Eq. (163) where $\mu = \mu_\Gamma$ is the scale for which the jet function is to be determined perturbatively. In the jet functions $B_\pm(\hat{s}, \Gamma_t, \mu_\Gamma, \delta m)$ we then use $\delta m = \delta m_J(\mu_\Gamma)$ and the invariant mass variables $\hat{s}_{t,\bar{t}}$ are determined via

$$\hat{s}_{t,\bar{t}} = \frac{M_{t,\bar{t}}^2 - m_J^2(\mu_\Gamma)}{m_J(\mu_\Gamma)}. \tag{165}$$

We emphasize again that it is crucial that the renormalization scale in δm and in the explicit logs in the jet functions $B_\pm$ agree, in order to ensure the cancellation of the $\mathcal{O}(\Lambda_{\rm QCD})$ renormalon ambiguity. This is because asymptotically (for large order n) the terms causing the poorly behaved perturbative behavior in the pole-mass scheme at $\mathcal{O}(\alpha_s^{n+1})$ are proportional to $[\mu_\Gamma \alpha_s^{n+1}(\mu_\Gamma)\beta_0^n n!]$, and only cancel if the same renormalization scale is used.

Relation to other mass schemes.—It is useful to relate the jet mass to the top $\overline{\rm MS}$ mass, $\bar{m}_t(\mu)$. This facilitates using a top-mass measurement from jets in other computations, such as electroweak precision tests. Typically one is interested in $\bar{m}_t(\bar{m}_t)$, since the renormalization-group evolution in $\overline{\rm MS}$ makes sense only above the mass of the particle. To relate the two mass schemes we take the measured $m_J(\mu_0)$ and use the solution to the jet-mass RGE equation in Eq. (163) to run it up to, lets say, $\mu = \bar{m}_t$, obtaining $m_J(\bar{m}_t)$. Now we use the relations to the scale independent pole mass at $\mu = \bar{m}_t$:

$$\bar{c}(\bar{m}_t)\bar{m}_t(\bar{m}_t) = m_t^{\rm pole} = m_J(\bar{m}_t) + c_J(\bar{m}_t, L_m)L_m, \tag{166}$$

where $\bar{c}(\mu) = 1 + C_F\alpha_s(\mu)/\pi(1 + \frac{3}{2}\ln(\mu/\bar{m}_t)) + \ldots$ and c_J is given to one loop by Eq. (162). Recall that the choice of L_m determines a scheme, so $m_J(\mu)$ also depends on this parameter. Expanding the relation in Eq. (166) to one-loop order we obtain a translation of the jet mass to the $\overline{\rm MS}$ scheme that is free of the $\mathcal{O}(\Lambda_{\rm QCD})$ renormalon contained in the pole mass:

$$\bar{m}_t(\bar{m}_t) = m_J(\bar{m}_t) - \frac{\alpha_s(\bar{m}_t)C_F}{\pi}m_J(\bar{m}_t) + \frac{\alpha_s(\bar{m}_t)C_F}{\pi}L_m\bigg[\ln\bigg(\frac{\bar{m}_t}{L_m}\bigg) + \frac{3}{2}\bigg]. \tag{167}$$

Note again that it is essential to strictly expand the series on the RHS of Eq. (167) and to use the strong coupling constant at the *same* scale everywhere to ensure the proper cancellation of the $\mathcal{O}(\Lambda_{\rm QCD})$ renormalon ambiguity [91]. We also note that $\bar{c}(m_t)$ is known to three-loop order [92–94], while $c_J(m_t, \Gamma_t)$ is only known to one-loop at this time. Because of the small size of Γ_t the one-loop contribution of $c_J(m_t, \Gamma_t)$ causes only a shift of about $\simeq 250$ MeV in the determination of the $\overline{\rm MS}$ mass $\bar{m}_t(m_t)$. Thus this correction may in many cases not be of critical concern when converting a top-mass determination from jets into an $\overline{\rm MS}$ mass at one-loop order. However, we emphasize that mistaking a jet-mass measurement as a pole-mass value beyond the one-loop order can lead to a significant error in precision quantities that have a strong dependence on the top-quark $\overline{\rm MS}$ mass and which have been computed to high order in QCD. This is due to the $\mathcal{O}(\Lambda_{\rm QCD})$ renormalon inherent to the pole-mass definition. It is therefore an important task to determine the higher order contributions in the jet-mass definition of Eq. (162).

Another important class of top-quark masses are the so-called threshold masses [80] which can be determined to very high precision from a threshold scan of the total top pair production cross section at a future e^+e^- linear collider. Based on theoretical predictions at the next-to-next-to leading level in QCD [80,81,95] and through dedicated experimental studies it is expected that a threshold top mass such as the 1S-mass [59,89,90] can be determined with theoretical and experimental uncertainties at the level of 100 MeV [96,97]. It is therefore useful to relate the jet mass to the top 1S mass. To establish this relation one should note that the 1S mass is defined in the framework of nonrelativistic QCD and incorporates effects which are associated to soft $\sim m_t\alpha_s$ and ultrasoft $\sim m_t\alpha_s^2$ scales. Since ultrasoft effects are not responsible for the nonrelativistic binding effects that define the 1S mass definition and since the $\mathcal{O}(\Lambda_{\rm QCD})$ renormalon contribution in the 1S-pole-mass relation are associated to the soft scale [86], the relation between the jet and 1S mass has to be determined for the soft scale $\mu_S \sim m_t\alpha_s$. To obtain the relation one can use an approach similar to the one described above and first evolve the jet mass to μ_S using Eq. (163). It is then straightforward to relate the jet mass to the 1S mass using the known results for the 1S-pole-mass relation, see e.g. Refs. [81,98,99] for three-loop results (see also Refs. [100,101]) accounting also for summation of large logarithmic terms and Refs. [102,103] for four-loop fixed order expressions. At one-loop order the relation reads

$$m_t^{\rm 1S} = m_J(\mu_S) - \frac{\alpha_s(\mu_S)C_F}{8}[\alpha_s(\mu_S)C_F m_J(\mu_S)] + \frac{\alpha_s(\mu_S)C_F}{\pi}L_m\bigg[\ln\bigg(\frac{\mu_S}{L_m}\bigg) + \frac{3}{2}\bigg]. \tag{168}$$

Note that the same principles for treating the perturbative series discussed above for the $\overline{\rm MS}$-jet-mass relation have to be applied here to ensure the proper cancellation of the $\mathcal{O}(\Lambda_{\rm QCD})$ renormalon contributions. In addition it is necessary to treat the terms in the perturbative series in the 1S-pole-mass relation in the so-called Upsilon expansion, where terms that are of order α_s^{n+1} are formally treated of order α_s^n [89,90]. This is because the physical scale that governs this series is the inverse Bohr radius $C_F m_t\alpha_s$ (which is the analog of L_m in Eq. (162)). Note that the one-loop corrections from the jet-pole-mass relation have a larger numerical impact in the one-loop relation of Eq. (168) than in Eq. (167) because the 1S-pole-mass corrections are an order of magnitude smaller than the corrections in the $\overline{\rm MS}$-pole-mass relation. We will give a more detailed discussion on the higher order structure of Eqs. (167) and (168) in Ref. [82].

VII. SOFT-FUNCTION MODELS WITH PERTURBATIVE CORRECTIONS

The soft function at a scale $\mu \sim \mu_\Lambda$ is written as

$$S(\ell^+,\ell^-,\mu) = \int_{-\infty}^{+\infty} d\tilde\ell^+ \int_{-\infty}^{+\infty} d\tilde\ell^- \times S_{\rm part}(\ell^+ - \tilde\ell^+, \ell^- - \tilde\ell^-, \mu, \delta) \times S_{\rm mod}(\tilde\ell^+, \tilde\ell^-). \tag{169}$$

This combines the partonic perturbative result for the soft function $S^{\rm part}$ (given in Eqs. (113) for the hemisphere prescription), with a model hadronic function $S^{\rm mod}$ satisfying the moment constraints in Eq. (41). As explained in Ref. [30], this form encodes the features we require for an appropriate soft function S for our analysis. In particular it works equally well for the peak region where the soft function is nonperturbative, and for the tail region where the soft function is perturbatively calculable at leading power. S in Eq. (169) has μ dependence consistent with its anomalous dimension and the $\overline{\rm MS}$ scheme. And finally it should be totally free from the $\mathcal{O}(\Lambda_{\rm QCD})$ soft-function renormalon ambiguity identified in Ref. [30], which is also known to appear in event shapes for massless jets [104].

For the analyses in this work we will use the exponential model $f_{\rm exp}$ of Ref. [22], with the addition of a gap parameter Δ, so that

$$S_{\rm mod}(\ell^+,\ell^-,\Delta) = f_{\rm exp}(\ell^+ - \Delta, \ell^- - \Delta),$$
$$f_{\rm exp}(\ell^+,\ell^-) = \theta(\ell^+)\theta(\ell^-)\frac{\mathcal{N}(a,b)}{\Lambda^2}\bigg(\frac{\ell^+\ell^-}{\Lambda^2}\bigg)^{a-1} \times \exp\bigg(\frac{-(\ell^+)^2 - (\ell^-)^2 - 2b\ell^+\ell^-}{\Lambda^2}\bigg). \tag{170}$$

Here the normalization constant $\mathcal{N}(a,b)$ is defined so that $\int d\ell^+ d\ell^- S(\ell^+,\ell^-) = 1$. The parameter $\Lambda \sim \Lambda_{\rm QCD}$ sets the width of the hadronic function and hence the scale for $\ell^\pm$ and the soft radiation. The dimensionless parameter a controls how fast the function vanishes at the origin, and the dimensionless parameter $b > -1$ controls the correlation of energy flow into the two hemispheres. Any $b \neq 0$ implies cross talk between the two hemispheres.[9] The gap parameter Δ enforces $\ell^\pm \geq \Delta$ and encodes the minimal hadronic energy deposit due to soft radiation.

As explained in Ref. [30], there is a renormalon in $S_{\rm part}(\ell^\pm - \tilde\ell^\pm)$ that corresponds to an $\mathcal{O}(\Lambda_{\rm QCD})$ ambiguity in the partonic threshold where $\ell^\pm - \tilde\ell^\pm = 0$, and a corresponding ambiguity in the nonperturbative gap parame-

---

[9] In Ref. [22] the values $a = 2$ and $b = -0.4$ were obtained from a fit to LEP data. The analysis used a different scheme for including perturbative corrections in the soft function than the one advocated here.

ter Δ. It can be removed by shifting to a renormalon free gap parameter $\bar{\Delta}$, using $= \Delta = \bar{\Delta}(\mu) + \delta(\mu)$,

$$\begin{aligned} S(\ell^+, \ell^-, \mu) &= \int_{-\infty}^{+\infty} d\tilde{\ell}^+ \int_{-\infty}^{+\infty} d\tilde{\ell}^- \\ &\quad \times S_{\rm part}(\ell^+ - \tilde{\ell}^+, \ell^- - \tilde{\ell}^-, \mu) \\ &\quad \times f_{\rm exp}(\tilde{\ell}^+ - \Delta, \tilde{\ell}^- - \Delta) \\ &= \int_{-\infty}^{+\infty} d\tilde{\ell}^+ \int_{-\infty}^{+\infty} d\tilde{\ell}^- \\ &\quad \times S_{\rm part}(\ell^+ - \tilde{\ell}^+ - \delta, \ell^- - \tilde{\ell}^- - \delta, \mu) \\ &\quad \times f_{\rm exp}(\tilde{\ell}^+ - \bar{\Delta}, \tilde{\ell}^- - \bar{\Delta}). \end{aligned} \tag{171}$$

Here $\delta = \sum_{i=1}^{\infty} \delta_i$ is a perturbative series with $\delta_i \sim \mathcal{O}(\alpha_s^i)$ that defines the scheme for $\bar{\Delta}$. Expanding $S_{\rm part}(\ell^\pm - \tilde{\ell}^\pm - \delta)$ in perturbation theory the δ_i's remove the renormalon ambiguity from $S_{\rm part}$ order by order. Up to $\mathcal{O}(\alpha_s)$ this gives

$$\begin{aligned} S_{\rm part}(\ell^+, \ell^-, \mu, \delta_i) &= S^0_{\rm part}(\ell^+, \ell^-) \\ &\quad + \bigg[S^1_{\rm part}(\ell^+, \ell^-, \mu) \\ &\quad - \delta_1 \Big(\frac{d}{d\ell^+} + \frac{d}{d\ell^-} \Big) S^0_{\rm part}(\ell^+, \ell^-) \bigg], \end{aligned} \tag{172}$$

where defining $\mathcal{L}^1(\ell) = 1/\mu[\theta(\ell)\ln(\ell/\mu)/(\ell/\mu)]_+$ we have

$$\begin{aligned} S^0_{\rm part}(\ell^+, \ell^-) &= \delta(\ell^+)\delta(\ell^-), \\ S^1_{\rm part}(\ell^+, \ell^-, \mu) &= \delta(\ell^+) S^1_{\rm part}(\ell^-, \mu) + \delta(\ell^-) S^1_{\rm part}(\ell^+, \mu), \\ S^1_{\rm part}(\ell, \mu) &= \frac{C_F \alpha_s(\mu)}{\pi} \Big[\frac{\pi^2}{24} \delta(\ell) - 2\mathcal{L}^1(\ell) \Big]. \end{aligned} \tag{173}$$

A renormalon free scheme for the gap $\bar{\Delta}$ can be defined [30] using a first moment of the soft function with upper cutoff L_Δ, similar to the jet mass in Eq. (157). This definition can be written

$$0 = \int_{-\infty}^{L_\Delta} d\ell^+ \int_{-\infty}^{L_\Delta} d\ell^- \ell^+ S_{\rm part}(\ell^+ - \delta, \ell^- - \delta, \mu), \tag{174}$$

and at $\mathcal{O}(\alpha_s)$ gives [30]

$$\delta_1 = -2L_\Delta \frac{C_F \alpha_s(\mu)}{\pi} \Big[\ln\Big(\frac{\mu}{L_\Delta} \Big) + 1 \Big]. \tag{175}$$

Because $\Delta = \bar{\Delta}(\mu) + \delta(\mu)$ is RG invariant, this gives an anomalous dimension equation

$$\mu \frac{d}{d\mu} \bar{\Delta}(\mu) = 2L_\Delta \frac{C_F \alpha_s(\mu)}{\pi}, \tag{176}$$

with a LL solution

$$\bar{\Delta}(\mu) = \bar{\Delta}(\mu_0) - L_\Delta \frac{4C_F}{\beta_0} \ln\Big[\frac{\alpha_s(\mu)}{\alpha_s(\mu_0)} \Big]. \tag{177}$$

Using Eq. (172) in (170) and integrating by parts we obtain a suitable soft function for our NLL analysis

$$\begin{aligned} S(\ell^+, \ell^-, \mu) &= S_{\rm mod}(\ell^+, \ell^-, \bar{\Delta}) - \delta_1 \Big(\frac{d}{d\ell^+} + \frac{d}{d\ell^-} \Big) \\ &\quad \times S_{\rm mod}(\ell^+, \ell^-, \bar{\Delta}) + \int_{-\infty}^{+\infty} d\tilde{\ell}^+ \int_{-\infty}^{+\infty} d\tilde{\ell}^- \\ &\quad \times S^1_{\rm part}(\ell^+ - \tilde{\ell}^+, \ell^- - \tilde{\ell}^-, \mu) \\ &\quad \times S_{\rm mod}(\tilde{\ell}^+, \tilde{\ell}^-, \bar{\Delta}) \\ &\equiv \int_{-\infty}^{+\infty} d\tilde{\ell}^+ \int_{-\infty}^{+\infty} d\tilde{\ell}^- \\ &\quad \times \tilde{S}_{\rm part}(\ell^+ - \tilde{\ell}^+, \mu, \delta_1) \\ &\quad \times \tilde{S}_{\rm part}(\ell^- - \tilde{\ell}^-, \mu, \delta_1) S_{\rm mod}(\tilde{\ell}^+, \tilde{\ell}^-, \bar{\Delta}), \end{aligned} \tag{178}$$

where the modified one-dimensional partonic soft function is

$$\tilde{S}_{\rm part}(\ell, \mu, \delta_1) = \delta(\ell) - \delta_1(\mu)\delta'(\ell) + S^1_{\rm part}(\ell, \mu). \tag{179}$$

With Eq. (170) the result in Eq. (178) involves logarithmic terms $\ln(\ell^\pm/\mu)$ and $\ln(\Lambda/\mu)$, that arise from the convolution of the partonic plus functions with the smooth hadronic functions. In the peak region there is a possible tension between the convergence of the perturbative series in $\alpha_s(\mu)$ for $S_{\rm part}$ and the size of the $\ln(\Lambda/\mu)$ terms. In Ref. [30] the log series in the soft function was analyzed and it was concluded that for scales $\mu \simeq 1$ GeV in the peak region this tension is not an issue. In the tail region the cross section is dominated by $\ell^\pm \sim \hat{s}m/Q$. Thus $\ell^\pm$ grows, and it becomes necessary to increase μ so that $\mu \sim \hat{s}m/Q$ to avoid large logs from the $\ln(\ell^\pm/\mu)$ terms.

To demonstrate the importance of the renormalon subtraction we show $S(\ell^+, \ell^-, \mu)$ in Fig. 11, plotted with $\ell = \ell^+ = \ell^-$ for $\Lambda = 0.55$ GeV and three sets of the remaining parameters $(a, b, L_\Delta/\Lambda) = (2.5, -0.4, 0.8)$, $(3.5, -0.2, 0.7)$, and $(2.5, -0.8, 0.8)$, respectively. The tree-level soft function is $S = S_{\rm mod}$ in Eq. (170) where we take $\bar{\Delta} = 100$ MeV, and is shown by the black solid lines. The three dashed blue lines denote the $\mathcal{O}(\alpha_s)$ soft function obtained from Eqs. (178) without the renormalon subtraction ($\delta_1 = 0$), and for $\mu = 0.8, 0.9, 1.0$ GeV. The three light solid red lines denote the $\mathcal{O}(\alpha_s)$ soft function obtained from Eqs. (178) with a renormalon free gap using δ_1 from

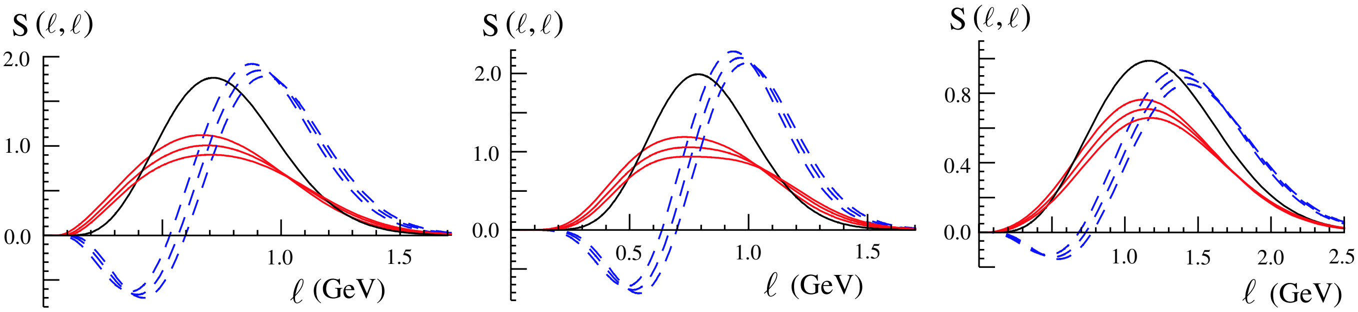

FIG. 11 (color online). Soft-function models based on Eq. (178) with the hadronic model function $S^{\rm mod}$ given in Eq. (170) for $\Lambda = 0.55$ GeV, $\bar\Delta(\mu = 1\ {\rm GeV}) = 0.1$ GeV, and $(a, b) = (2.5, -0.4)$ (left panel), $(3.5, -0.2)$ (middle panel), and $(a, b) = (2.5, -0.8)$ (right panel). The curves are tree level (black solid line), $\mathcal{O}(\alpha_s)$ with $\delta_1 = 0$ (blue dashed lines), and $\mathcal{O}(\alpha_s)$ with a renormalon free gap (red light solid lines). The blue and red curves are shown for $\mu = 0.8, 0.9, 1.0$ GeV, with the higher curves corresponding to lower values of the renormalization scale.

Eq. (175), and $\mu = 0.8, 0.9, 1.0$ GeV. For both the blue and red curves we use $\bar\Delta(\mu) = 60, 82, 100$ MeV for these three μ's, respectively, which corresponds to implementing the LL running from Eq. (177). Compared to the tree-level result, the blue dashed $\mathcal{O}(\alpha_s)$ curves show a significantly shifted location of their maximum and become negative for small values of ℓ. The red light solid curves show that the renormalon subtraction stabilizes the peak location and removes the negative dip. These features are generic for any choice of hadronic model parameters (a, b).

VIII. NUMERICAL ANALYSIS UP TO NEXT-TO-LEADING LOG ORDER

In Ref. [2] we carried out a numerical analysis of the top-invariant mass distribution concentrating on nonperturbative effects caused by the soft function and on the dependence of the invariant mass distributions on the parameters used for the soft-function model. The analysis was based on the tree-level results for the jet functions in Eq. (28), without summation of logarithms, and on the hemisphere soft function as given by the model of Ref. [22] which had been obtained from fits to event shapes in e^+e^- annihilation. The soft function caused a positive shift in the peak position of the invariant mass distribution, $M_{t,\bar t} > m_J$, where the shift is parametrically $\sim\Lambda_{\rm QCD}Q/m$, and it was demonstrated that the peak shift and peak width grow linearly with Q/m.

In this section we will extend the analysis to include radiative corrections and examine the perturbative convergence of predictions for the invariant mass distribution. This amounts to a full NLL analysis (i.e. one-loop matrix elements plus NLL summation of logarithms). Recall from Fig. 1 that there are four relevant scales for the log summation, $\mu_Q \simeq Q$, $\mu_m \simeq m$, $\mu_\Gamma \simeq \hat s + \Gamma_t + Q\Lambda/m_t$, and $\mu_\Lambda \gtrsim \Lambda_{\rm QCD} + m\Gamma_t/Q + \hat s m/Q$. For the peak region we use $\mu_\Lambda \simeq 1$ GeV. Our analysis is performed in several steps. After setting up the cross-section formula, we proceed in Sec. VIII A to consider the summation of large logs for the perturbative corrections, and analyze the scale and scheme dependence. We show that the summation of logs between $\mu_\Gamma \simeq \Gamma_t + Q\Lambda/m_t$ and $\mu_\Lambda \simeq 1$ GeV have a significant impact on stabilizing the cross section. Then in Sec. VIII B we convolute the perturbative corrections with the soft-function model and analyze the cross section in the peak region. In Sec. VIII C we analyze the cross section in the tail region, and plot combined peak and tail results. Finally in Sec. VIII D we use our results to determine the thrust distribution at NLL order.

For the numerical analysis it is convenient to write the invariant mass cross section in the top jet-mass scheme in terms of dimension one invariant mass variables

$$\frac{d^2\sigma}{dM_t dM_{\bar t}} = \frac{\sigma_0}{\Gamma_t^2} F\bigg(M_t, M_{\bar t}, m_J, \frac{Q}{m_J}\bigg), \qquad (180)$$

where the prefactor σ_0 is given in Eq. (7). Here m_J is the jet mass and the dimensionless function F is

$$\begin{aligned} F\bigg(M_t, M_{\bar t}, m_J, \frac{Q}{m_J}\bigg) &= \int_{-\infty}^{\infty} d\ell^+ d\ell^- {\rm P}\bigg(\hat s_t - \frac{Q\ell^+}{m_J}, \hat s_{\bar t} - \frac{Q\ell^-}{m_J}, \mu_\Lambda\bigg) S^{\rm mod}(\ell^+, \ell^-, \bar\Delta(\mu_\Lambda)) \\ &= \int_{-\infty}^{\infty} d\ell^+ d\ell^- {\rm P}\bigg(\hat s_t - \frac{Q\ell^+}{m_J} - \frac{Q\bar\Delta(\mu_\Lambda)}{m_J}, \hat s_{\bar t} - \frac{Q\ell^-}{m_J} - \frac{Q\bar\Delta(\mu_\Lambda)}{m_J}, \mu_\Lambda\bigg) S^{\rm mod}(\ell^+, \ell^-, 0), \end{aligned} \qquad (181)$$

with $S^{\rm mod}$ the hadronic model function given in Eq. (170). In the second line we shifted the integration variables to put all μ-dependent factors into P. In terms of M_t and $M_{\bar t}$ the invariant mass variables $\hat s_{t,\bar t}$ in Eq. (181) are

$$\hat{s}_{\,t} = \frac{M_t^2 - m_J^2}{m_J}, \qquad \hat{s}_{\bar{t}} = \frac{M_{\bar{t}}^2 - m_J^2}{m_J}. \tag{182}$$

All the perturbatively computable contributions in Eq. (181) are grouped into the dimensionless function

$$\begin{aligned} \mathrm{P}(\hat{s}_t, \hat{s}_{\bar{t}}, \mu_\Lambda) = {}& 4M_t M_{\bar{t}} \Gamma_t^2 H_Q(Q, \mu_Q) U_{H_Q}(Q, \mu_Q, \mu_m) H_m(m, \mu_m) U_{H_m}\Big(\frac{Q}{m_J}, \mu_m, \mu_\Lambda\Big) \\ & \times G_+\Big(\hat{s}_t, \frac{Q}{m_J}, \Gamma_t, \mu_\Lambda\Big) G_-\Big(\hat{s}_{\bar{t}}, \frac{Q}{m_J}, \Gamma_t, \mu_\Lambda\Big). \end{aligned} \tag{183}$$

P also depends on Q, m_J, and Γ_t, but for simplicity we have not shown this dependence in its arguments. For the hard coefficients we used Eqs. (55) and (65) to write them in terms of the one-loop matching coefficients $H_Q(Q, \mu_Q)$ and $H_m(m, \mu_m)$ in Eqs. (93) and (132) and the NLL-evolution factors U_{H_Q} and U_{H_m} given by Eq. (79). The functions $G_\pm$ in Eq. (183) contain perturbative corrections that modify the shape of the cross section. Using Eqs. (39), (46), and (178) and a few trivial changes of integration variables, these functions are

$$G_\pm\Big(\hat{s}, \frac{Q}{m_J}, \Gamma_t, \mu_\Lambda\Big) \equiv \int_{-\infty}^{+\infty} d\hat{s}' d\hat{s}'' d\ell' U_B(\hat{s} - \hat{s}', \mu_\Lambda, \mu_\Gamma) B_\pm^{\Gamma=0}\Big(\hat{s}' - \hat{s}'' - \frac{Q}{m_J}\ell', \mu_\Gamma, \delta m\Big) \tilde{S}_{\rm part}(\ell', \mu_\Lambda, \delta_1) \frac{\Gamma_t}{\pi(\hat{s}''^2 + \Gamma_t^2)}. \tag{184}$$

This result depends on $B_\pm^{\Gamma=0}$, the jet function for stable quarks in Eq. (142), and $\tilde{S}^{\rm part}$ the modified partonic soft function of Eq. (179). The form in Eq. (181) is derived from the factorization theorem given in Eq. (46), where the renormalization scales μ_Γ and μ_Λ were distinguished. This leads to the presence of the evolution factor U_B in Eq. (184), which is given at NLL in Eq. (79). The functions $G_\pm$, and hence all the ingredients in P, can be computed in perturbation theory, and analytic results for $G_\pm$ are given in Appendix E.

When quoting results at LL order we take U_B, U_{H_Q}, and U_{H_m} at LL order, and use tree-level results for $B_\pm^{\Gamma=0}$ and $\tilde{S}_{\rm part}$, including $\delta m = \delta_1 = 0$. The results quoted at NLL order use NLL evolution for U_B, U_{H_Q}, and U_{H_m}. They also include the $\mathcal{O}(\alpha_s)$ results for matching coefficients and matrix elements, including $B_\pm^{\Gamma=0}$, $\tilde{S}_{\rm part}$, δm, δ_1, $H_Q(Q, \mu_Q)$, and $H_m(m, \mu_m)$. These $\mathcal{O}(\alpha_s)$ terms have no-large logs, and in our numerical analysis we strictly drop all terms of $\mathcal{O}(\alpha_s^2)$ or higher in the product of these matching and matrix-element terms that appear in P. We also make use of the two-loop solution for the running coupling

$$\begin{aligned} \frac{1}{\alpha_s(\mu)} = {}& \frac{1}{\alpha_s(\mu_0)} + \frac{\beta_0}{2\pi} \ln\Big(\frac{\mu}{\mu_0}\Big) \\ & + \frac{\beta_1}{4\pi\beta_0} \ln\Big[1 + \frac{\beta_0}{2\pi}\alpha_s(\mu_0) \ln\Big(\frac{\mu}{\mu_0}\Big)\Big], \end{aligned} \tag{185}$$

with $\alpha_s(\mu_0 = m_Z) = 0.118$ as our reference value, and with β_0 and β_1 from Eq. (83). For the running above μ_m we take $n_f = 6$, while for the running below μ_m we take $n_f = 5$ (hence neglecting the b-quark threshold).

Since there are many features of the cross section formulae in Eqs. (180)–(184) that we wish to explore, it is useful to have a default set of parameters to use at both LL and NLL order. When not otherwise specified, we use the following values for our analysis below. Our default $Q/m_J = 5$, and the default renormalization scales are $\mu_Q = 5 * 172$ GeV, $\mu_m = 172$ GeV, $\mu_\Gamma = 5$ GeV, and $\mu_\Lambda = 1$ GeV. For results that involve the running jet mass we take as a reference value $m_J(\mu_0 = 2\ \text{GeV}) = 172$ GeV in the $L_m = 1$ GeV scheme, and evolve to other scales using Eq. (163) for $m_J(\mu)$. For results in the pole-mass scheme we also use $m_t^{\rm pole} = 172$ GeV. When the running gap is included we take as our reference value $\bar{\Delta}(\mu_0 = 1\ \text{GeV}) = 100$ MeV with $L_\Delta = 0.44$ GeV, and evolve to other scales using Eq. (177) for $\bar{\Delta}(\mu)$. We refer to this as the $\bar{\Delta}$ scheme. For results quoted without a renormalon free gap parameter we use $\Delta = 100$ MeV, and refer to this as the Δ scheme. Finally when studying perturbative aspects of the cross section our default model for the soft function $S_{\rm mod}(\ell^+, \ell^-, \bar{\Delta})$ in Eq. (170) is $(\Lambda, a, b) = (0.55\ \text{GeV}, 2.5, -0.4)$. Note that the dependence of $S_{\rm mod}$ on the model parameters Λ, a, and b is not shown explicitly in its arguments. We will explore deviations from these default parameters on a case-by-case basis.

A. Analysis of perturbative corrections and log summation

We begin our analysis by studying the perturbative corrections contained in the function

$$\tilde{\mathrm{P}}(M_t, M_{\bar{t}}) \equiv \mathrm{P}\left(\frac{M_t^2 - m_J^2 - Q\bar{\Delta}(\mu_\Lambda)}{m_J}, \frac{M_{\bar{t}}^2 - m_J^2 - Q\bar{\Delta}(\mu_\Lambda)}{m_J}, \mu_\Lambda\right). \tag{186}$$

This function $\tilde{\mathrm{P}}$ is convoluted with the soft-function model to give the cross section, as shown in the second line of Eq. (181). All of the dependence on the scales μ_Q, μ_m, μ_Γ, and μ_Λ cancels out in this function to the order we are working, and we can analyze the residual scale dependence of $\tilde{\mathrm{P}}$ to obtain an estimate of the remaining uncertainties from higher order corrections.

In Fig. 12 we demonstrate the effect of summing logs for the functions $m_J B_+(\hat{s}, \Gamma_t, \mu)$ (left panels, see Eq. (69)), $S(\ell, \ell, \mu)$ (center panels, see Eq. (59)), and $\tilde{\mathrm{P}}(M_t, M_t)$ (right panels, see Eq. (186)). For this plot we take $\mu = \mu_\Gamma = \mu_\Lambda$. The three top panels show LL results using the pole mass and Δ schemes. They demonstrate that increasing μ changes the shape of both B_+ and S. However, in the convolution that gives P these changes just reduce to a shift in the overall normalization, due to the consistency condition in Eq. (78). The three bottom panels show NLL results using the jet mass and $\bar{\Delta}$ schemes. At LL and NLL order the peak of B_+ moves to the left as we increase μ (top-left panel and bottom-left panel). At both LL and NLL order the peak of S moves to the right for increasing μ (central panels). The right panels show that at LL and NLL we still have a strong residual scale dependence in P, and that there is still a peak shift at NLL. This occurs because we have taken $\mu_\Gamma = \mu_\Lambda$ and not yet summed the large logs between μ_Γ and μ_Λ, where $\mu_\Gamma/\mu_\Lambda \simeq Q/m$. These remaining large logs can be seen explicitly in the formula in Eq. (E11).

This situation is rectified in Fig. 13, where we show results for $\tilde{\mathrm{P}}(M_t, M_t)$ with separated scales μ_Γ and μ_Λ. Again the top three panels are LL, and bottom three are NLL. In the left two panels we vary μ_Γ about $\mu_\Gamma = 5$ GeV holding $\mu_\Lambda = 1$ GeV fixed. We use the range $\mu_\Gamma =$ 3.3–7.5 GeV to estimate the scale uncertainty because of the importance of not upsetting the $\mu_\Gamma/\mu_\Lambda \simeq Q/m$ relation too severely. (For contrast the blue dashed curve in the lower-left panel shows the result for $\mu_\Gamma = \mu_\Lambda = 1$ GeV.) In the center panels we hold $\mu_\Gamma = 5$ GeV and instead vary $\mu_\Lambda = 0.8$–1.2 GeV (where variation below 0.8 GeV is not advisable since α_s has grown to 0.45 at this scale). The dashed vertical line shows the input value of the short-distance mass, $m_J(\mu_0 = 2\ \mathrm{GeV}) = 172$ GeV, while the solid vertical line shows the shift due to the gap, $M_{\bar{t}} = [m_J^2(\mu_0) + Q\bar{\Delta}]^{1/2} \simeq 172.25$ GeV, with $\bar{\Delta}(1\ \mathrm{GeV}) = 0.1$ GeV. Finally in the two right panels we show how the μ-variation of the center panels is reduced if we vary μ_Λ in the same range, but simultaneously change μ_Γ so that $\mu_\Gamma/\mu_\Lambda = Q/m$ is fixed. Because of this sizeable

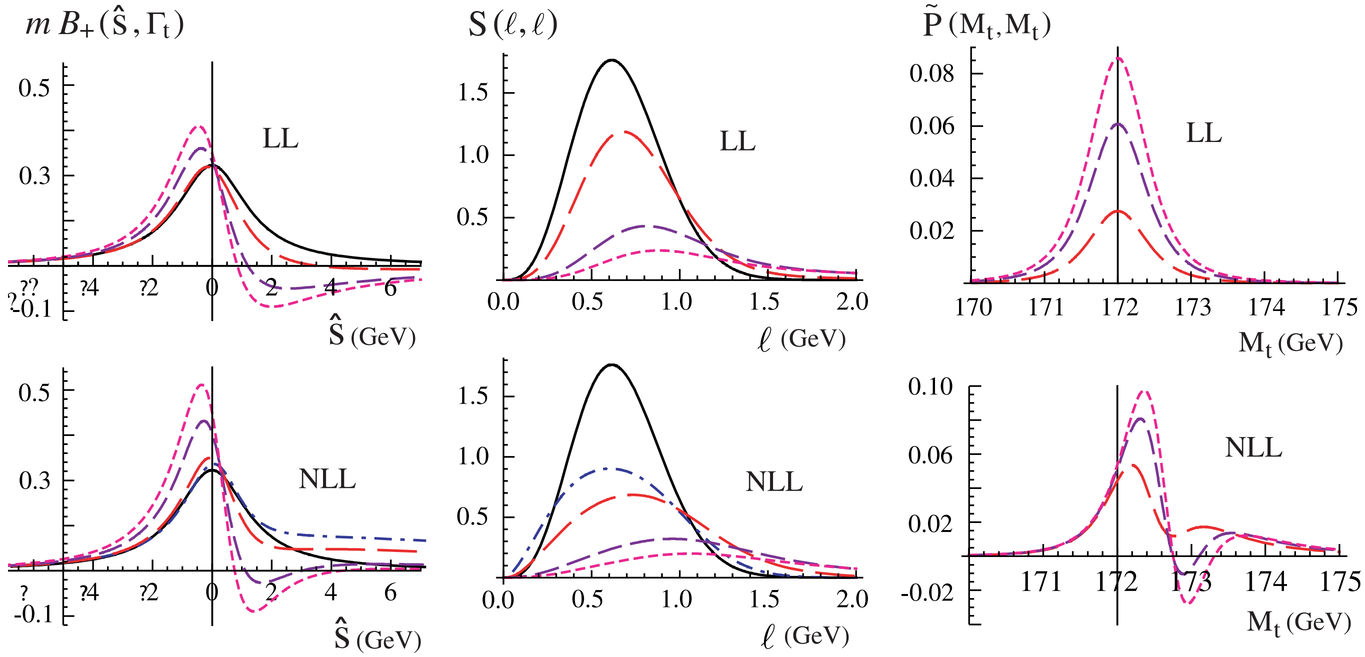

FIG. 12 (color online). Renormalization-group evolution of the jet function, $m_J B_+(\hat{s}, \Gamma_t, \mu)$ (left panels), the diagonal soft function $S(\ell, \ell, \mu)$ (center panels), and the function $\tilde{P}(M_t, M_t)$ in Eq. (186) (right panels) with $\mu = \mu_\Gamma = \mu_\Lambda$. The top three panels show LL results, while the bottom three are NLL results. For the left and center panels the curves are tree level (black solid line), NLO at $\mu = 1$ GeV (blue dot-dashed lines), and curves which evolve at LL or NLL order from $\mu_0 = 1$ to $\mu = 1.5$, 4.0, 7.0 GeV (red, purple, magenta, with decreasing dash sizes, respectively). The right panels show only these last three curves.

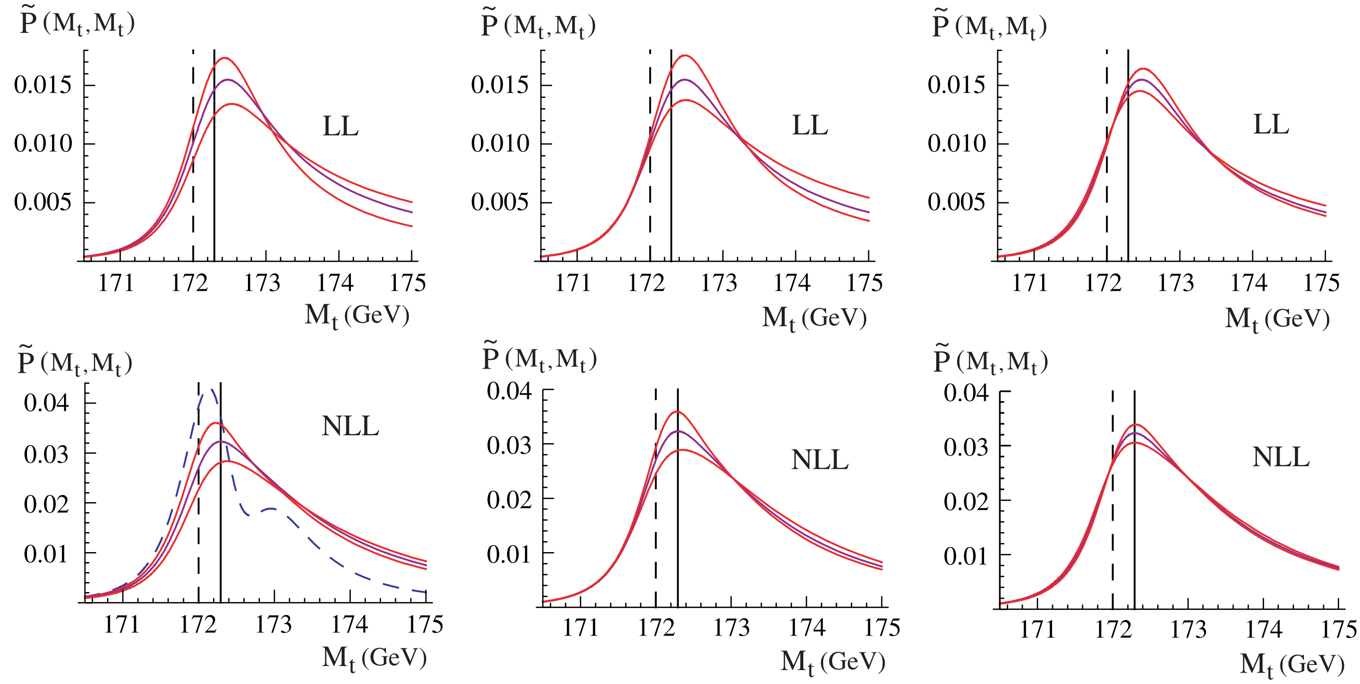

FIG. 13 (color online). The μ_Γ and μ_Λ scale dependence of the perturbative contributions, $\tilde{P}(M_t, M_t)$. The top panels show LL results, while bottom panels show NLL results. Central values are $\mu_\Gamma = 5$ GeV and $\mu_\Lambda = 1$ GeV. In the left panels the solid curves are for $\mu_\Gamma = 3.3, 5, 7.5$ GeV (from top to bottom at the peak), while the blue-dashed line shows the result when $\mu_\Gamma = \mu_\Lambda = 1$ GeV. In the central panels the solid curves are for $\mu_\Lambda = 0.8, 1.0, 1.2$ GeV (from bottom to top at the peak). The right panels are the same as the central panels, except that we also change μ_Γ so that $\mu_\Gamma/\mu_\Lambda = Q/m = 5$ remains fixed.

correlation the overall uncertainty is smaller than from naively summing the uncertainties from the left and center panels in quadrature. We believe that an uncertainty in the shape that is of order the μ_Γ variation shown in the left panels gives a reasonable error estimate. From comparing the percent change at LL and the percent change at NLL we see that there is a reduction to the μ-variation in all cases, particularly in the cross section above the peak.

In Fig. 14 we show results for the μ_m and μ_Q scale dependence of $\tilde{P}(M_t, M_t)$ (left and central panels, respectively). We increase and decrease μ_m and μ_Q by a factor of 2, and both variations exhibit rather small scale uncertainty. Here we show LL and NLL as the bottom and top three curves inside each panel. As is often the case in jet physics, we note that there is a sizeable change to the normalization of the cross section in going from LL to

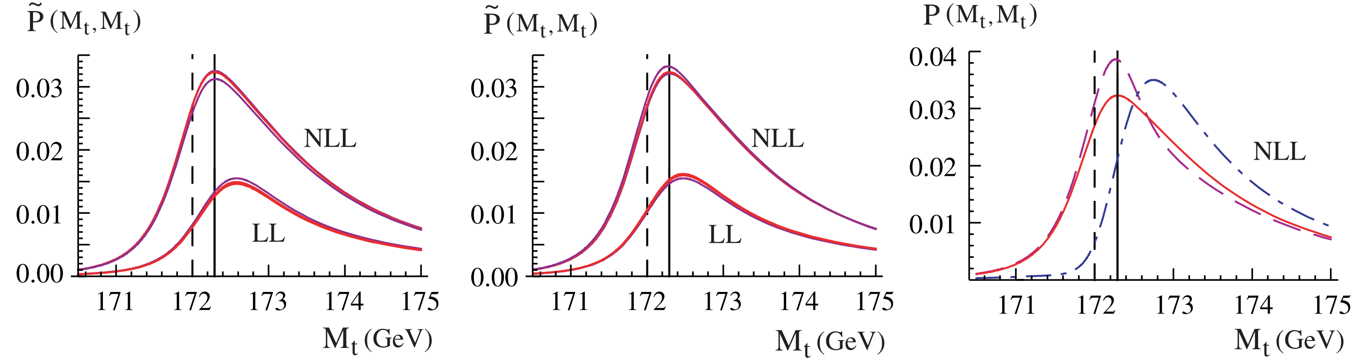

FIG. 14 (color online). $\tilde{P}(M_t, M_t)$ versus M_t. Left panel shows the μ_m dependence at LL (bottom curves) and NLL (top curves) taking $\mu_m = 86, 172, 344$ GeV. Central panel shows the μ_Q dependence at LL (bottom curves) and NLL (top curves) taking $\mu_Q = 430, 860, 1720$ GeV. The right panel shows the effect of using renormalon free gap and mass parameters, where the red solid curve includes both. The purple dashed curve turns off the renormalon subtractions for the mass (thus using the pole-mass scheme), and the blue dot-dashed curve turns off the renormalon subtraction for the gap.

NLL order. The vertical lines are the same as in Fig. 13. In the right-most panel of Fig. 14 we show the effect of using the renormalon free jet mass and renormalon free gap parameter $\bar{\Delta}$ (solid red curve) in contrast to turning off the renormalon subtraction for the mass, i.e. when using the top-quark pole scheme (purple dashed curve), and turning off the renormalon subtraction for the gap (blue dot-dashed curve). Even at $\mathcal{O}(\alpha_s)$ the importance of having a renormalon free soft function with $\bar{\Delta}$ is clearly visible.

B. Cross section in the peak region

Having examined the scale dependence of the perturbative corrections we now turn to the convolution with the soft function that gives the normalized cross section $F(M_t, M_{\bar{t}}, m_J, Q/m_J)$ in Eq. (181). For most of our plots we keep the soft-function model fixed, having in mind that it can be extracted from LEP data. In Fig. 15 we show F at NLL for our default parameter set as a function of the two invariant mass variables M_t and $M_{\bar{t}}$. The underlying short-distance quark mass is $m_J(\mu = 2\ \text{GeV}) = 172$ GeV, and the peak of the cross section occurs for M_t and $M_{\bar{t}}$ values which are $\simeq 2.4$ GeV larger. This peak shift occurs due to the presence of the low energy radiation described by the soft function as discussed in Ref. [2]. At LO the shift is in the positive direction to $M_t^{\text{peak}} \simeq m_J + QS^{[1,0]}_{\text{mod}}/(2m_J)$, where here $S^{[1,0]} = \int d\ell^+ d\ell^- \ell^+ S_{\text{mod}}(\ell^+, \ell^-) \sim \Lambda_{\text{QCD}}$ is the first moment of the underlying soft-function model [2]. As described below, this linear behavior with Q/m persists at NLL order, although the slope is no longer simply $S^{[1,0]}_{\text{mod}}$. Above the peak one sees in Fig. 15 the perturbative tails from gluon radiation, and that the tails are largest if we fix one of M_t or $M_{\bar{t}}$ at the peak.

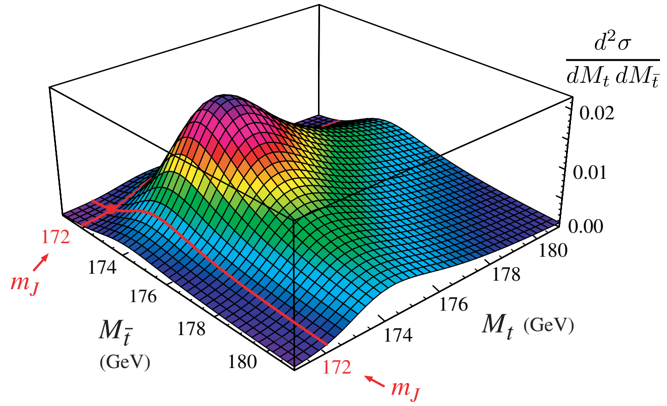

FIG. 15 (color online). $F(M_t, M_{\bar{t}})$, the differential cross section in units of σ_0/Γ_t^2, versus M_t and $M_{\bar{t}}$. The result is shown at NLL order.

In order to analyze the parameter dependence of the cross section we will now consider the diagonal $F(M_t, M_t, m_J, Q/m_J)$, which we simply referred to as $F(M_t, M_t)$ in the analysis that follows. In Fig. 16, in the left panel, we show LL curves (bottom three lines) and NLL curves (top three lines) using $\mu_\Gamma = 3.3, 5.0, 7.5$ GeV in the jet mass and $\bar{\Delta}$ scheme. We find that the peak of the cross section is very stable to the variation of μ_Γ, and changes very little from LL to NLL order. As explained above, by far the dominant contribution of the shift of the peak away from the input short-distance jet mass is due to the underlying soft function, shown here by the difference between the dashed and solid lines. In the central panel we show again the NLL order cross sections in the jet mass and $\bar{\Delta}$ scheme (red curves) and compare it to the NLL predictions in the pole-mass scheme for the same three μ_Γ values (blue curves). The results show that in the pole-mass scheme there is more variation of the peak position than in the jet-mass scheme. Finally in the right panel we show variations of the cross section in comparing the renormalon free $\bar{\Delta}$ scheme (red curves) and the gap with a renormalon ambiguity in the Δ scheme (magenta curves). This figure demonstrates that the effect of the switching to a renormalon free gap scheme is larger than the residual μ_Γ dependence at NLL order.

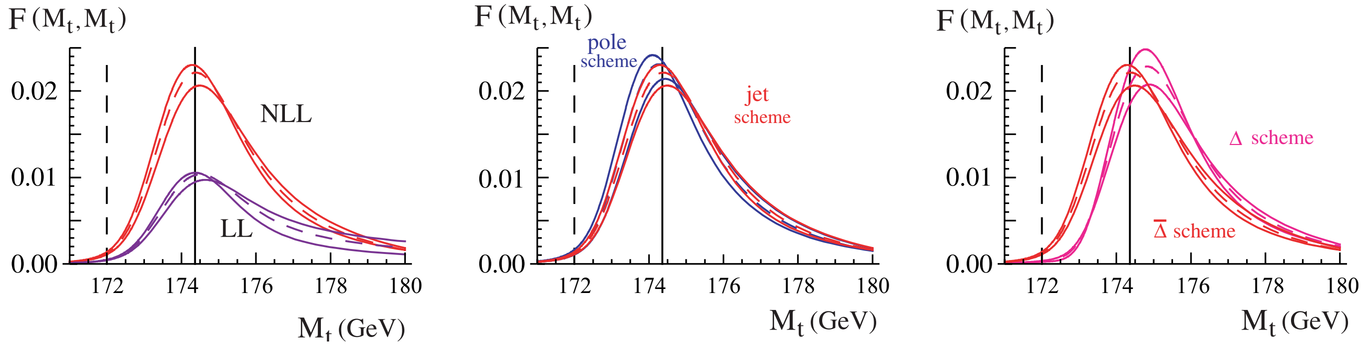

FIG. 16 (color online). Normalized peak cross section, $F(M_t, M_t)$ versus M_t. The dashed curves have $\mu_\Gamma = 5$ GeV, and the solid curves have $\mu_\Gamma = 3.3, 7.5$ GeV. The left panel shows results at LL (lower purple curves) and NLL (upper red curves) with the jet and $\bar{\Delta}$ schemes. The center panel shows results in the jet-mass scheme (red) versus the pole-mass scheme (blue), where in both cases we use the $\bar{\Delta}$ scheme. The right panel shows results in the $\bar{\Delta}(\mu)$ scheme for the gap parameter (red) versus the Δ scheme (magenta), where in both cases we use the jet-mass scheme.

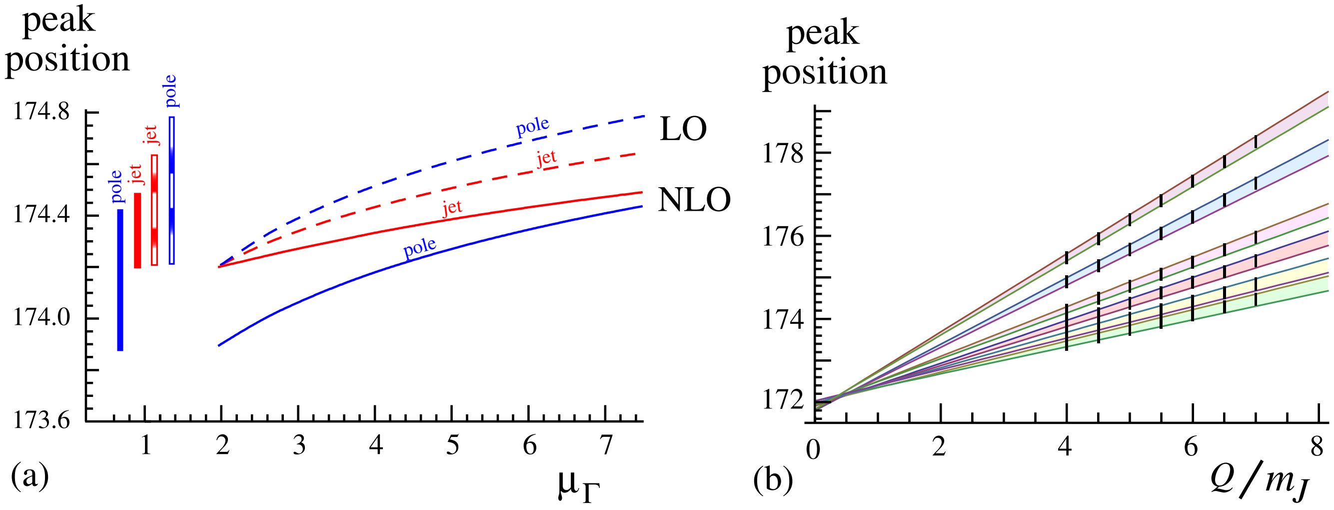

FIG. 17 (color online). (a) Peak position of the single differential distribution $d\sigma/dM_t dM_{\bar{t}}(M_t, M_t)$ as a function of μ_Γ. Red curves use the jet mass and $\bar{\Delta}$ scheme and blue curves use the pole mass and Δ scheme. Dashed curves are LL order, and solid curves are NLL order. The bars to the left show the size of the scale variation and left to right correspond to the curves from bottom to top. (b) The solid curves show the peak position versus Q/m for six different models which from top to bottom are $(a, b) = (3.5, -0.8)$ (purple), $(a, b) = (2.5, -0.8)$ (blue), $(a, b) = (3.5, -0.4)$ (magenta), $(a, b) = (2.5, -0.4)$ (red), $(a, b) = (3.5, 0.4)$ (yellow), and $(a, b) = (2.5, 0.4)$ (green). The solid curves show a linear fit using the values at $Q/m = 4$ and 5. Extrapolated to $Q/m = 0$ any line converges on the underlying short-distance mass, independent of the soft-radiation model, yielding $m_t(\mu = 5\text{ GeV}) = 171.9 \pm 0.1$ GeV.

The μ_Γ dependence of the peak position is shown more explicitly in the left panel of Fig. 17. In the pole scheme (blue curves) we see that there is very little change to the μ_Γ dependence in going from LL (dashed blue curve) to NLL (solid blue curve). In contrast in the jet-mass scheme (red curves) the μ_Γ dependence is already smaller at LL order (dashed red curve), and is significantly reduced by the NLL results (solid red curve). In the right panel of Fig. 17 we plot as black ticks results for the peak position versus Q/m using six different models for the soft function with $\mu_\Gamma = 5$ GeV. It is clearly visible that the peak is shifted in a linear fashion with Q/m_J, with a slope that is model dependent. For each model the solid lines show a fit to the peak position for $\mu_\Gamma = 3.3$ GeV and $\mu_\Gamma = 7.5$ GeV with a solid band to show the uncertainty from this μ-dependence. The fits are done using the points at $Q/m = 4$ and 5. Extrapolating back to $Q/m = 0$ removes the dependence on the soft radiation, and we see that for any soft-function model the intercept determines the short-distance mass parameter $m_J(\mu = 5\text{ GeV}) = 171.9$ GeV. From the spread of the curves we have $\simeq 0.13$ GeV theoretical uncertainty in this determination of the short-distance mass. This provides a method for determining the short-distance mass even if the soft function is unknown. In order to maintain the perturbative stability of the relation of this intercept with the top mass it is important to use the jet-mass scheme.

C. Cross section in the tail region

The tail region of the cross section is characterized by invariant masses where $\hat{s} \gg \Gamma$. In this region we are varying M_t and hence $\hat{s}$ over a large range, and it becomes necessary to scale $\mu_\Gamma \sim \hat{s}$ and $\mu_\Lambda \sim \hat{s} m_J/Q$ to avoid having large logarithms that spoil the perturbative expansion. We therefore define reference scales for the tail region,

$$\mu_\Gamma^0 = \sqrt{\left[\frac{M^2 - m_J^2(2\text{ GeV})}{m_J(2\text{ GeV})}\right]^2 + (5\text{ GeV})^2}, \qquad \mu_\Lambda^0 = \sqrt{\left[\frac{M^2 - m_J^2(2\text{ GeV})}{Q}\right]^2 + (1\text{ GeV})^2}, \tag{187}$$

where $m_J(2\text{ GeV}) = 172$ GeV, and we study the scale dependence by varying μ_Γ and μ_Λ about these results. In Fig. 18 we show the perturbative function $\tilde{\mathrm{P}}$ from Eq. (186) at LL order (dashed curves) and NLL order (solid curves). The left panel varies μ_Γ by 50% about μ_Γ^0 holding $\mu_\Lambda = \mu_\Lambda^0$ fixed, while the central panel varies μ_Λ holding $\mu_\Gamma = \mu_\Gamma^0$ fixed. In contrast to the peak region we now plot the cross section over a log scale. Note that the LL results exhibit larger uncertainty in this tail region, which is again substantially improved by the NLL results. In the rightmost panel we vary μ_Λ as in the central panel, but now take $\mu_\Gamma/\mu_\Lambda = Q/m$ as fixed. Just as in the peak region this choice substantially reduces the scale uncertainty, indicating once again that simply adding the individual variations of μ_Γ and μ_Λ very likely overestimate the size of higher order perturbative corrections. Finally since $\hat{s}$ increases in the tail region, the uncertainty from the power expansion also increases as we require $v \cdot k/m = \hat{s}/(2m) \simeq (M_t - m_J)/m_J \ll 1$. At $M_t = 185$ GeV this is an expansion in $1/12$ and by $M_t = 200$ GeV it is an expansion in $1/6$, both

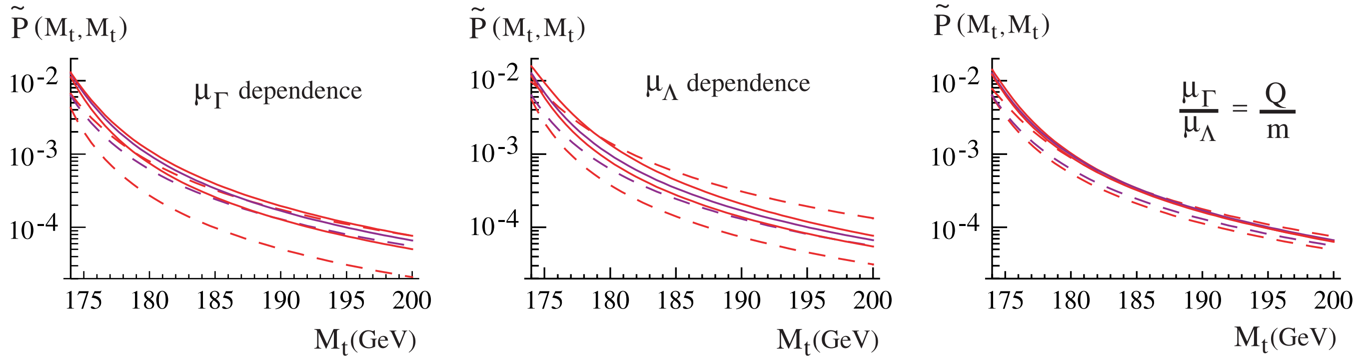

FIG. 18 (color online). Perturbative contributions, $\tilde{P}(M_t, M_t)$ in the tail region at LL (dashed curves) and NLL (solid curves). In the left panel we take $\mu_\Lambda = \mu_\Lambda^0$ and plot three curves with $\mu_\Gamma = \{0.5, 1.0, 1.5\}\mu_\Gamma^0$. In the center panel we take $\mu_\Gamma = \mu_\Gamma^0$ and show three curves with $\mu_\Lambda = \{0.5, 1.0, 1.5\}\mu_\Lambda^0$. In the right panel we show $\mu_\Gamma = \{0.5, 1.0, 1.5\}\mu_\Gamma^0$ with $\mu_\Lambda = \mu_\Gamma m_J(2\text{ GeV})/Q$. Here μ_Γ^0 and μ_Λ^0 are given in Eq. (187).

of which are larger than the ratio $\simeq 1/100$ that we have in the peak region.

In Fig. 19 we convolute P with the soft-function model as in Eq. (181), and plot the normalized cross section F over both the peak and tail regions. The three panels show the same μ-variations as Fig. 18. These plots show one of the attractive features of our treatment of the soft function. In the tail region there are perturbative corrections in the soft function that are important for determining the cross section, and there is also an important power correction due to the first moment of the model function S_{mod}. Both of these are included in our analysis by using the full $S(\ell^+, \ell^-, \mu)$ function from Eq. (169) as explained in Ref. [30]. In the peak region these terms naturally interpolate into a full model soft function in a consistent manner. Once again we see from the third panel of Fig. 19 that taking $\mu_\Gamma/\mu_\Lambda = Q/m_J$ leads to quite small μ-dependence for the entire cross section. Finally in Fig. 20 we show the effect that variation of the soft-function model has on the cross section in the tail region. The effect of the soft function becomes larger as we get closer to the peak region, as expected. Since the cross section has already dropped by two orders of magnitude by $M_t = 200$ GeV we have not bothered to analyze it in the ultra-tail region, $M_t - m_J \sim m_J$, where it is further suppressed by several more decades. However, in Appendix F we do give formulas for the cross section in the ultra-tail region, which are analogous to the ones used for our analysis of the peak and tail cross sections. These formulae could be useful as a means of estimating top-quark backgrounds from $t\bar{t}$ events for other processes in the ultra-tail region.

D. Thrust

Starting from the two-dimensional distribution, $d^2\sigma/dM_t^2 dM_{\bar{t}}^2$ in Eq. (180) it is straightforward to derive results for other event-shape variables for massive particles. For example, for the thrust T, we have $1 - T \equiv \tau = (M_t^2 + M_{\bar{t}}^2)/Q^2$, so

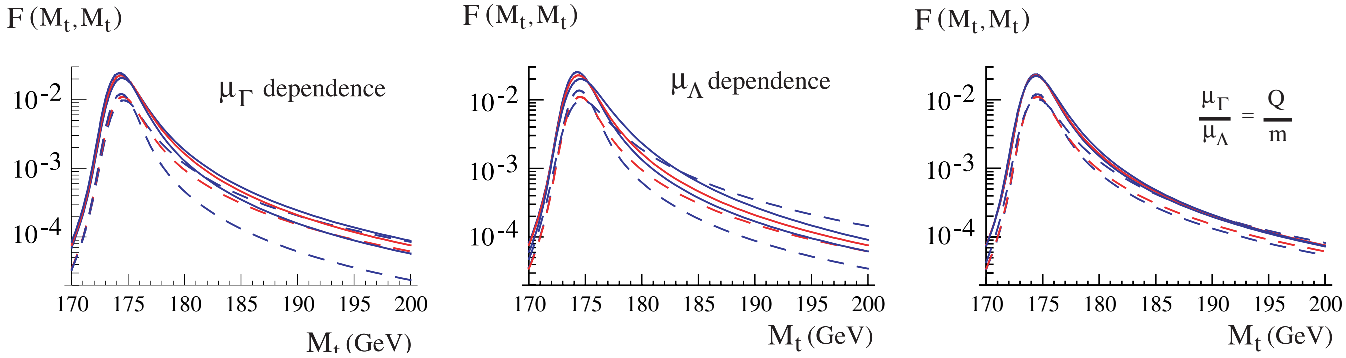

FIG. 19 (color online). Cross section plotted over both the peak and tail regions at LL order (dashed line) and NLL order (solid line). In the left panel we take $\mu_\Lambda = \mu_\Lambda^0$ and plot three curves with $\mu_\Gamma = \{0.5, 1.0, 1.5\}\mu_\Gamma^0$. In the center panel we take $\mu_\Gamma = \mu_\Gamma^0$ and show three curves with $\mu_\Lambda = \{0.5, 1.0, 1.5\}\mu_\Lambda^0$. In the right panel we show $\mu_\Gamma = \{0.5, 1.0, 1.5\}\mu_\Gamma^0$ with $\mu_\Lambda = \mu_\Gamma m_J(2\text{ GeV})/Q$.

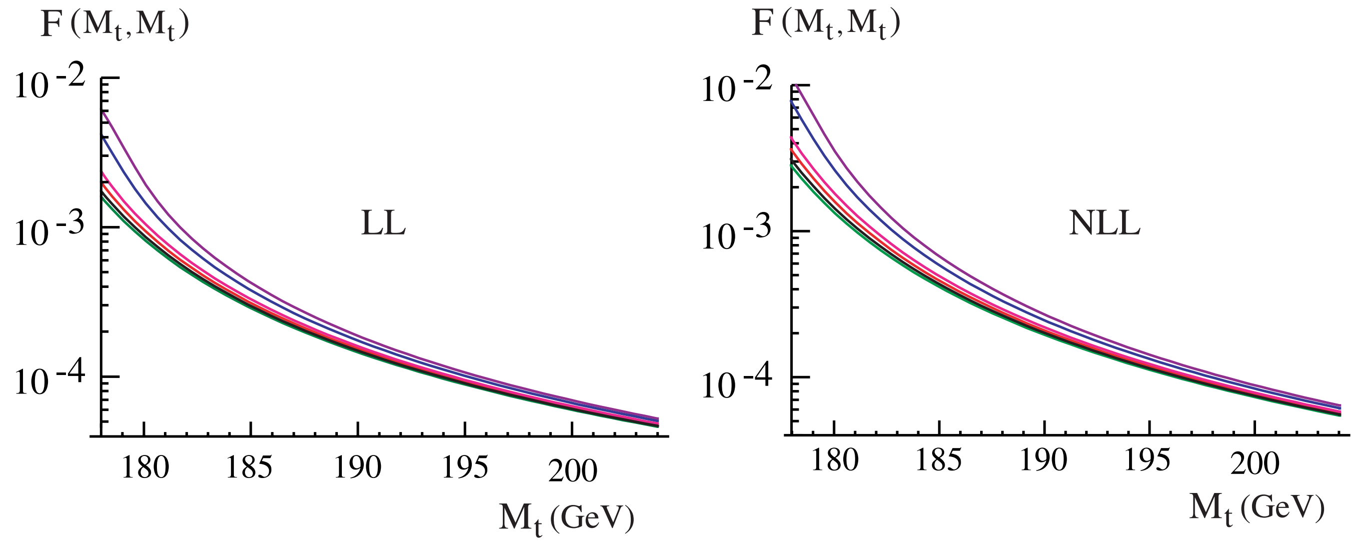

FIG. 20 (color online). Variation of the tail cross section using different soft-function models at LL (left panel) and NLL (right panel). The curves are $(a, b) = (3.5, -0.8)$ (purple), $(a, b) = (2.5, -0.8)$ (blue), $(a, b) = (3.5, -0.4)$ (magenta), $(a, b) = (2.5, -0.4)$ (red), $(a, b) = (3.5, 0.4)$ (black), and $(a, b) = (2.5, 0.4)$ (green).

$$\begin{aligned}\frac{1}{\sigma_0}\frac{d\sigma}{dT} &= \int_0^\infty dM_t^2 \int_0^\infty dM_{\bar t}^2\, \delta\Big(\tau - \frac{M_t^2 + M_{\bar t}^2}{Q^2}\Big)\frac{1}{\sigma_0} \\ &\quad\times \frac{d^2\sigma}{dM_t^2 dM_{\bar t}^2} \\ &= \int_0^\infty d\ell\, \mathrm{P_T}\Big(\frac{Q^2\tau - 2m_J^2 - Q\ell - 2Q\bar\Delta(\mu_\Lambda)}{m_J}, \mu_\Lambda\Big) \\ &\quad\times S_{\rm mod}^{\rm symm}(\ell, 0). \end{aligned} \tag{188}$$

The perturbative contributions are grouped into the dimensionless function $\mathrm{P_T}$ which is a projection of our function P,

$$\mathrm{P_T}(\hat s, \mu_\Lambda) \equiv \int_{-\infty}^{+\infty} d\hat s_d \frac{m_J Q^2}{8 M_t M_{\bar t} \Gamma_t^2} \mathrm{P}\Big(\frac{\hat s + \hat s_d}{2}, \frac{\hat s - \hat s_d}{2}, \mu_\Lambda\Big). \tag{189}$$

Here under the $\hat s_d$ integral $M_t^2 = m_J^2 + m_J(\hat s + \hat s_d)/2$ and $M_{\bar t}^2 = m_J^2 + m_J(\hat s - \hat s_d)/2$. An analytic formula for $\mathrm{P_T}$ is derived in Appendix G. The appropriate soft function for thrust, $S_{\rm mod}^{\rm symm}(\ell)$ in Eq. (188), is also simply a projection of the model for the hemisphere soft function, $S_{\rm mod}(\ell^+, \ell^-, \Delta)$, where

$$S_{\rm mod}^{\rm symm}(\ell, 0) = \int_0^\infty d\ell^+ d\ell^- \delta(\ell - \ell^+ - \ell^-) S_{\rm mod}(\ell^+, \ell^-, 0). \tag{190}$$

For the exponential model in Eq. (170) this projection gives

$$S_{\rm mod}^{\rm symm}(\ell, 0) = \frac{\mathcal{N}(a, b)}{\Lambda} \frac{\sqrt{\pi}\Gamma(a)}{\Gamma(a + \frac{1}{2})}\Big(\frac{\ell}{2\Lambda}\Big)^{2a-1} {}_1F_1\Big(\frac{1}{2}, \frac{1}{2} + a, \frac{(b-1)\ell^2}{2\Lambda^2}\Big) e^{-(1+b)\ell^2/(2\Lambda^2)}, \tag{191}$$

where $\{a, b, \Lambda\}$ are the model parameters and $\mathcal{N}(a, b)$ is the same normalization constant as in Eq. (170).

In Fig. 21 we plot the thrust distribution at LL order (dashed curves) and NLL order (solid curves) for events which were initiated by the massive unstable top quarks in e^+e^- collisions. Since the plot includes values in the tail region we use the reference scales

$$\begin{aligned}\mu_\Gamma^0 &= \sqrt{\frac{Q^4}{4m_J^2}\Big(\tau - \frac{2m_J^2}{Q^2}\Big)^2 + (5\ \mathrm{GeV})^2}, \\ \mu_\Lambda^0 &= \frac{1}{0.8}\frac{\mu_\Gamma^0 m_J}{Q}, \end{aligned} \tag{192}$$

where $\tau = 1 - T$. Taking $\mu_\Gamma \simeq \mu_\Gamma^0$ and $\mu_\Lambda \simeq \mu_\Lambda^0$ ensures that the logs involving these parameters do not grow substantially over the region plotted. Our choice for μ_Λ here is slightly larger than the ones used earlier. This is because of the effective doubling of the anomalous dimensions for the thrust cross section (see Appendix G), which necessitates using slightly larger values for μ_Λ to avoid the region where large values for α_s cause a breakdown in perturbation theory.

The threshold for thrust for two-massive particles is given by $1 - T = 2m_J^2/Q^2$ and is shown by the vertical dashed lines in Fig. 21. Just as for the invariant mass distribution, there is a peak in the thrust cross section and

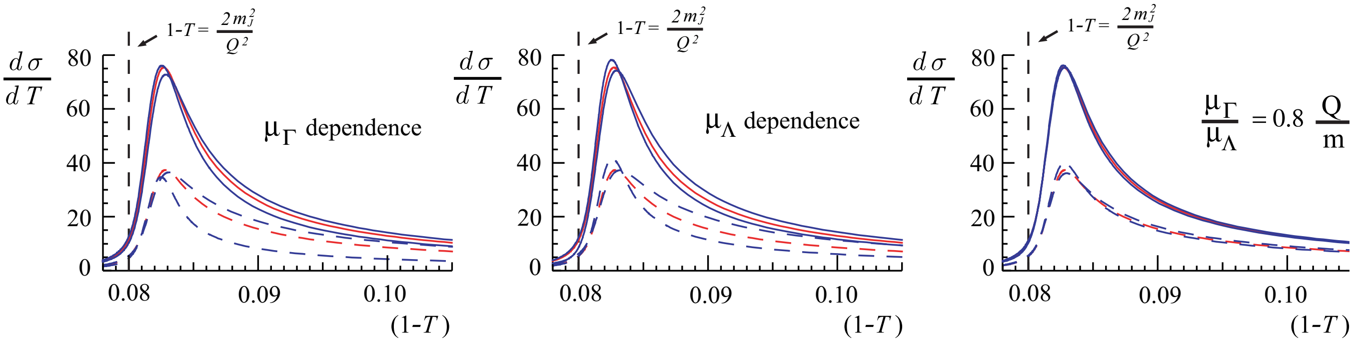

FIG. 21 (color online). Thrust distribution, $d\sigma/dT$ in units of σ_0, plotted versus $1-T$ at LL (dashed curves) and NLL (solid curves). In the left panel we take $\mu_\Lambda = \mu_\Lambda^0$ and plot three curves with $\mu_\Gamma = \{0.5, 1.0, 1.5\}\mu_\Gamma^0$. In the center panel we take $\mu_\Gamma = \mu_\Gamma^0$ and show three curves with $\mu_\Lambda = \{0.7, 1.0, 1.5\}\mu_\Lambda^0$. In the right panel we show $\mu_\Lambda = \{0.7, 1.0, 1.5\}\mu_\Lambda^0$ with $\mu_\Gamma = \mu_\Lambda[0.8Q/m_J(2\text{ GeV})]$.

it is shifted above the massive particle threshold due to soft-radiation effects by an amount $\simeq 2\Lambda_{\rm QCD}/Q$. The analog of this for massless jets is a peak in the thrust distribution at values $1-T \simeq 2\Lambda_{\rm QCD}/Q$ (see for example [22]), which is a shift above the massless dijet threshold at $1-T=0$. The three panels in Fig. 21 show the μ-dependence of our NLL results, varying μ_Γ in the left panel, μ_Λ in the center panel, and μ_Λ with $\mu_\Gamma/\mu_\Lambda = 4$ fixed in the right panel (since here $Q/m_J = 5$). Again we see that there is very small μ-dependence when μ_Γ and μ_Λ are varied in a correlated fashion. We believe the left panel gives a reasonable estimate of the perturbative uncertainties in the shape of the thrust distribution. An analysis of the thrust-distribution peak for different values of Q could also be used to extract the short-distance top-mass parameter.

IX. CONCLUSION

Precise measurements of the top-quark mass m_t belong to the most important standard measurements carried out at the Tevatron and the LHC. The most sensitive method relies on the reconstruction of the top-quark invariant mass distribution through measurements of the energies and momenta of jets from the top decay. While considerable work has and is being invested to control experimental systematic effects, very little theoretical work exists which studies both perturbative and nonperturbative QCD aspects of the resulting invariant mass distribution. Also, to our knowledge, there has been no theoretical work on how the shape and the resonance mass of this distribution are related to a short-distance top-mass parameter in the QCD Lagrangian.

In Ref. [2] we derived the factorization theorem in Eq. (3) which describes the simpler environment of e^+e^- collisions. It predicts the double differential invariant mass distribution $d^2\sigma/dM_t^2 dM_{\bar t}^2$ in the resonance region for the large c.m. energies $Q \gg m_t$, where $M_{t,\bar t}$ are the total invariant masses of all particles in the two hemispheres determined with respect to the event thrust axis. The factorization represents the leading order result in a power expansion in m/Q and Γ/m, and these corrections are indicated in Eq. (3). Here Γ is the width of the invariant mass distribution, which is larger than the underlying total width of the top quarks Γ_t. The derivation was based on the hierarchy $Q \gg m_t \gg \Gamma, \Lambda_{\rm QCD}$, where $\Lambda_{\rm QCD}$ is the hadronization scale and uses the effective theories SCET and HQET to achieve a separation of different physical effects associated to Q, m_t, Γ_t, and $M_{t,\bar t}$ and $\Lambda_{\rm QCD}$. For the systematic inclusion of mass and width effects the use of both effective theories was crucial. The factorization theorem separates perturbative from nonperturbative effects and represents the leading order term in the power expansion, but is valid to all orders in the expansion in α_s.

In this paper we extended the presentation given in Ref. [2] and presented detailed computations of the different pieces entering the factorization theorem in the peak region at NLL order. We also presented NLL predictions for the tail of the invariant mass distribution, where $M_{t,\bar t}$ are above the resonance peak. The double invariant hemisphere mass distribution is itself an event-shape distribution that can be related to other event-shape variables such as thrust or jet masses in a straightforward way. The factorization formula consists of several functions that can be computed perturbatively order by order in α_s, including hard coefficients for the scales Q and m, and two jet functions for the top and antitop quarks which depend strongly on the top-quark Lagrangian mass. It also involves a nonperturbative soft function that describes the momentum distribution of soft final state radiation. Using alternative invariant mass prescriptions, for which the soft particles are assigned differently to M_t and $M_{\bar t}$, the same factorization formula applies, but with a different soft function. In the tail region the soft function also contains perturbatively calculable corrections.

Our analysis uses effective theory techniques. In particular we calculated Wilson coefficients that arise from matching QCD onto SCET, and from matching SCET onto bHQET to NLO. In addition we calculated the NLL running: first between the scales Q and m using anomalous dimensions of operators in SCET, and then between the scales m and Γ and between Γ and Λ using anomalous dimensions of operators in bHQET. The perturbative corrections, including resummation, are given by simple analytic functions, and our strategy for computing these functions naturally generalizes for future analytic computations at NNLL order. One important result of our analysis is that in the peak region the running between the scales Q, m, and Γ is local, it only changes the overall normalization and not the shape of the invariant mass distribution. Thus only large logs between the scales Γ and Λ can shift the shape of the distribution. This is encoded in consistency equations for the renormalization-group evolution functions entering the factorization theorem.

The observable invariant mass distribution is obtained from a convolution of the jet functions with the soft function. Through this convolution the energy of the peak and the width of the observed distribution are dependent on the center-of-mass energy Q. In particular, nonperturbative effects described by the soft function shift the resonance peak position towards larger masses, and broaden the distribution. In Ref. [2] we demonstrated that the soft function for the hemisphere mass prescription can be determined from event-shape distributions for massless dijet events, and that the dependence on the mass scheme is controlled through the perturbative expansion of the jet function. This allows in principle for a top-quark mass determination that is free of hadronization uncertainties. Even if the soft-function is not known from measurements of massless jets, one can still extract the short-distance mass parameter using an analysis like the one described in Fig. 17. We have demonstrated that these statements remain true in the presence of perturbative corrections and with the summation of large logs. We also introduced the so-called jet-mass scheme to define the Lagrangian top-mass parameter. This is a top-quark short-distance mass scheme that is particularly suited to mass determinations related to the resonance peak position, since it makes the peak position stable to the inclusion of perturbative corrections. One-loop relations of this jet mass to the $\overline{\text{MS}}$-mass and 1S-mass schemes were given in Sec. VI, as well as the LL evolution formula for the jet mass. For the construction of the soft function at NLL order we used results from Ref. [30] where a soft model function is convoluted with the soft-function contributions determined from fixed order perturbation theory. This soft function works equally well in the peak and tail regions. To avoid large higher order corrections it was necessary to introduce a gap parameter in the soft function that accounts for the fact that there is a minimal hadronic energy for the soft radiation between the jets. This parameter allows us to make the perturbative corrections in the soft function free from an $\mathcal{O}(\Lambda_{\text{QCD}})$ renormalon ambiguity.

In our numerical analysis we analyzed the hemisphere mass distribution on the peak and away from the peak, and the thrust distribution. We demonstrated that NLL order corrections are important and need to be accounted for to make viable predictions. We also showed that it is important to sum the large logs between $\mu_\Gamma \simeq \Gamma$ and $\mu_\Lambda \gtrsim \Lambda$ to avoid sizeable scale uncertainties. We also studied the impact of the jet-mass scheme, and showed that it improves predictions for the resonance peak position in comparison to the pole-mass scheme. For mass measurements this result implies that the jet mass can be determined from mass reconstruction more accurately than the pole mass which is known to suffer from renormalon ambiguities. In our NLL analysis we demonstrated that the perturbative corrections associated to the gap parameter improve significantly the perturbative behavior of predictions in the peak and in the tail region. This result implies that soft functions that account for a gap as proposed in Ref. [30] are crucial for precise measurements of the top-quark mass and the model parameters from experimental data. Finally we also presented a NLL prediction for the thrust distribution for top pair production in the region of large thrust. To our knowledge this NLL result presents for the first time a full resummed event-shape distribution for massive quarks. The thrust distribution has a strong dependence on the mass and can serve as an alternative way of measuring heavy quark masses. Our numerical analysis can be extended to make predictions for bottom quark production by taking the limit $\Gamma_t \rightarrow 0$. It would also be interesting to study the $\alpha_s m_t/Q$ and m_t^2/Q^2 power corrections, which can be accomplished in our effective field theory setup.

Through our detailed calculations of the jet invariant mass distributions and their relation to the top-quark mass, we have demonstrated the viability of extracting the top mass with high precision at a future linear collider such as the ILC. In principle, a precision of better than Λ_{QCD} can be achieved since there is a clear relation between the top-mass Lagrangian parameter and the physically observed jet invariant mass distribution. In the future we intend to extend the work presented here and in Ref. [2] to the study of top-mass reconstruction at the LHC.

ACKNOWLEDGMENTS

We would like to thank B. Holdom, A. Juste, V. Khoze, S. Kluth, J. H. Kühn, S. Menke, M. Peskin, and G. Salam for helpful discussions and communication. We thank the Max-Planck Institute for Physics for hospitality while parts of this work were completed. This work was supported in part by the Department of Energy Office of Nuclear Science under the grants No. DE-FG02-94ER40818 and No. DE-FG03-92ER40701, and in part by the EU network Contract No. MRTN-CT-2006-035482 (FLAVIAnet).

APPENDIX A: SUMMARY OF FEYNMAN DIAGRAMS IN SCET

In this appendix we list results for the individual Feynman diagrams used in the body of the paper in Sec. IV.

QCD graphs.—For the QCD current at one loop we have vertex and wave function graphs. We use free quark external states with an off-shellness IR regulator, $\Delta^2 = p^2 - m^2 = \bar p^2 - m^2$ where $\Delta^2 \ll m^2$. We use dimensional regularization with $d = 4 - 2\epsilon$ for the UV divergences. The graphs in Fig. 4 are

$$\begin{aligned} V_{4a} &= \Gamma_i^\mu \frac{\alpha_s C_F}{4\pi}\Big(\frac{1}{\epsilon} + 2\ln^2\frac{-Q^2}{m^2} - 4\ln\frac{-Q^2}{m^2}\ln\frac{Q^2}{\Delta^2} \\ &\quad + 3\ln\frac{-Q^2}{m^2} + \ln\frac{\mu^2}{m^2} + \frac{2\pi^2}{3}\Big), \\ V_{4b} &= \frac{-i\alpha_s C_F}{4\pi}\Big[m\Big\{\frac{4}{\epsilon} + 4\ln\Big(\frac{\mu^2}{m^2}\Big) + 6 + \frac{4\Delta^2}{m^2}\ln\Big(\frac{m^2}{-\Delta^2}\Big)\Big\} \\ &\quad + \not p\Big\{\frac{-1}{\epsilon} - \ln\Big(\frac{\mu^2}{m^2}\Big) - 2 + \frac{\Delta^2}{m^2} + \frac{2\Delta^2}{m^2}\ln\Big(\frac{-\Delta^2}{m^2}\Big)\Big\}\Big]. \end{aligned} \tag{A1}$$

SCET vertex graphs.—For the SCET current we have collinear vertex and wave function graphs and a soft vertex graph. We use dimensional regularization for the UV divergences and the off-shellness IR regulators $\Delta^2 = p^2 - m^2$ and $\bar\Delta^2 = \bar p^2 - m^2$. To compare IR divergences to the full theory results we should set $\Delta^2 = \bar\Delta^2$ and expand in $\Delta^2 \ll m^2$. For later convenience we will first quote results prior to making this expansion. The massive collinear quark Lagrangian is given by [105,106]

$$\begin{aligned} \mathcal{L}_{qn}^{(0)} &= \bar\xi_n\Big[in\cdot D_s + gn\cdot A_n + (i\not D_c^\perp - m)W_n\frac{1}{\bar n\cdot\mathcal{P}} \\ &\quad \times W_n^\dagger(i\not D_c^\perp + m)\Big]\frac{\bar{\not n}}{2}\xi_n. \end{aligned} \tag{A2}$$

Using the corresponding massive SCET Feynman rules the graphs in Fig. 5 are given by Fig. 5$\{a, b, c\} = (\bar\xi_n\Gamma_i^\mu\xi_{\bar n})V_{5\{a,b,c\}}$ and Fig. 5$\{d, e\} = (\frac{-i\bar{\not n}}{2})V_{5\{d,e\}}$ where the intgerals $V_{5a,b,c,d,e}$ read

$$\begin{aligned} V_{5a} &= -2ig^2C_F\tilde\mu^{2\epsilon}\int\frac{d^dk}{(2\pi)^d}\Big\{\frac{\bar n\cdot(k+p)}{[\bar n\cdot k][k^2][(k+p)^2-m^2]} - \frac{\bar n\cdot p}{[\bar n\cdot k][k^2][\bar n\cdot pn\cdot(k+p)-m^2]}\Big\}, \\ V_{5b} &= V_{5a} \quad \text{with} \quad n\leftrightarrow\bar n,\, p\longrightarrow\bar p, \\ V_{5c} &= -2ig^2C_F\tilde\mu^{2\epsilon}\int\frac{d^dk}{(2\pi)^d}\frac{(\bar n\cdot p)(-n\cdot\bar p)}{[k^2][\bar n\cdot pn\cdot k+\Delta^2+i0][-n\cdot\bar p\,\bar n\cdot k+\bar\Delta^2]}, \\ V_{5d} &= -2g^2C_F\tilde\mu^{2\epsilon}\int\frac{d^dk}{(2\pi)^d}\frac{\bar n\cdot(k+p)}{[k^2][(k+p)^2-m^2]}\Big\{\frac{4m^2(1-\frac{\epsilon}{2})}{[\bar n\cdot p][\bar n\cdot(k+p)]} + \frac{(k_\perp^2-m^2)(1-\epsilon)}{[\bar n\cdot(k+p)]^2} - \frac{m^2(1-\epsilon)}{[\bar n\cdot p]^2}\Big\}, \\ V_{5e} &= 2g^2C_F\tilde\mu^{2\epsilon}\int\frac{d^dk}{(2\pi)^d}\frac{1}{[k^2]}\frac{(1-\epsilon)}{[\bar n\cdot(k+p)]}, \end{aligned} \tag{A3}$$

where

$$\tilde\mu^2 \equiv \frac{\mu^2 e^{\gamma_E}}{4\pi}, \tag{A4}$$

and where all terms in the denominator with square brackets are defined with the $+i0$ prescription. To evaluate Fig. 5(a) and 5(b) we included the zero-bin minimal subtraction [55] to avoid double-counting the region encoded in Fig. 5(c). For V_{5d} and V_{5e} we have a singularity for $\bar n\cdot(k+p)\longrightarrow 0$ with fixed $k_\perp^2$, but it cancels in the sum of the two diagrams:

$$V_{5d} + V_{5e} = -2g^2C_F\tilde\mu^{2\epsilon}\int\frac{d^dk}{(2\pi)^d}\frac{(1-\epsilon)}{[k^2][(k+p)^2-m^2]}\Big\{\frac{4m^2(1-\frac{\epsilon}{2})}{(1-\epsilon)[\bar n\cdot p]} - n\cdot(k+p) - \frac{m^2\bar n\cdot(k+p)}{[\bar n\cdot p]^2}\Big\}.$$

Setting $\bar n\cdot p = n\cdot\bar p = Q$ and computing the integrals we find

$$\begin{aligned}
V_{5a} &= \frac{\alpha_s C_F}{4\pi}\bigg[\frac{2}{\epsilon^2} + \frac{2}{\epsilon}\ln\Big(\frac{\mu^2}{-\Delta^2}\Big) + \frac{2}{\epsilon} + \ln^2\Big(\frac{\mu^2}{-\Delta^2}\Big) - \ln^2\Big(\frac{m^2}{-\Delta^2}\Big) - 2\mathrm{Li}_2\Big(\frac{-\Delta^2}{m^2}\Big) \\
&\quad + 2\ln\Big(\frac{m^2}{-\Delta^2}\Big)\ln\Big(\frac{m^2+\Delta^2}{-\Delta^2}\Big) + 2\ln\Big(\frac{\mu^2}{-\Delta^2}\Big) - \frac{2m^2}{m^2+\Delta^2}\ln\Big(\frac{m^2}{-\Delta^2}\Big) + 4 + \frac{\pi^2}{2}\bigg], \\
V_{5b} &= V_{5a}[\Delta^2 \to \bar{\Delta}^2], \\
V_{5c} &= \frac{\alpha_s C_F}{4\pi}\bigg[-\frac{2}{\epsilon^2} - \frac{2}{\epsilon}\ln\Big(\frac{Q^2\mu^2}{(-\Delta^2)\bar{\Delta}^2}\Big) - \ln^2\Big(\frac{Q^2\mu^2}{(-\Delta^2)\bar{\Delta}^2}\Big) - \frac{\pi^2}{2}\bigg], \\
V_{5d} + V_{5e} &= \frac{1}{Q}\frac{\alpha_s C_F}{4\pi}\bigg[\frac{6m^2-\Delta^2}{\epsilon} + (6m^2-\Delta^2)\ln\Big(\frac{\mu^2}{-\Delta^2}\Big) - \frac{m^4(6m^2+7\Delta^2)}{(m^2+\Delta^2)^2}\ln\Big(\frac{m^2}{-\Delta^2}\Big) + 8m^2 - \frac{\Delta^4}{m^2+\Delta^2}\bigg].
\end{aligned} \tag{A5}$$

Note that the soft graph, V_{5c}, , is independent of m. Expanding V_{5a} and $V_{5d} + V_{5e}$ for $\Delta^2 \ll m^2$ gives

$$\begin{aligned}
V_{5a} &= \frac{\alpha_s C_F}{4\pi}\bigg[\frac{2}{\epsilon^2} + \frac{2}{\epsilon}\ln\Big(\frac{\mu^2}{-\Delta^2}\Big) + \frac{2}{\epsilon} + \ln^2\Big(\frac{\mu^2}{-\Delta^2}\Big) + \ln^2\Big(\frac{m^2}{-\Delta^2}\Big) + 2\ln\Big(\frac{\mu^2}{m^2}\Big) + 4 + \frac{\pi^2}{2}\bigg], \\
V_{5d} + V_{5e} &= \frac{1}{Q}\frac{\alpha_s C_F}{4\pi}\bigg[m^2\Big\{\frac{6}{\epsilon} + 6\ln\Big(\frac{\mu^2}{m^2}\Big) + 8\Big\} - \Delta^2\Big\{\frac{1}{\epsilon} + \ln\Big(\frac{\mu^2}{m^2}\Big) + 4\ln\Big(\frac{-\Delta^2}{m^2}\Big)\Big\}\bigg].
\end{aligned} \tag{A6}$$

From Eq. (A2) with Eq. (51) we have a mass counterterm, $-i\bar{n}\!\!\!/ /(2\bar{n}\cdot p)2m\delta_m$. In the pole-mass scheme

$$(\delta_m)^{\rm pole} = -m\frac{\alpha_s C_F}{4\pi}\bigg[\frac{3}{\epsilon} + 3\ln\frac{\mu^2}{m^2} + 4\bigg], \tag{A7}$$

which exactly cancels the entire m^2 term in the self-energy graphs $V_{5d} + V_{5e}$. In a general mass scheme we have $\delta_m = (\delta_m)^{\rm pole} + \delta m$, and

$$\begin{aligned}
V_{5d} + V_{5e} + \frac{2m}{\bar{n}\cdot p}\delta_m &= \frac{2m\delta m}{Q} - \frac{\Delta^2}{Q}\frac{\alpha_s C_F}{4\pi} \\
&\quad \times \Big\{\frac{1}{\epsilon} + \ln\Big(\frac{\mu^2}{m^2}\Big) + 4\ln\Big(\frac{-\Delta^2}{m^2}\Big)\Big\}.
\end{aligned} \tag{A8}$$

Using the $\overline{\rm MS}$ subtraction, the wave function renormalization Z_ξ removes the remaining $1/\epsilon$ divergence in Eq. (A8), and leaves a finite correction to the residue of the collinear quark propagator, $iR_\xi(n\!\!\!/ /2)\bar{n}\cdot p/(p^2 - m^2)$, with

$$\begin{aligned}
Z_\xi &= 1 - \frac{\alpha_s C_F}{4\pi\epsilon}, \\
R_\xi &= 1 + \frac{\alpha_s C_F}{4\pi}\bigg[-\ln\Big(\frac{\mu^2}{m^2}\Big) - 4\ln\Big(\frac{-\Delta^2}{m^2}\Big)\bigg].
\end{aligned} \tag{A9}$$

This is identical to results from the QCD self-energy, $V_{(4b)}$ in Eq. (A1), namely $R_\psi = R_\xi$ and $Z_\psi = Z_\xi$.

SCET jet function.—The computation of the stable massive SCET jet function is given by the imaginary part of the graphs in Fig. 6. The integrals are identical to those for the vertex graphs above, except that now there is true external momentum, r_n^μ, that is routed through the diagram, and the invariant mass s takes the place of the offshellness, therefore these diagrams do not require an IR regulator. Here $s = r_n^2 - m^2 = Qr_n^+ - m^2$ is defined for convenience. The diagrams in Fig. 6 contribute to the SCET jet functions. Taking the spin and color trace, but not yet the imaginary part, the graphs give

$$\begin{aligned}
J_{6a} = J_{6b} &= \bigg[\frac{i}{\pi}\frac{i}{s+i0}\bigg]V_{5a}(\Delta^2 \to s) \\
&= \frac{-\alpha_s C_F}{4\pi^2 s}\bigg\{\frac{2}{\epsilon^2} + \frac{2}{\epsilon}\ln\Big(\frac{\mu^2}{-s}\Big) + \frac{2}{\epsilon} + \ln^2\Big(\frac{\mu^2}{-s}\Big) - \ln^2\Big(\frac{m^2}{-s}\Big) - 2\mathrm{Li}_2\Big(\frac{-s}{m^2}\Big) + 2\ln\Big(\frac{m^2}{-s}\Big)\ln\Big(\frac{m^2+s}{-s}\Big) \\
&\quad + 2\ln\Big(\frac{\mu^2}{-s}\Big) - \frac{2m^2}{m^2+s}\ln\Big(\frac{m^2}{-s}\Big) + 4 + \frac{\pi^2}{2}\bigg\}, \\
J_{6c} &= 0, \\
J_{6d} + J_{6e} + J_{6f} &= \bigg[\frac{i}{\pi}\frac{(iQ)}{(s+i0)^2}\bigg]\bigg[V_{5d}(\Delta^2 \to s) + V_{5e}(\Delta^2 \to s) + \frac{2m}{Q}\delta m\bigg] \\
&= \frac{-2m\delta m}{\pi s^2} + \frac{\alpha_s C_F}{4\pi^2 s}\bigg\{\frac{1}{\epsilon} + \ln\Big(\frac{\mu^2}{-s}\Big) - \frac{m^2(5m^2+6s)}{(m^2+s)^2}\ln\Big(\frac{m^2}{-s}\Big) + \frac{s}{m^2+s}\bigg\},
\end{aligned} \tag{A10}$$

where $1/\epsilon$ terms are UV divergences and all s factors are $s + i0$. An internal Z_ψ counterterm is not needed since these factors cancel between the propagator and vertices. The sum of the terms in Eq. (A10) is quoted as Eq. (99) in the text. Expanding Eq. (A10) to leading order in $s/m^2 \ll 1$ gives

$$\begin{aligned} J_{6a} = J_{6b} &= \frac{-\alpha_s C_F}{4\pi^2 s}\left\{\frac{2}{\epsilon^2} + \frac{2}{\epsilon}\ln\left(\frac{\mu^2}{-s}\right) + \frac{2}{\epsilon} + \ln^2\left(\frac{\mu^2}{-s}\right) + \ln^2\left(\frac{m^2}{-s}\right) + 2\ln\left(\frac{\mu^2}{m^2}\right) + 4 + \frac{\pi^2}{2}\right\}, \\ J_{6d} + J_{6e} + J_{6f} &= \frac{-2m\delta m}{\pi s^2} + \frac{\alpha_s C_F}{4\pi^2 s}\left\{\frac{1}{\epsilon} + \ln\left(\frac{\mu^2}{m^2}\right) + 4\ln\left(\frac{-s}{m^2}\right)\right\}, \end{aligned} \tag{A11}$$

and the sum of these five terms gives Eq. (100).

Soft-function graphs.—Next we summarize the computation of the hemisphere soft function at one loop given by the graphs in Fig. 7. We use dimensional regularization for both UV and IR divergences. For Fig. 7a and 7b we have a loop integral, and for Fig. 7c and 7d a phase space integral:

$$\begin{aligned} S_{7a} &= \frac{-2ig^2 C_F\tilde{\mu}^{2\epsilon}}{(2\pi)^d}\int d^d q\,\frac{\delta(\ell^+)\delta(\ell^-)}{(q^+ + i0)(q^- - i0)(q^2 + i0)}, \\ S_{7b} &= \frac{2ig^2 C_F\tilde{\mu}^{2\epsilon}}{(2\pi)^d}\int d^d q\,\frac{\delta(\ell^+)\delta(\ell^-)}{(q^+ - i0)(q^- + i0)(q^2 - i0)}, \\ S_{7c} &= \frac{-2g^2 C_F\tilde{\mu}^{2\epsilon}}{(2\pi)^{d-1}}\int \frac{d^{d-1}q}{(q^+ + q^-)}\,\frac{[\theta(q^- - q^+)\delta(\ell^+ - q^+)\delta(\ell^-) + \theta(q^+ - q^-)\delta(\ell^+)\delta(\ell^- - q^-)]}{(q^- + i0)(-q^+ + i0)}, \\ S_{7d} &= \frac{-2g^2 C_F\tilde{\mu}^{2\epsilon}}{(2\pi)^{d-1}}\int \frac{d^{d-1}q}{(q^+ + q^-)}\,\frac{[\theta(q^- - q^+)\delta(\ell^+ - q^+)\delta(\ell^-) + \theta(q^+ - q^-)\delta(\ell^+)\delta(\ell^- - q^-)]}{(q^+ + i0)(-q^- + i0)}, \\ S_{7e} &= S_{7f} = S_{7g} = 0. \end{aligned} \tag{A12}$$

Here S_{7a} and S_{7b} are scaleless and convert IR divergences in $S_{7c,d}$ into UV divergences (see for instance Ref. [76] where this is worked out explicitly in several cases). To integrate $S_{7c,d}$ we convert $d^{d-1}q = \pi^{1-\epsilon}/[2\Gamma(1-\epsilon)]dq^+dq^-(q^+q^-)^{-\epsilon}(q^+ + q^-)\theta(q^+)\theta(q^-)$. Evaluating the sum of diagrams we find

$$S_{7a} + \ldots + S_{7g} = \frac{C_F\alpha_s(\mu)}{\pi}\,\frac{\mu^{2\epsilon}(e^{\gamma_E})^\epsilon}{\epsilon\Gamma(1-\epsilon)}\left[\frac{\delta(\ell-)\theta(\ell^+)}{(\ell^+)^{1+2\epsilon}} + \frac{\delta(\ell^+)\theta(\ell^-)}{(\ell^-)^{1+2\epsilon}}\right]. \tag{A13}$$

This result is used in Eq. (108) of the text.

APPENDIX B: SUMMARY OF FEYNMAN DIAGRAMS IN BHQET

In this appendix we list results for the individual Feynman diagrams used in the body of the paper in Sec. V. The velocity four vector $v_\pm^\mu$ and the momentum fluctuation four vector $k_\pm^\mu$ for the top and antitop, respectively, are given by

$$v_+^\mu = \left(\frac{m}{Q}, \frac{Q}{m}, \mathbf{0}_\perp\right), \qquad k_+^\mu \sim \Gamma\left(\frac{m}{Q}, \frac{Q}{m}, 1\right), \qquad v_-^\mu = \left(\frac{Q}{m}, \frac{m}{Q}, \mathbf{0}_\perp\right), \qquad k_-^\mu \sim \Gamma\left(\frac{Q}{m}, \frac{m}{Q}, 1\right). \tag{B1}$$

The Feynman rules for boosted HQET are summarized in Fig. 22.

bHQET vertex graphs.—First we give the results for the bHQET vertex graphs of Fig. 8. These graphs are defined in terms of the integrals $V_{8a,b,c,d}$ as Fig. 8 $\kappa = V_{8\kappa}(\bar{h}_{v_+}\Gamma_i^\mu h_{v_-})$ for $\kappa = a, b, d$ and Fig. 8 $\tau = V_{8\tau}$ for $\tau = c, e, f$. The one-loop integrals are given by

$$\begin{aligned} V_{8a} &= -iC_F g^2\tilde{\mu}^{2\epsilon}\int\frac{d^dk}{(2\pi)^d}\left\{\frac{n\cdot v_-}{[n\cdot k][v_-\cdot(k + r_-)][k^2]} - \frac{n\cdot v_-}{[n\cdot k][\frac{1}{2}n\cdot v_-\bar{n}\cdot k + v_-\cdot r_-][k^2]}\right\}, \\ V_{8b} &= V_{8a} \quad \text{with} \quad (n\leftrightarrow\bar{n}, v_+\leftrightarrow v_-, r_-\leftrightarrow r_+), \qquad V_{8c} = -C_F g^2\tilde{\mu}^{2\epsilon}\int\frac{d^dk}{(2\pi)^d}\,\frac{v_\pm\cdot v_\pm}{[k^2][v_\pm\cdot(k + l_\pm)]}, \\ V_{8d} &= iC_F g^2\tilde{\mu}^{2\epsilon}\int\frac{d^dk}{(2\pi)^d}\,\frac{\bar{n}\cdot n}{[k^2][\frac{1}{2}\bar{n}\cdot v_+ n\cdot k + v_+\cdot r_+][\frac{1}{2}n\cdot v_-\bar{n}\cdot k + v_-\cdot r_-]}, \qquad V_{8e} = V_{8f} = 0, \end{aligned} \tag{B2}$$

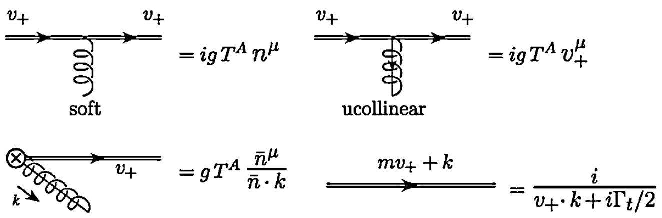

FIG. 22. bHQET Feynman rules for the top quarks annihilated by h_{v_+}: soft gluon coupling to the top quark, ucollinear gluon coupling to top quark, Wilson line ucollinear gluon coupling to the top quark, top propagator. Results for the antitop quarks annihilated by $\bar h_{v_-}$ are obtained by taking $v_+ \to v_-$, $T^A \to \bar T^A = -(T^A)^T$, and $n \leftrightarrow \bar n$.

where all the external legs are kept off shell by $(v_\pm \cdot r_\pm) \neq 0$ to regulate infrared divergences. As before, throughout this section all factors in the denominator with square brackets are defined with a $+i0$ prescription. Just as in SCET, the integrals $V_{8a,b}$ are defined with a zero-bin subtraction [55] in order to avoid double-counting the region encoded in the soft loop in Fig. 8(c). The loop momentum appearing in $V_{8a,b,d}$ has ultracollinear scaling as displayed in Eq. (B1). On the other hand, the loop momentum k in V_{8c} has a homogenous soft scaling corresponding to the exchange of a soft cross-talk gluon between the top and antitop sectors. Given homogenous scaling of the soft loop momentum and the collinear scaling of the velocity labels in Eq. (B1), at leading order we have the relations $v_+ \cdot k = \frac{1}{2}(\bar n \cdot v_+)(n \cdot k)$ and $v_- \cdot k = \frac{1}{2}(n \cdot v_-)(\bar n \cdot k)$ which have been used in V_{8c}. Using $v_\pm \cdot v_\pm = 1$, $\bar n \cdot n = 2$, $\bar n \cdot v_+ = n \cdot v_- = Q/m$ and setting $(2v_\pm \cdot r_\pm) = \Omega$ the integrals give:

$$\begin{aligned}
V_{8a} = V_{8b} &= \frac{\alpha_s C_F}{4\pi}\left[\frac{1}{\epsilon^2} + \frac{2}{\epsilon}\ln\left(\frac{\mu}{-\Omega}\right) + 2\ln^2\left(\frac{\mu}{-\Omega}\right) + \frac{5\pi^2}{12}\right],\\
V_{8c} &= -i\Omega\frac{\alpha_s C_F}{4\pi}\left[\frac{1}{\epsilon} + 2\ln\left(\frac{\mu}{-\Omega}\right) + 2\right],\\
V_{8d} &= \frac{\alpha_s C_F}{4\pi}\left[-\frac{2}{\epsilon^2} - \frac{2}{\epsilon}\ln\left(\frac{\mu^2 Q^2}{-\Omega^2 m^2}\right) - \ln^2\left(\frac{\mu^2 Q^2}{-\Omega^2 m^2}\right) - \frac{\pi^2}{2}\right].
\end{aligned} \tag{B3}$$

From V_{8c} for the wave function graph we get the $\overline{\text{MS}}$ wave function renormalization Z_h and the corresponding residue R_h as

$$Z_h = 1 + \frac{\alpha_s C_F}{2\pi\epsilon}, \qquad R_h = 1 + \frac{\alpha_s C_F}{4\pi}\left[4\ln\left(\frac{\mu}{-\Omega}\right) + 4\right]. \tag{B4}$$

These results are used to obtain Eq. (128) in the text.

bHQET jet function.—Next consider the graphs for the stable bHQET jet functions in Fig. 9. Prior to taking the imaginary part they are

$$\begin{aligned}
B_{9a}^{\Gamma=0}(\hat s) &= B_{9b}^{\Gamma=0}(\hat s) = -\frac{1}{\pi m \hat s}V_{8a}(\Omega \to \hat s),\\
B_{9c}^{\Gamma=0}(\hat s) &= 0, \qquad B_{9d}^{\Gamma=0}(\hat s) = \frac{-2i}{\pi m \hat s^2}V_{8c}(\Omega \to \hat s),\\
B_{9e}^{\Gamma=0}(\hat s) &= -\frac{1}{\pi m}\frac{2\delta m}{\hat s^2}.
\end{aligned} \tag{B5}$$

From Eqs. (B5) and (B3) we get

$$\begin{aligned}
B_{9a}^{\Gamma=0}(\hat s) &= B_{9b}^{\Gamma=0}(\hat s)\\
&= -\frac{1}{\pi m \hat s}\frac{\alpha_s C_F}{4\pi}\left[\frac{1}{\epsilon^2} + \frac{2}{\epsilon}\ln\left(\frac{\mu}{-\hat s}\right) + 2\ln^2\left(\frac{\mu}{-\hat s}\right) + \frac{5\pi^2}{12}\right],\\
B_{9d}^{\Gamma=0}(\hat s) &= -\frac{1}{\pi m\, \hat s}\frac{\alpha_s C_F}{4\pi}\left[\frac{2}{\epsilon} + 4\ln\left(\frac{\mu}{-\hat s}\right) + 4\right],
\end{aligned} \tag{B6}$$

where $\hat s = \hat s + i0$. Adding together $B_{9a}^{\Gamma=0}(\hat s), \ldots, B_{9e}^{\Gamma=0}(\hat s)$ we arrive at Eq. (138) in the main body of the paper.

Zero-bin subtraction for the bHQET jet function.—The $1/\epsilon$ singularities in Eq. (B6) are UV divergences. This is ensured by the zero-bin subtraction [55] for the graphs $B_{9a,b}^{\Gamma=0}$ that are needed to avoid double-counting with infrared regions already accounted for by the soft function (or the contributions in the soft loop in V_{8c}). Using dimensional regularization to regularize UV and IR divergences in Eqs. (B2) this may not be obvious since in this case the zero-bin subtraction is associated to scaleless integrals. To illustrate the role of the zero-bin subtraction more explicitly we reconsider the calculation of the antitop jet function $B_{9a}^{\Gamma=0}$ with a different IR regulator. From the definition of $B_+^{\Gamma=0}$ in the effective theory this computation involves two terms, the naive loop integrand $\tilde B_{9a}^{\Gamma=0}$ and a term induced by the zero-bin subtraction on propagators $B_{9a(0)}^{\Gamma=0}$. We use an explicit ρ-term to regulate the soft and collinear IR divergences for $n \cdot k = k^+ \to 0$. For the naive part of the result we have

$$\begin{aligned}
\tilde B_{9a}^{\Gamma=0} &= \frac{iC_F g^2 \tilde\mu^{2\epsilon}}{\pi m \hat s}\int\frac{d^d k}{(2\pi)^d}\frac{n \cdot v_-}{[n \cdot k - \rho][v_- \cdot (k + r_-)][k^2]}\\
&= -\frac{1}{\pi m \hat s}\frac{C_F g^2 \tilde\mu^{2\epsilon}}{4\pi}(4\pi)^\epsilon\Gamma(\epsilon)\left(\frac{\bar n \cdot v_-}{n \cdot v_-}\right)^{-\epsilon}\int_{-\infty}^0\frac{dk^+}{2\pi}\\
&\quad\times\frac{(k^+)^{-\epsilon}}{k^+ - \rho}\left(k^+ + \frac{\hat s}{\bar n \cdot v_-}\right)^{-\epsilon}.
\end{aligned} \tag{B7}$$

For the graph $B_{9a}^{\Gamma=0}$ the zero-bin subtraction is obtained from the fact that the collinear propagators act as distributions and induce a subtraction from the limit where $k^\mu \sim \Gamma\lambda^2$. Since this subtraction is obtained from the Feynman rules of the same diagram as Eq. (B7), it must have the same ρ-regulator for the $k^+ \to 0$ limit. For this subtraction part we obtain

$$\begin{aligned}\tilde{B}^{\Gamma=0}_{9a(0)} &= \frac{iC_F g^2 \tilde{\mu}^{2\epsilon}}{\pi m \hat{s}} \int \frac{d^d k}{(2\pi)^d} \\ &\quad \times \frac{n\cdot v_-}{[n\cdot k-\rho][\frac{1}{2} n\cdot v_- \bar{n}\cdot k + v_-\cdot r_-][k^2]} \\ &= -\frac{1}{\pi m\hat{s}} \frac{C_F g^2 \tilde{\mu}^{2\epsilon}}{4\pi} (4\pi)^\epsilon \Gamma(\epsilon) \Big(\frac{\hat{s}}{n\cdot v_-}\Big)^{-\epsilon} \\ &\quad \times \int_{-\infty}^{0} \frac{dk^+}{2\pi} \frac{(k^+)^{-\epsilon}}{k^+-\rho}. \end{aligned} \tag{B8}$$

The ρ term in Eqs. (B7) and (B8) regulates soft and collinear divergences, and these two results can be computed explicitly in terms of this regulator. However it drops out in the difference of Eqs. (B7) and (B8) which is IR finite:

$$\begin{aligned} B^{\Gamma=0}_{9a} &= \tilde{B}^{\Gamma=0}_{9a} - B^{\Gamma=0}_{9a(0)} \\ &= -\frac{1}{\pi m\hat{s}} \frac{C_F g^2 \tilde{\mu}^{2\epsilon}}{4\pi} (4\pi)^\epsilon \Gamma(\epsilon) \Big(\frac{\bar{n}\cdot v_-}{n\cdot v_-}\Big)^{-\epsilon} \int_{-\infty}^{0} \frac{dk^+}{2\pi} \\ &\quad \times \frac{(k^+)^{-\epsilon}}{k^+-\rho} \bigg[\Big(k^+ + \frac{\hat{s}}{\bar{n}\cdot v_-}\Big)^{-\epsilon} - \Big(\frac{\hat{s}}{\bar{n}\cdot v_-}\Big)^{-\epsilon}\bigg]. \end{aligned} \tag{B9}$$

For $k^+ \to 0$ the term in the brackets is linear in k^+ and the ρ-term can be dropped since the expression does not contain any IR divergences. Evaluating Eq. (B9) we recover the result shown in Eq. (B6). Thus all $1/\epsilon$ singularities are indeed UV divergences.

APPENDIX C: PLUS FUNCTION AND IMAGINARY PART IDENTITIES

The plus function with an arbitrary exponent $1+\omega$ with $\omega<1$ is defined by

$$\bigg[\frac{\theta(x)}{(x)^{1+\omega}}\bigg]_+ = \lim_{\beta\to 0}\bigg[\frac{\theta(x-\beta)}{(x)^{1+\omega}} - \delta(x-\beta)\frac{\beta^{-\omega}}{\omega}\bigg]. \tag{C1}$$

A more general definition for the distribution $[\theta(x)/x^{1+\omega}]_+$ can be defined, by first integrating $\theta(x)/x^{1+\omega}$ with a test function for values of ω where the integrals converge, and then analytically continuing the result to other values of ω. Expanding Eq. (C1) for small ω gives the definition for the $\log^n(x)/x$ plus functions for $n\geq 0$:

$$\bigg[\frac{\theta(x)\ln^n x}{x}\bigg]_+ \equiv \lim_{\beta\to 0}\bigg[\frac{\theta(x-\beta)\ln^n x}{x} + \delta(x-\beta)\frac{\ln^{n+1}\beta}{n+1}\bigg]. \tag{C2}$$

The following rescaling identity for a dimensionless constant κ is also quite useful:

$$\begin{aligned}\kappa\bigg[\frac{\theta(x)\ln^n(\kappa x)}{\kappa x}\bigg]_+ &= \frac{\ln^{n+1}(\kappa)}{n+1}\delta(x) + \sum_{k=0}^{n}\frac{n!}{(n-k)!k!} \\ &\quad \times \ln^{n-k}(\kappa)\bigg[\frac{\theta(x)\ln^k(x)}{x}\bigg]_+. \end{aligned} \tag{C3}$$

For example, for integrations over a finite range Eq. (C3) allows us to rescale the + function to act only within the interval [0, 1], where standard identities such as $\int_0^1 dx' g(x')[\theta(x')/x']_+ = \int_0^1 dx'[g(x')-g(0)]/x'$ for a given test function g can then be applied. This is somewhat simpler than the corresponding general relation $\int_0^\beta dx' g(x')[\theta(x')/x']_+ = \int_0^\beta dx'[g(x')-g(0)]/x' + g(0)\ln(\beta)$. Relation (C3) has also been used to verify the multiplicative form of the consistency conditions in Eqs. (121) and (150).

In computing the SCET and bHQET jet functions one has to take the imaginary part of the forward scattering graphs. For this the following result for a dimensionless variable x is quite useful

$$\begin{aligned}\mathrm{Im}\bigg[\frac{\ln^n(-x-i0)}{\pi(-x-i0)}\bigg] &= \cos^2\Big(\frac{n\pi}{2}\Big)\frac{(-\pi^2)^{n/2}}{n+1}\delta(x) \\ &\quad + \sum_{j=0}^{[(n-1)/2]}\frac{(-1)^j n!\pi^{2j}}{(2j+1)!(n-2j-1)!} \\ &\quad \times \bigg[\frac{\theta(x)\ln^{n-2j-1}(x)}{x}\bigg]_+, \end{aligned} \tag{C4}$$

where $[p]$ on the sum is the greatest integer not exceeding p, sometimes also called the Gauss bracket of p. For the first few orders this gives

$$\begin{aligned} \frac{1}{\pi}\,\mathrm{Im}\bigg[\frac{1}{x+i0}\bigg] &= -\delta(x), \\ \frac{1}{\pi}\,\mathrm{Im}\bigg[\frac{\ln(-x-i0)}{x+i0}\bigg] &= -\bigg[\frac{\theta(x)}{x}\bigg]_+, \\ \frac{1}{\pi}\,\mathrm{Im}\bigg[\frac{1}{(x+i0)^2}\bigg] &= \delta'(x), \\ \frac{1}{\pi}\,\mathrm{Im}\bigg[\frac{\ln^2(-x-i0)}{x+i0}\bigg] &= \frac{\pi^2}{3}\delta(x) - 2\bigg[\frac{\theta(x)\ln(x)}{x}\bigg]_+. \end{aligned} \tag{C5}$$

To compute the massive SCET jet function in Eq. (101) the following identities were also used [with $s = s + i0 = x\kappa_1^2 + i0$]:

$$
\begin{aligned}
\frac{1}{\pi}\,\mathrm{Im}\Big\{\frac{1}{s}\,\mathrm{Li}_2\Big(\frac{-s}{m^2}\Big)\Big\} &= -\frac{1}{s}\ln\Big(\frac{-s}{m^2}\Big)\theta(-m^2-s),\\
\frac{1}{\pi}\,\mathrm{Im}\Big\{\frac{1}{s}\ln\Big(\frac{m^2}{-s}\Big)\ln\Big(1+\frac{s}{m^2}\Big)\Big\} &= \frac{1}{s}\ln\Big(\frac{m^2}{-s}\Big)\theta(-m^2-s)+\frac{1}{\kappa_1^2}\Big[\frac{\theta(x)}{x}\Big]_+\ln\Big(1+\frac{s}{m^2}\Big),\\
\frac{1}{\pi}\,\mathrm{Im}\Big\{\frac{m^2(m^2+2s)}{s(s+m^2)^2}\ln\Big(\frac{m^2}{-s}\Big)\Big\} &= -\delta(s)\ln\Big(\frac{m^2}{\kappa_1^2}\Big)+\frac{1}{\kappa_1^2}\Big[\frac{\theta(x)}{x}\Big]_+-\frac{\theta(s)s}{(s+m^2)^2}+m^2\ln\Big(\frac{m^2}{-s}\Big)\delta'(s+m^2).
\end{aligned}
\tag{C6}
$$

APPENDIX D: GENERAL RGE WITH PLUS AND DELTA FUNCTIONS

In this appendix we solve the general anomalous dimension equation

$$
\mu\frac{d}{d\mu}F(t,\mu)=\int_{-\infty}^{+\infty}dt'\gamma_F(t-t',\mu)F(t',\mu),
\tag{D1}
$$

where t and t' are variables of mass dimension j, and $\gamma_F(t-t')$ involves a + function and δ function. To motivate the general form for γ we consider a generic one-loop amplitude which has the form

$$
\begin{aligned}
A^{\mathrm{bare}}(t)&=\frac{1}{t+i0}+\frac{\alpha_s(\mu)}{4\pi}\frac{1}{t+i0}\Big(\frac{\mu^j}{-t-i0}\Big)^{2\epsilon/j}\\
&\quad\times\Big(\frac{\Gamma_0}{2\epsilon^2}+\frac{\gamma_0}{2\epsilon}+\ldots\Big).
\end{aligned}
\tag{D2}
$$

At one loop the imaginary part of A^{bare} is renormalized by the ultraviolet Z-factor

$$
\begin{aligned}
Z(t-t')&=\delta(t-t')+\frac{\alpha_s(\mu)}{4\pi}\Big\{\delta(t-t')\Big[\frac{\Gamma_0}{2\epsilon^2}+\frac{\Gamma_0}{2\epsilon}\ln\Big(\frac{\mu^2}{\kappa^2}\Big)\\
&\quad+\frac{\gamma_0}{2\epsilon}\Big]-\frac{\Gamma_0}{j\kappa^j\epsilon}\Big[\frac{\kappa^j\theta(t-t')}{t-t'}\Big]_+\Big\},
\end{aligned}
\tag{D3}
$$

where the numerical coefficients Γ_0 and γ_0 are the first terms in the perturbative series for the anomalous dimensions

$$
\begin{aligned}
\Gamma[\alpha_s]&=\frac{\alpha_s(\mu)}{4\pi}\Gamma_0+\Big[\frac{\alpha_s(\mu)}{4\pi}\Big]^2\Gamma_1+\ldots,\\
\gamma[\alpha_s]&=\frac{\alpha_s(\mu)}{4\pi}\gamma_0+\Big[\frac{\alpha_s(\mu)}{4\pi}\Big]^2\gamma_1+\ldots
\end{aligned}
\tag{D4}
$$

At any order in α_s the anomalous dimension to be used in Eq. (D1) is

$$
\begin{aligned}
\gamma_F(t-t',\mu)&=-\frac{2\Gamma[\alpha_s]}{j\mu^j}\Big[\frac{\mu^j\theta(t-t')}{t-t'}\Big]_+\\
&\quad+\gamma[\alpha_s]\delta(t-t')\\
&=-2\Gamma[\alpha_s]\Big\{\frac{1}{j\kappa^j}\Big[\frac{\kappa^j\theta(t-t')}{t-t'}\Big]_+\\
&\quad-\delta(t-t')\ln\Big(\frac{\mu}{\kappa}\Big)\Big\}+\gamma[\alpha_s]\delta(t-t'),
\end{aligned}
\tag{D5}
$$

and depends on the dimension j, $t-t'$, and μ. For convenience we introduced in Eq. (D5) the mass scale $\kappa>0$ so that the plus function has the dimensionless variables t/κ^j and t'/κ^j. But note that $\gamma_F(t-t',\mu)$ is independent of the choice of κ. Here $\Gamma[\alpha_s]$ and $\gamma[\alpha_s]$ are perturbative series in $\alpha_s(\mu)$ which start with a linear term as shown in Eq. (D4).

To solve Eq. (D5) we use the Fourier transform method of Refs. [43,107], including the improvements of Ref. [108] which gives formulas that apply to all orders in perturbation theory. Our computation is a simple generalization of these solutions to mass dimension j variables, which as we will see is key to understanding how the renormalization-group evolutions of the soft function and the jet functions can combine to give local running. Taking a Fourier transform, $\gamma(y)=\int dt\exp(-ity)\gamma(t)$ and $F(y)=\int dt\exp(-ity)F(t)$ we have a simple multiplicative RGE

$$
\begin{aligned}
\mu\frac{d}{d\mu}F(y,\mu)&=\gamma_F(y,\mu)F(y,\mu),\\
\gamma_F(y,\mu)&=\frac{2\Gamma[\alpha_s]}{j}\ln(iy\mu^j e^{\gamma_E})+\gamma[\alpha_s],
\end{aligned}
\tag{D6}
$$

where $y=y-i0$. Note that the form of the position space anomalous dimension in Eq. (D6) simply follows from locality applied to the bilocal vacuum matrix element defining the jet function in position space. When translated to momentum space this directly implies the convolution structure shown in Eqs. (57) and (67). Integrating Eq. (D6) from μ_0 to μ by changing variables to α_s with $d\ln\mu=d\alpha_s/\beta[\alpha_s]$ gives the solution

$$
\ln\Big[\frac{F(y,\mu)}{F(y,\mu_0)}\Big]=\tilde{\omega}(\mu,\mu_0)\ln(iy\mu_0^j e^{\gamma_E})+\tilde{K}(\mu,\mu_0),
\tag{D7}
$$

where

$$
\begin{aligned}
\tilde{\omega}(\mu,\mu_0)&=\frac{2}{j}\int_{\alpha_s(\mu_0)}^{\alpha_s(\mu)}\frac{d\alpha}{\beta[\alpha]}\Gamma[\alpha],\\
\tilde{K}_\gamma(\mu,\mu_0)&=\int_{\alpha_s(\mu_0)}^{\alpha_s(\mu)}\frac{d\alpha}{\beta[\alpha]}\gamma[\alpha],\\
\tilde{K}(\mu,\mu_0)&=\tilde{K}_\gamma(\mu,\mu_0)+2\int_{\alpha_s(\mu_0)}^{\alpha_s(\mu)}\frac{d\alpha}{\beta[\alpha]}\Gamma[\alpha]\\
&\quad\times\int_{\alpha_s(\mu_0)}^{\alpha}\frac{d\alpha'}{\beta[\alpha']}.
\end{aligned}
\tag{D8}
$$

(Note that in the main body of this paper where we consider LL and NLL accuracy we write ω, K, and K_γ instead of $\tilde{\omega}$, $\tilde{K}$, and $\tilde{K}_\gamma$, respectively.) Thus the position space solution is $F(y, \mu) = \mathcal{U}(y, \mu, \mu_0)F(y, \mu_0)$ with

$$\mathcal{U}(y, \mu, \mu_0) = e^{\tilde{K}(\mu,\mu_0)}(iy\mu_0^j e^{\gamma_E})^{\tilde{\omega}(\mu,\mu_0)}. \tag{D9}$$

The desired solution is the inverse transform, $F(t, \mu) = 1/(2\pi)\int dy \exp(ity)F(y, \mu)$ so

$$F(t, \mu) = \frac{e^{\tilde{K}}}{2\pi}\int dy e^{ity}F(y, \mu_0)(iy\mu_0^j e^{\gamma_E})^{\tilde{\omega}}. \tag{D10}$$

To simplify this result we use $F(y, \mu_0) = \int dt' \exp(-it'y)F(t', \mu_0)$ and also the inverse transform

$$(iy\mu^j)^\omega = \frac{1}{\Gamma(-\omega)}\int dt' \exp(-it'y\mu^j)\left[\frac{\theta(t')}{(t')^{(1+\omega)}}\right]_+. \tag{D11}$$

Doing the integrals over y and t' we obtain the final result

$$F(t, \mu) = \int dt' U(t - t', \mu, \mu_0)F(t', \mu_0), \tag{D12}$$

where the evolution kernel is

$$U(t - t', \mu, \mu_0) = \frac{e^{\tilde{K}}(e^{\gamma_E})^{\tilde{\omega}}}{\mu_0^j\Gamma(-\tilde{\omega})}\left[\frac{(\mu_0^j)^{1+\tilde{\omega}}\theta(t - t')}{(t - t')^{1+\tilde{\omega}}}\right]_+. \tag{D13}$$

This + function is defined by Eq. (C1) and $\tilde{K}$ and $\tilde{\omega}$ are determined at whatever order one desires from Eq. (D8). In Sec. III D we carry out these integrals with NLL accuracy. The above derivation also suffices to solve Eqs. (54) and (64) to obtain U_{H_Q} and U_{H_m}, respectively. First we note that $\gamma_{H_Q}(Q, \mu)$ has the same form as $\gamma_F(y, \mu)$ with $j = 2$ and $iye^{\gamma_E} \rightarrow 1/Q^2$, so the general solution is given by Eq. (D9) with the same substitutions, yielding the result in Eq. (79). For $\gamma_{H_m}(Q/m, \mu)$ the cusp angle is fixed at m^2/Q^2, so the solution is given by Eq. (D9) with $\Gamma[\alpha_s] \rightarrow 0$ and $\gamma[\alpha_s] \rightarrow \Gamma_{H_m}[\alpha_s]\ln(m^2/Q^2) + \gamma_{H_m}[\alpha_s]$. This yields U_{H_m} in Eq. (79).

For the cases with convolutions a few additional identities are useful. The evolution kernels obey

$$\begin{aligned}\int dr' U(r - r', \mu, \mu_I)U(r' - r'', \mu_I, \mu_0)\\ = U(r - r'', \mu, \mu_0),\end{aligned} \tag{D14}$$

which states that it is equivalent to evolve through an intermediate scale, $\mu_0 \rightarrow \mu_I \rightarrow \mu$, or directly from $\mu_0 \rightarrow \mu$. To verify Eq. (D14) one needs

$$\begin{aligned}&\int dr''\left[\frac{(\mu_I^j)^{1+\tilde{\omega}_1}\theta(r - r'')}{(r - r'')^{1+\tilde{\omega}_1}}\right]_+\left[\frac{(\mu_0^j)^{1+\tilde{\omega}_2}\theta(r'' - r')}{(r'' - r')^{1+\tilde{\omega}_2}}\right]_+\\ &\quad = \frac{\Gamma(-\tilde{\omega}_1)\Gamma(-\tilde{\omega}_2)}{(\mu_I^{-j})\Gamma(-\tilde{\omega}')}\left(\frac{\mu_I^j}{\mu_0^j}\right)^{\tilde{\omega}_1}\left[\frac{(\mu_0^j)^{1+\tilde{\omega}'}\theta(r - r')}{(r - r')^{1+\tilde{\omega}'}}\right]_+,\\ &\tilde{K}(\mu, \mu_I) + \tilde{K}(\mu_I, \mu_0) = \tilde{\omega}_1 \ln\left(\frac{\mu_0^j}{\mu_I^j}\right) + \tilde{K}(\mu, \mu_0),\end{aligned} \tag{D15}$$

where here $\tilde{\omega}_1 = \tilde{\omega}(\mu, \mu_I)$, $\tilde{\omega}_2 = \tilde{\omega}(\mu_I, \mu_0)$, and $\tilde{\omega}' = \tilde{\omega}(\mu, \mu_0) = \tilde{\omega}_1 + \tilde{\omega}_2$. The first result in Eq. (D15) is straightforward to derive using the Fourier transform. Another useful identity simplifies the convolution of two U's that have the same renormalization scales, but variables with different mass dimension, and different anomalous dimension coefficients

$$\begin{aligned}&\int dr' U(Q'(r - r'), \mu, \mu_0; j', \Gamma', \gamma', \tilde{\omega}_1)\\ &\quad \times U(r' - r'', \mu, \mu_0; j, \Gamma, \gamma, \tilde{\omega}_2)\\ &= \frac{1}{Q'}\left(\frac{(\mu_0)^{j'-j}}{Q'}\right)^{\tilde{\omega}_1} U(r - r'', \mu, \mu_0; j, \Gamma' + \Gamma, \gamma' + \gamma, \tilde{\omega}').\end{aligned} \tag{D16}$$

Here the variables after the semicolon denote parameter dependence, and Q' simply denotes a variable with mass dimension $j' - j$. Also here $\tilde{\omega}_1 = \tilde{\omega}(\mu, \mu_0; \Gamma'/j')$ and $\tilde{\omega}_2 = \tilde{\omega}(\mu, \mu_0; \Gamma/j)$ are simply the $\tilde{\omega}$'s obtained from the other parameters, but this is not the case for $\tilde{\omega}'$ in the U on the RHS where $\tilde{\omega}' \equiv \tilde{\omega}_1 + \tilde{\omega}_2$. The final useful identity is

$$\lim_{\tilde{\omega}' \rightarrow 0} U(r - r', \mu, \mu_0; j, \Gamma, \gamma, \tilde{\omega}') = e^{\tilde{K}(\mu,\mu_0;\Gamma,\gamma)}\delta(r - r'), \tag{D17}$$

which is easy to derive from Eqs. (C1) and (D13). Using Eqs. (D15) and (D16) it is a straightforward exercise to verify the consistency equations directly in the integral form given in Eqs. (71) and (77).

APPENDIX E: ANALYTIC RESULTS FOR $G_\pm$ IN THE PEAK AND TAIL CROSS SECTION

In this appendix we show how the functions $G_\pm$ defined in Eq. (184) can be determined analytically. As a first step we use Eqs. (115) and (142) with $\kappa_3 = \mu_\Gamma$ and $\kappa_2 = \mu_\Gamma m_J/Q$ to compute the ℓ' integral to $\mathcal{O}(\alpha_s)$ [recall $m_J = m_J(\mu_\Gamma)$]

$$\begin{aligned}E_{\pm}^{\Gamma=0}\Big(\hat{s},\frac{Q}{m_J},\mu_\Gamma,\mu_\Lambda\Big) &\equiv \int_{-\infty}^{+\infty} d\ell' B_{\pm}^{\Gamma=0}\Big(\hat{s}-\frac{Q}{m_J}\ell',\mu_\Gamma\Big)\tilde{S}^{\rm part}(\ell',\mu_\Lambda,\delta_1)\\ &= \frac{1}{\mu_\Gamma m_J}\bigg[\delta(z)+\frac{C_F\alpha_s(\mu_\Gamma)}{\pi}\bigg\{\Big(1-\frac{\pi^2}{8}\Big)\delta(z)+2\Big[\frac{\theta(z)\ln z}{z}\Big]_+ -\Big[\frac{\theta(z)}{z}\Big]_+\bigg\}\\ &\quad +\frac{C_F\alpha_s(\mu_\Lambda)}{\pi}\bigg\{\Big[\frac{\pi^2}{24}-\ln^2\Big(\frac{\mu_\Lambda Q}{\mu_\Gamma m_J}\Big)\Big]\delta(z)-2\Big[\frac{\theta(z)\ln z}{z}\Big]_+ +2\ln\Big(\frac{\mu_\Lambda Q}{\mu_\Gamma m_J}\Big)\Big[\frac{\theta(z)}{z}\Big]_+\bigg\}\\ &\quad -\Big[\frac{\delta_1(\mu_\Lambda)Q}{\mu_\Gamma m_J}+\frac{2\delta m_J(\mu_\Gamma)}{\mu_\Gamma}\Big]\delta'(z)\bigg], \end{aligned} \tag{E1}$$

where $z = \hat{s}/\mu_\Gamma$ and δ_1 is given in Eq. (175). The $\delta'(z)$ term in Eq. (E1) contains the residual mass correction δm_J for the jet-mass scheme in Eq. (161) and the subtraction δ_1 for the soft function from Eq. (175). Using the relations

$$\begin{aligned}\delta(z) &= -\frac{1}{\pi}\,{\rm Im}\Big[\frac{1}{z+i0}\Big], \qquad \Big(\frac{1}{z}\Big)_+ = -\frac{1}{\pi}\,{\rm Im}\Big[\frac{\ln(-z-i0)}{z+i0}\Big],\\ \Big[\frac{\ln z}{z}\Big]_+ &= -\frac{1}{\pi}\,{\rm Im}\Big[\frac{\ln^2(-z-i0)}{2(z+i0)}+\frac{\pi^2}{6}\frac{1}{z+i0}\Big], \qquad \delta'(z)=\frac{1}{\pi}\,{\rm Im}\Big[\frac{1}{(z+i0)^2}\Big],\end{aligned} \tag{E2}$$

the result for $E_\pm$ can be rewritten as

$$E_{\pm}^{\Gamma=0}\Big(\hat{s},\frac{Q}{m_J(\mu_\Gamma)},\mu_\Gamma,\mu_\Lambda\Big) = {\rm Im}\Big[\mathcal{E}_{\pm}^{\Gamma=0}\Big(\hat{s},\frac{Q}{m_J(\mu_\Gamma)},\mu_\Gamma,\mu_\Lambda\Big)\Big], \tag{E3}$$

with

$$\begin{aligned}\mathcal{E}_{\pm}^{\Gamma=0}\Big(\hat{s},\frac{Q}{m_J},\mu_\Gamma,\mu_\Lambda\Big) &= \frac{-1}{\pi m_J}\frac{1}{\hat{s}+i0}\bigg\{1+\frac{1}{\hat{s}+i0}\Big[2\delta m_J(\mu_\Gamma)+\frac{Q}{m_J}\delta_1(\mu_\Lambda)\Big]+\frac{C_F\alpha_s(\mu_\Gamma)}{\pi}\Big[1+\frac{5\pi^2}{24}+\ln^2\Big(\frac{-\hat{s}-i0}{\mu_\Gamma}\Big)\\ &\quad -\ln\Big(\frac{-\hat{s}-i0}{\mu_\Gamma}\Big)\Big]+\frac{C_F\alpha_s(\mu_\Lambda)}{\pi}\Big[-\frac{7\pi^2}{24}-\ln^2\Big(\frac{\mu_\Lambda Q}{\mu_\Gamma m_J}\Big)-\ln^2\Big(\frac{-\hat{s}-i0}{\mu_\Gamma}\Big)\\ &\quad +2\ln\Big(\frac{\mu_\Lambda Q}{\mu_\Gamma m_J}\Big)\ln\Big(\frac{-\hat{s}-i0}{\mu_\Gamma}\Big)\Big]\bigg\}.\end{aligned} \tag{E4}$$

Note that for $\mu_\Lambda \gtrsim \Lambda$ and $\mu_\Gamma \sim \hat{s} \sim \Gamma \sim Q\Lambda/m$ there are no large logs in this expression, and that the terms with δm_J and δ_1 are the same order in the power counting. Given Eq. (E4), doing the second integral in the variable $\hat{s}''$ involving the Breit-Wigner function is simple since it just results in a shift of the invariant mass variable into the positive complex plane, as in Eq. (37):

$$\int_{-\infty}^{+\infty} d\hat{s}'' E_{\pm}^{\Gamma=0}\Big(\hat{s}-\hat{s}'',\frac{Q}{m_J},\mu_\Gamma,\mu_\Lambda\Big)\frac{\Gamma_t}{\pi(\hat{s}''^2+\Gamma_t^2)} = {\rm Im}\Big[\mathcal{E}_{\pm}^{\Gamma=0}\Big(\hat{s}+i\Gamma_t,\frac{Q}{m_J},\mu_\Gamma,\mu_\Lambda\Big)\Big] = E_\pm\Big(\hat{s},\frac{Q}{m_J},\Gamma_t,\mu_\Gamma,\mu_\Lambda\Big). \tag{E5}$$

For the final integration in the variable $\hat{s}'$ in Eq. (184) we have to convolute the finite width version of the terms in Eq. (E4) with the evolution kernel U_B. The relevant computations read

$$\int_{-\infty}^{+\infty} d\hat{s}' U_B(\hat{s}-\hat{s}',\mu_\Lambda,\mu_\Gamma)\frac{\ln^n(\frac{-\hat{s}'-i\Gamma_t}{\mu_\Gamma})}{\hat{s}'+i\Gamma_t} \equiv -G_n(\hat{s},\Gamma_t,\mu_\Lambda,\mu_\Gamma), \tag{E6}$$

where

$$G_n(\hat{s},\Gamma_t,\mu,\mu_0) = \frac{e^{K_3}(\mu_0 e^{\gamma_E})^{\omega_1}\Gamma(1+\omega_1)}{(-\hat{s}-i\Gamma_t)^{1+\omega_1}} I_n\Big(\frac{\hat{s}+i\Gamma}{\mu_0},\omega_1\Big), \tag{E7}$$

with $K_3 = K_3(\mu,\mu_0)$ and $\omega_1 = \omega_1(\mu,\mu_0)$ given in Eqs. (147), and

$$I_n(x,\omega) = \frac{d^n}{d\epsilon^n}\frac{\Gamma(1-\epsilon+\omega)}{\Gamma(1-\epsilon)\Gamma(1+\omega)}(-x-i0)^{\epsilon}\big|_{\epsilon=0}. \tag{E8}$$

For the terms we need

$$\begin{aligned} I_0(x,\omega) &= 1, \qquad I_1(x,\omega) = \ln(-x-i0)-H(\omega),\\ I_2(x,\omega) &= [H(\omega)-\ln(-x-i0)]^2-\zeta_2+\Psi'(1+\omega).\end{aligned} \tag{E9}$$

Here $H(\omega)$ is the harmonic number function and $\Psi'(z) = d/dz[\Gamma'(z)/\Gamma(z)]$ is the derivative of the polygamma function. Thus the final result for the function $G_\pm$ is [$m_J = m_J(\mu_\Gamma)$]

$$G_\pm\left(\hat{s},\frac{Q}{m_J},\Gamma_t,\mu_\Lambda\right)=\mathrm{Im}\left[\mathcal{G}_\pm\left(\hat{s},\frac{Q}{m_J},\Gamma_t,\mu_\Gamma,\mu_\Lambda\right)+\delta\mathcal{G}_\pm\left(\hat{s},\frac{Q}{m_J},\Gamma_t,\mu_\Gamma,\mu_\Lambda\right)\right],\tag{E10}$$

where taking $G_i=G_i(\hat{s},\Gamma_t,\mu_\Lambda,\mu_\Gamma)$ we have

$$\begin{aligned}\mathcal{G}_\pm\left(\hat{s},\frac{Q}{m_J},\Gamma_t,\mu_\Gamma,\mu_\Lambda\right)&=\frac{1}{\pi m_J}\left\{G_0+\frac{C_F\alpha_s(\mu_\Gamma)}{\pi}\left[G_2-G_1+\left(1+\frac{5\pi^2}{24}\right)G_0\right]\right.\\&\quad\left.+\frac{C_F\alpha_s(\mu_\Lambda)}{\pi}\left[-G_2+2\ln\left(\frac{\mu_\Lambda Q}{\mu_\Gamma m_J}\right)G_1-\left(\frac{7\pi^2}{24}+\ln^2\left(\frac{\mu_\Lambda Q}{\mu_\Gamma m_J}\right)\right)G_0\right]\right\},\\\delta\mathcal{G}_\pm\left(\hat{s},\frac{Q}{m_J},\Gamma_t,\mu_\Gamma,\mu_\Lambda\right)&=-\frac{1}{\pi m_J}\left[\frac{Q}{m_J}\delta_1(\mu_\Lambda)+2\delta m_J(\mu_\Gamma)\right]\frac{d}{d\hat{s}}G_0.\end{aligned}\tag{E11}$$

APPENDIX F: CROSS SECTION IN THE ULTRA-TAIL REGION

In the text we presented results for the cross section in the peak and tail regions, where we assume $Q\gg m\gg\hat{s}$ and $m\gg\Gamma$. In this section we analyze the cross section for $Q\gg m\sim\hat{s}$, so that $\hat{s}$ is far above the peak region. This corresponds to $|M_{t,\bar{t}}-m_J|\sim m$, where the top-antitop jet invariant mass double differential distribution can be described by the SCET factorization formula of Eq. (13). Writing this cross section in an analogous form to Eq. (180) $[m_J=m_J(\mu_m)]$ we have

$$\frac{d^2\sigma}{dM_t dM_{\bar{t}}}=\frac{4M_tM_{\bar{t}}\sigma_0}{(m_J\Gamma_t)^2}F^{\mathrm{SCET}}(M_t,M_{\bar{t}},Q,m_J),\tag{F1}$$

where

$$\begin{aligned}&F^{\mathrm{SCET}}(M_t,M_{\bar{t}},Q,m_J)\\&\quad=(m_J\Gamma_t)^2H_Q(Q,\mu_m)\mathcal{M}(m_J,\mu_m)U_{H_Q}^{(5)}(Q,\mu_m,\mu_\Lambda)\\&\qquad\times\int_{-\infty}^{\infty}d\ell^+d\ell^-G_n(s_t-Q\ell^+,Q,m_J,\Gamma,\mu_\Lambda)\\&\qquad\times G_{\bar{n}}(s_{\bar{t}}-Q\ell^-,Q,m_J,\Gamma,\mu_\Lambda)S^{\mathrm{mod}}(\ell^+,\ell^-).\end{aligned}\tag{F2}$$

Note that Eqs. (F1) and (F2) are also appropriate for describing the massless limit $m_J\to0$ and the stable limit $\Gamma_t\to0$. To obtain this result we manipulated the first form given in Eq. (49). Here, S^{mod} is the hadronic model function given in Eq. (170), where we have suppressed its arguments a, b, Λ. The functions $G_{n,\bar{n}}$ can be written as

$$\begin{aligned}&G_{n,\bar{n}}(s,Q,m_J,\Gamma,\mu_\Lambda)\\&\equiv\int ds'ds''d\ell'U_J(s-s',\mu_\Lambda,\mu_m)\\&\quad\times J_{n,\bar{n}}(s'-s''-Q\ell',m_J,\mu_m)\tilde{S}^{\mathrm{part}}(\ell',\mu_\Lambda,\delta_1)\\&\quad\times\frac{m_J\Gamma}{\pi(s''^2+m_J^2\Gamma^2)}.\end{aligned}\tag{F3}$$

Here, $\tilde{S}^{\mathrm{part}}$ is the modified partonic soft function of Eqs. (115) and (179). For consistency with our peak cross section results we continue to use the jet-mass scheme, by taking δm_J for the δm term in Eq. (107). Since it does not require any technical effort, we include in $G_{n,\bar{n}}$ a constant width term for the top quark through the convolution involving the variable s''. We note, however, that away from the resonance region this width term leads to power-suppressed effects, and, moreover, does not provide a consistent description of the top-quark decay. It is nevertheless convenient to introduce the width term for practical purposes because it allows for an easy numerical evaluation of the SCET factorization theorem for all values of $M_{t,\bar{t}}$ without running into singularities for $M_{t,\bar{t}}$ close to the top-quark mass.

We can carry out an analytic calculation of the functions $G_{n,\bar{n}}$ defined in Eq. (F3). The calculation divides itself into two parts, the terms singular for $s_{t,\bar{t}}\to0$ which include the δ function and $+$ functions in Eq. (106), and the nonsingular θ-function term on the last line of Eq. (106). The final result in the jet-mass scheme reads $[m_J=m_J(\mu_m)]$

$$\begin{aligned}G_{n,\bar{n}}(s,Q,m_J,\Gamma_t,\mu_\Lambda)&=\mathrm{Im}[\mathcal{G}_{n,\bar{n}}(s,Q,m_J,\Gamma_t,\mu_m,\mu_\Lambda)\\&\quad+\delta\mathcal{G}_{n,\bar{n}}(s,Q,m_J,\Gamma_t,\mu_m,\mu_\Lambda)]\\&\quad+G_{n,\bar{n}}^{\mathrm{nonsing}}(s,Q,m_J,\mu_m).\end{aligned}\tag{F4}$$

For the singular terms, $\mathcal{G}_{n,\bar{n}}$ and $\delta\mathcal{G}_{n,\bar{n}}$, a computation can be carried out in close analogy to the computation of $G_\pm$ described in Appendix E. Taking the singular terms in Eq. (106) with $\kappa_1^2=\mu_m m_J$, and the results from

Eqs. (115) and (179) with $\kappa_2 = \mu_m m_J/Q$ we find

$$\begin{aligned}\mathcal{G}_{n,\bar n}(s, Q, m_J, \Gamma_t, \mu_m, \mu_\Lambda) &= \frac{1}{\pi}\bigg\{\tilde G_0 + \frac{C_F\alpha_s(\mu_m)}{\pi}\bigg[\tilde G_2 - \tilde G_1 + \bigg(\ln^2\frac{\mu_m}{m_J} + \frac{1}{2}\ln\frac{\mu_m}{m_J} + \frac{\pi^2}{4} + 2\bigg)\tilde G_0\bigg] \\ &\qquad + \frac{C_F\alpha_s(\mu_\Lambda)}{\pi}\bigg[-\tilde G_2 + 2\ln\bigg(\frac{\mu_\Lambda Q}{\mu_m m_J}\bigg)\tilde G_1 - \bigg(\frac{7\pi^2}{24} + \ln^2\bigg(\frac{\mu_\Lambda Q}{\mu_m m_J}\bigg)\bigg)\tilde G_0\bigg]\bigg\}, \\ \delta\mathcal{G}_{n,\bar n}(s, Q, m_J, \Gamma_t, \mu_m, \mu_\Lambda) &= -\frac{1}{\pi}[Q\delta_1(\mu_\Lambda) + 2m_J\delta m_J(\mu_m)]\frac{d}{ds}\tilde G_0,\end{aligned} \tag{F5}$$

with

$$\begin{aligned}\tilde G_n(s, Q, m_J, \Gamma_t, \mu_\Lambda, \mu_m) &\equiv -\int_{-\infty}^{+\infty} ds' U_J(s - s', \mu_\Lambda, \mu_m)\frac{\ln^n\big(\frac{-s'-im_J\Gamma_t}{\mu_m m_J}\big)}{s' + im_J\Gamma_t} = \frac{e^{K_1}(\mu_m^2 e^{\gamma_E})^{\omega_1}\Gamma(1+\omega_1)}{(-s - im_J\Gamma_t)^{1+\omega_1}} I_n\bigg(\frac{s + im_J\Gamma_t}{\mu_m m_J}, \omega_1\bigg) \\ &= \frac{1}{m_J}e^{K_1 - K_3}\bigg(\frac{\mu_m}{m_J}\bigg)^{\omega_1} G_n\bigg(\frac{s}{m}, \Gamma_t, \mu_\Lambda, \mu_m\bigg).\end{aligned} \tag{F6}$$

Here, $\omega_1 = \omega_1(\mu_\Lambda, \mu_m)$ and $K_1 = K_1(\mu_\Lambda, \mu_m)$ are given by Eq. (105) and the functions I_n were defined in Eq. (E8). The term $\delta\mathcal{G}_{n,\bar n}$ arises from the jet-mass definition (see Eq. (161)) and from the subtraction that we carry out for the soft-function model (see Eq. (175)).

For the nonsingular terms we note that the top-width effects represent $\mathcal{O}(\Gamma_t/m)$ power-suppressed terms for any $s \ll Q^2$. For instance, when $s \sim m^2$ the top width appears in the combination $s + im_J\Gamma_t$, and when $s \sim m\Gamma$ the entire nonsingular term is $\mathcal{O}(\Gamma_t/m)$. Thus it is consistent to neglect the top-quark width for the nonsingular terms. Setting $\Gamma_t = 0$ in Eq. (F3) and carrying out the s' and s'' integrals gives

$$\begin{aligned}G_{n,\bar n}^{\text{nonsing}}(s, Q, m_J, \mu_m, \mu_\Lambda) &= \frac{\alpha_s(\mu_m)C_F}{\pi m_J^2}\frac{\theta(s)e^{K_1}}{\Gamma(-\omega_1)}\bigg(\frac{\mu_m^2 e^{\gamma_E}}{s}\bigg)^{\omega_1}\bigg[\frac{1}{\omega_1}{}_3F_2\bigg(\{1, 1, 1\}, \{2, 1-\omega_1\}, \frac{-s}{m_J^2}\bigg) \\ &\qquad + \frac{sm_J^2}{4(1-\omega_1)(m_J^2 + s)^2}\bigg\{\frac{\omega_1^2 - 1}{\omega_1} + \bigg(\frac{s}{m_J^2} - \omega_1\bigg){}_2F_1\bigg(1, 1, 2-\omega_1, \frac{-s}{m_J^2}\bigg)\bigg\}\bigg].\end{aligned} \tag{F7}$$

APPENDIX G: ANALYTIC RESULTS FOR THE P_T FUNCTION FOR THRUST

In this appendix we derive an analytic result for P_T, the perturbative corrections appearing in the thrust cross section in Eq. (188). Starting from Eq. (189) for P_T with Eq. (183) for P the key is to simplify the integral over the product of G_+G_-,

$$\begin{aligned}G_\text{T}(\hat s) &\equiv \int_{-\infty}^{+\infty} d\hat s_d G_+\bigg(\frac{\hat s + \hat s_d}{2}, \frac{Q}{m_J}, \Gamma_t, \mu_\Lambda\bigg)G_-\bigg(\frac{\hat s + \hat s_d}{2}, \frac{Q}{m_J}, \Gamma_t, \mu_\Lambda\bigg) \\ &= \int d\hat s_s'\bigg[\int\frac{d\hat s_d}{2}U_B\bigg(\frac{\hat s - \hat s_s' - \hat s_d'}{2}, \mu_\Lambda, \mu_\Gamma\bigg)U_B\bigg(\frac{\hat s - \hat s_s' + \hat s_d'}{2}, \mu_\Lambda, \mu_\Gamma\bigg)\bigg] \\ &\quad \times \int d\hat s_s''\bigg[\int d\hat s_d'' E_+^{\Gamma=0}\bigg(\frac{\hat s_s' - \hat s_s'' - \hat s_d''}{2}\bigg)E_-^{\Gamma=0}\bigg(\frac{\hat s_s' - \hat s_s'' + \hat s_d''}{2}\bigg)\bigg]\bigg[\int\frac{d\hat s_d}{2}m_J^2 B_+^{\text{tree}}\bigg(\frac{\hat s_s'' + \hat s_d}{2}, \Gamma_t\bigg)B_-^{\text{tree}}\bigg(\frac{\hat s_s'' - \hat s_d}{2}, \Gamma_t\bigg)\bigg],\end{aligned} \tag{G1}$$

where $B_\pm^{\text{tree}}(\hat s, \Gamma_t)$ is simply a Breit-Wigner as shown in Eq. (28). This Breit-Wigner appears due to the factorization of lifetime effects in Sec. II B, and the perturbative corrections to the jet functions are part of $E_\pm^{\Gamma=0}$.

Here we rewrote the original integrations over symmetric variables ($\hat s_s$'s) and antisymmetric variables ($\hat s_d$'s). Each of the integrations in square brackets can be performed, with the help of Eqs. (D16) and (E1), to give the terms in the following result

$$G_\text{T}(\hat s) = \int d\hat s_s' d\hat s_s''\bigg[\tilde U_B(\hat s - \hat s_s', \mu_\Lambda, \mu_\Gamma)\bigg]\bigg[\frac{2}{m_J}E_\text{T}^{\Gamma=0}(\hat s_s' - \hat s_s'')\bigg]\bigg[m_J B_+^{\text{tree}}(\hat s_s'', 2\Gamma_t)\bigg]. \tag{G2}$$

Here the Breit-Wigner has a width of $2\Gamma_t$, and the function $E_{\rm T}^{\Gamma=0}(\hat{s})$ is identical to $E_+^{\Gamma=0}(\hat{s})$ in Eq. (E1) but with the replacements $\{\alpha_s \to 2\alpha_s,\ \delta_1 \to 2\delta_1,\ \delta m_J \to 2\delta m_J\}$. Finally the evolution kernel is

$$\tilde{U}_B(\hat{s}, \mu, \mu_0) = \frac{e^{2K_3}(e^{\gamma_E})^{2\omega_1}}{\mu_0 \Gamma(-2\omega_1)} \bigg[\frac{\mu_0^{1+2\omega_1}\theta(\hat{s}-\hat{s}')}{(\hat{s}-\hat{s}')^{1+2\omega_1}}\bigg]_+, \tag{G3}$$

which is equivalent to the kernel U_B for the bHQET jet function but with the anomalous dimensions doubled. We can write the function $E_{\rm T}^{\Gamma=0}(\hat{s}) = {\rm Im}[\mathcal{E}_{\rm T}^{\Gamma=0}(\hat{s})]$, where $\mathcal{E}_{\rm T}^{\Gamma=0}(\hat{s})$ has the same form as $\mathcal{E}_+^{\Gamma=0}(\hat{s})$ in Eq. (E4) but with the replacements $\{\alpha_s \to 2\alpha_s,\ \delta_1 \to 2\delta_1,\ \delta m_J \to 2\delta m_J\}$. The result in Eq. (G2) has a structure such that we can perform the last two integrations with the same techniques as in Appendix E. We obtain $G_{\rm T}(\hat{s}) = {\rm Im}[\mathcal{G}_{\rm T}(\hat{s}) + \delta\mathcal{G}_{\rm T}(\hat{s})]$ where

$$\begin{aligned}
\mathcal{G}_{\rm T}(\hat{s}) &= \frac{2}{\pi m_J^2}\bigg\{G_0^T(\hat{s}) + \frac{2C_F\alpha_s(\mu_\Gamma)}{\pi}\bigg[G_2^T(\hat{s}) - G_1^T(\hat{s}) + \bigg(1+\frac{5\pi^2}{24}\bigg)G_0^T(\hat{s})\bigg] \\
&\quad + \frac{2C_F\alpha_s(\mu_\Lambda)}{\pi}\bigg[-G_2^T(\hat{s}) + 2\ln\bigg(\frac{\mu_\Lambda Q}{\mu_\Gamma m_J}\bigg)G_1^T(\hat{s}) - \bigg(\frac{7\pi^2}{24} + \ln^2\bigg(\frac{\mu_\Lambda Q}{\mu_\Gamma m_J}\bigg)\bigg)G_0^T(\hat{s})\bigg]\bigg\}, \\
\delta\mathcal{G}_{\rm T}(\hat{s}) &= -\frac{4}{\pi m_J^2}\bigg[\frac{Q}{m_J}\delta_1(\mu_\Lambda) + 2\delta m_J(\mu_\Gamma)\bigg]\frac{d}{d\hat{s}}G_0^T,
\end{aligned} \tag{G4}$$

and $G_n^T(\hat{s}) = G_n^T(\hat{s}, \Gamma_t, \mu_\Lambda, \mu_\Gamma)$ is simply $G_n(\hat{s}, \Gamma_t, \mu_\Lambda, \mu_\Gamma)$ from Eq. (E6) but with $\omega_1 \to 2\omega_1$, $K_3 \to 2K_3$, and $\Gamma_t \to 2\Gamma_t$.

Including the prefactor from Eq. (189) we have the final result

$$P_{\rm T}(\hat{s}, \mu_\Lambda) = \frac{m_J Q^2}{2} H_Q(Q, \mu_Q) U_{H_Q}(Q, \mu_Q, \mu_m) H_m(m, \mu_m) U_{H_m}\bigg(\frac{Q}{m_J}, \mu_m, \mu_\Lambda\bigg) G_{\rm T}\bigg(\hat{s}, \frac{Q}{m_J}, \Gamma_t, \mu_\Lambda\bigg). \tag{G5}$$

---

[1] Tevatron Electroweak Working Group, arXiv:hep-ex/0703034.
[2] S. Fleming, A. H. Hoang, S. Mantry, and I. W. Stewart, Phys. Rev. D **77**, 074010 (2008).
[3] C. W. Bauer, S. Fleming, D. Pirjol, and I. W. Stewart, Phys. Rev. D **63**, 114020 (2001).
[4] C. W. Bauer, S. Fleming, D. Pirjol, I. Z. Rothstein, and I. W. Stewart, Phys. Rev. D **66**, 014017 (2002).
[5] C. W. Bauer, D. Pirjol, and I. W. Stewart, Phys. Rev. D **65**, 054022 (2002).
[6] C. W. Bauer and I. W. Stewart, Phys. Lett. B **516**, 134 (2001).
[7] C. W. Bauer, S. Fleming, and M. E. Luke, Phys. Rev. D **63**, 014006 (2000).
[8] A. V. Manohar and M. B. Wise, *Heavy Quark Physics* (Cambridge University Press, Cambridge, England, 2000).
[9] N. Isgur and M. B. Wise, Phys. Lett. B **232**, 113 (1989).
[10] N. Isgur and M. B. Wise, Phys. Lett. B **237**, 527 (1990).
[11] B. Grinstein, Nucl. Phys. **B339**, 253 (1990).
[12] E. Eichten and B. Hill, Phys. Lett. B **234**, 511 (1990).
[13] H. Georgi, Phys. Lett. B **240**, 447 (1990).
[14] M. Beneke, A. P. Chapovsky, A. Signer, and G. Zanderighi, Phys. Rev. Lett. **93**, 011602 (2004).
[15] M. Beneke, A. P. Chapovsky, A. Signer, and G. Zanderighi, Nucl. Phys. **B686**, 205 (2004).
[16] V. S. Fadin and V. A. Khoze, Pis'ma Zh. Eksp. Teor. Fiz. **46**, 417 (1987) [JETP Lett. **46**, 525 (1987)].
[17] A. H. Hoang and C. J. Reisser, Phys. Rev. D **71**, 074022 (2005).
[18] C. W. Bauer, C. Lee, A. V. Manohar, and M. B. Wise, Phys. Rev. D **70**, 034014 (2004).
[19] G. P. Korchemsky and G. Sterman, Nucl. Phys. **B555**, 335 (1999).
[20] C. W. Bauer, A. V. Manohar, and M. B. Wise, Phys. Rev. Lett. **91**, 122001 (2003).
[21] G. P. Korchemsky and G. Sterman, Nucl. Phys. **B437**, 415 (1995).
[22] G. P. Korchemsky and S. Tafat, J. High Energy Phys. 10 (2000) 010.
[23] C. Lee and G. Sterman, Phys. Rev. D **75**, 014022 (2007).
[24] C. Lee and G. Sterman, arXiv:hep-ph/0603066.
[25] G. P. Korchemsky, arXiv:hep-ph/9806537.
[26] C. F. Berger, T. Kucs, and G. Sterman, Phys. Rev. D **68**, 014012 (2003).
[27] C. F. Berger and G. Sterman, Eur. Phys. J. C **33**, s407 (2004).
[28] C. F. Berger, T. Kucs, and G. Sterman, Int. J. Mod. Phys. A **18**, 4159 (2003).
[29] A. V. Belitsky, G. P. Korchemsky, and G. Sterman, Phys. Lett. B **515**, 297 (2001).
[30] A. H. Hoang and I. W. Stewart, Phys. Lett. B **660**, 483 (2008).
[31] S. Catani, G. Turnock, B. R. Webber, and L. Trentadue, Phys. Lett. B **263**, 491 (1991).
[32] S. Catani, L. Trentadue, G. Turnock, and B. R. Webber, Nucl. Phys. **B407**, 3 (1993).
[33] S. J. Burby and E. W. N. Glover, J. High Energy Phys. 04 (2001) 029.

[34] F. Krauss and G. Rodrigo, Phys. Lett. B **576**, 135 (2003).
[35] E. Gardi and J. Rathsman, Nucl. Phys. **B609**, 123 (2001).
[36] Y.L. Dokshitzer, A. Lucenti, G. Marchesini, and G.P. Salam, J. High Energy Phys. 01 (1998) 011.
[37] S. Catani and B.R. Webber, Phys. Lett. B **427**, 377 (1998).
[38] C.F. Berger, Phys. Rev. D **66**, 116002 (2002).
[39] A. Banfi, Y.L. Dokshitzer, G. Marchesini, and G. Zanderighi, J. High Energy Phys. 05 (2001) 040.
[40] A. Banfi, G.P. Salam, and G. Zanderighi, J. High Energy Phys. 01 (2002) 018.
[41] C.F. Berger, T. Kucs, and G. Sterman, Phys. Rev. D **65**, 094031 (2002).
[42] E. Gardi and L. Magnea, J. High Energy Phys. 08 (2003) 030.
[43] G.P. Korchemsky and G. Marchesini, Phys. Lett. B **313**, 433 (1993).
[44] M. Trott, Phys. Rev. D **75**, 054011 (2007).
[45] A.V. Manohar, Phys. Rev. D **68**, 114019 (2003).
[46] T. Becher, M. Neubert, and B.D. Pecjak, J. High Energy Phys. 01 (2007) 076.
[47] M. Neubert, Phys. Rev. D **72**, 074025 (2005).
[48] T. Becher, M. Neubert, and G. Xu, arXiv:0710.0680.
[49] M.D. Schwartz, Phys. Rev. D **77**, 014026 (2008).
[50] G.P. Korchemsky and A.V. Radyushkin, Phys. Lett. B **279**, 359 (1992).
[51] J.C. Collins, D.E. Soper, and G. Sterman, Nucl. Phys. **B308**, 833 (1988).
[52] B.A. Kniehl, Phys. Lett. B **237**, 127 (1990).
[53] A.H. Hoang, J.H. Kuhn, and T. Teubner, Nucl. Phys. **B452**, 173 (1995).
[54] G.J.H. Burgers, Phys. Lett. B **164**, 167 (1985).
[55] A.V. Manohar and I.W. Stewart, Phys. Rev. D **76**, 074002 (2007).
[56] J.-y. Chiu, F. Golf, R. Kelley, and A.V. Manohar, Phys. Rev. Lett. **100**, 021802 (2008).
[57] T. Becher and K. Melnikov, J. High Energy Phys. 06 (2007) 084.
[58] A.H. Hoang and C.J. Reisser, Phys. Rev. D **74**, 034002 (2006).
[59] A.H. Hoang and T. Teubner, Phys. Rev. D **60**, 114027 (1999).
[60] E.C. Poggio, H.R. Quinn, and S. Weinberg, Phys. Rev. D **13**, 1958 (1976).
[61] C.W. Bauer and A.V. Manohar, Phys. Rev. D **70**, 034024 (2004).
[62] K.S.M. Lee, Z. Ligeti, I.W. Stewart, and F.J. Tackmann, Phys. Rev. D **74**, 011501 (2006).
[63] J.C. Collins, A.V. Manohar, and M.B. Wise, Phys. Rev. D **73**, 105019 (2006).
[64] A.M. Polyakov, Nucl. Phys. **B164**, 171 (1980).
[65] I.Y. Arefeva, Phys. Lett. B **93**, 347 (1980).
[66] J.-L. Gervais and A. Neveu, Phys. Lett. B **80**, 255 (1979).
[67] V.S. Dotsenko and S.N. Vergeles, Nucl. Phys. **B169**, 527 (1980).
[68] R.A. Brandt, F. Neri, and M.-a. Sato, Phys. Rev. D **24**, 879 (1981).
[69] S. Aoyama, Nucl. Phys. **B194**, 513 (1982).
[70] J. Chay, C. Kim, and A.K. Leibovich, Phys. Rev. D **72**, 014010 (2005).
[71] A.J. Buras, arXiv:hep-ph/9806471.
[72] J.G.M. Gatheral, Phys. Lett. B **133**, 90 (1983).
[73] J. Frenkel and J.C. Taylor, Nucl. Phys. **B246**, 231 (1984).
[74] G.P. Korchemsky and A.V. Radyushkin, Nucl. Phys. **B283**, 342 (1987).
[75] H. Boos, T. Feldmann, T. Mannel, and B.D. Pecjak, J. High Energy Phys. 05 (2006) 056.
[76] J. Chay, C. Kim, Y.G. Kim, and J.-P. Lee, Phys. Rev. D **71**, 056001 (2005).
[77] S. Catani, Y.L. Dokshitzer, M. Olsson, G. Turnock, and B.R. Webber, Phys. Lett. B **269**, 432 (1991).
[78] A.F. Falk and B. Grinstein, Phys. Lett. B **249**, 314 (1990).
[79] M. Beneke and V.M. Braun, Nucl. Phys. **B426**, 301 (1994).
[80] A.H. Hoang *et al.*, Eur. Phys. J. direct C **2**, 1 (2000).
[81] A.H. Hoang, A.V. Manohar, I.W. Stewart, and T. Teubner, Phys. Rev. D **65**, 014014 (2001).
[82] S. Fleming, A.H. Hoang, S. Mantry, and I. Stewart (unpublished).
[83] A. Jain, I. Scimemi, and I. Stewart (unpublished).
[84] S.W. Bosch, B.O. Lange, M. Neubert, and G. Paz, Nucl. Phys. **B699**, 335 (2004).
[85] M. Beneke, Phys. Rep. **317**, 1 (1999).
[86] A.H. Hoang, M.C. Smith, T. Stelzer, and S. Willenbrock, Phys. Rev. D **59**, 114014 (1999).
[87] M. Beneke, Phys. Lett. B **434**, 115 (1998).
[88] N. Uraltsev, arXiv:hep-ph/9804275.
[89] A.H. Hoang, Z. Ligeti, and A.V. Manohar, Phys. Rev. Lett. **82**, 277 (1999).
[90] A.H. Hoang, Z. Ligeti, and A.V. Manohar, Phys. Rev. D **59**, 074017 (1999).
[91] A.H. Hoang and A.V. Manohar, Phys. Lett. B **633**, 526 (2006).
[92] N. Gray, D.J. Broadhurst, W. Grafe, and K. Schilcher, Z. Phys. C **48**, 673 (1990).
[93] K. Melnikov and T.v. Ritbergen, Phys. Lett. B **482**, 99 (2000).
[94] K.G. Chetyrkin and M. Steinhauser, Nucl. Phys. **B573**, 617 (2000).
[95] A. Pineda and A. Signer, Nucl. Phys. **B762**, 67 (2007).
[96] M. Martinez and R. Miquel, Eur. Phys. J. C **27**, 49 (2003).
[97] A. Juste *et al.*, econf C0508141, PLEN0043 (2005).
[98] A.H. Hoang, A.V. Manohar, and I.W. Stewart, Phys. Rev. D **64**, 014033 (2001).
[99] A. Pineda, Phys. Rev. D **65**, 074007 (2002).
[100] A. Pineda, Phys. Rev. A **66**, 062108 (2002).
[101] A.H. Hoang and I.W. Stewart, Phys. Rev. D **67**, 114020 (2003).
[102] B.A. Kniehl, A.A. Penin, V.A. Smirnov, and M. Steinhauser, Nucl. Phys. **B635**, 357 (2002).
[103] M. Beneke, Y. Kiyo, and K. Schuller, Nucl. Phys. **B714**, 67 (2005).
[104] E. Gardi, J. High Energy Phys. 04 (2000) 030.
[105] A.K. Leibovich, Z. Ligeti, and M.B. Wise, Phys. Lett. B **564**, 231 (2003).
[106] I.Z. Rothstein, Phys. Rev. D **70**, 054024 (2004).
[107] C. Balzereit, T. Mannel, and W. Kilian, Phys. Rev. D **58**, 114029 (1998).
[108] M. Neubert, Eur. Phys. J. C **40**, 165 (2005).